THE UNIVERSITY OF CHICAGO

DESIGN PRINCIPLES FOR NON-EQUILIBRIUM SELF-ASSEMBLY

A DISSERTATION SUBMITTED TO
THE FACULTY OF THE DIVISION OF THE PHYSICAL SCIENCES
IN CANDIDACY FOR THE DEGREE OF
DOCTOR OF PHILOSOPHY

DEPARTMENT OF CHEMISTRY

BY

MICHAEL NGUYEN

CHICAGO, ILLINOIS
AUGUST 2021

For my parents

"Talking nonsense is the sole privilege mankind possesses over the other organisms. It's by talking nonsense that one gets to the truth! I talk nonsense, therefore I'm human."

— Fyodor Dostoevsky

TABLE OF CONTENTS

LIST OF FIGURES

LIST OF TABLES

ACKNOWLEDGMENTS

First, I would like to thank my advisor, Suriyanarayanan Vaikuntanathan, for his generosity, patience, understanding, and especially for his support when I was very sick. Next, I want to acknowledge my committee members, Aaron Dinner and Dmitri Talapin, for their advice and valuable time. I also would like to thank members of the Vaikuntanathan Group for their companionship and assistance. Finally, I would like to thank my parents for all their sacrifices and always being by my side.

ABSTRACT

Self-assembly is a process in which components in a system organize themselves into structures and patterns without human intervention. Though design principles for self-assembly for systems at global or local equilibrium have seen many advances recently, there has not been much progress for self-assembly far from equilibrium. Indeed, many essential processes in biophysics and chemistry occur far from equilibrium. The self-assembly of lipids into membranes, the growing of nanowires using the VLS technique, the making of many pro-drugs, vaccines, and the self-healing of intelligent materials are all examples of non-equilibrium self-assembly. Design principles for non-equilibrium self-assembly can potentially revolutionize our approach to making materials and understanding non-equilibrium processes. In this work, we attempt to derive general design principles for non-equilibrium self-assembly with ideas from stochastic thermodynamics.

First, we will develop a general framework to study self-assembly with master equations. We then used ideas from stochastic thermodynamics to write down a general form for the energy dissipation for these processes. The energy dissipation form then allows us to write bounds that can be used to constraints possible structures that the assembly will adopt under a non-equilibrium drive. In particular, using this framework, we can predict the necessary driving force for a phase transition as shown in Chapter 3 or growth instability in Chapter 4. We then further expand our frameworks to systems with multiple drive forces and systems under periodic drive in the later chapters.

CHAPTER 1

INTRODUCTION

The fields of colloidal and nanoscale self-assembly have seen dramatic progress in the last few years. Indeed experimental and theoretical work has elucidated design principles for the assembly of complex three-dimensional structures [4, 5, 6, 7]. Most of these advances, however, are based on an equilibrium thermodynamic framework: the target structure minimizes a thermodynamic free energy [8]. Understanding the principles governing self-assembly and organization far from equilibrium systems remains one of the central challenges of non-equilibrium statistical mechanics [9, 10, 1, 11, 12, 13, 14, 15]. This dissertation contributes to this research by deriving design principles for a class of non-equilibrium driven self-assembly processes. These principles can be used to predict possible structures that can be achieved under non-equilibrium drives.

Imagine a self-assembly process in which interactions amongst the various monomers are described by a set of energies E^{eq}. The ratio of association and dissociation rates is set by a combination of interaction energies and chemical potentials $\{\dots \mu_i \dots\}$ of the monomers. This generic setup is sufficient to describe many self-assembly processes. Examples include growth of crystals from solution by nucleation [11], growth dynamics of cell walls [16], growth of multicomponent assemblies [7] and growth dynamics of biological polymers and filaments [17]. The chemical potential controls the growth of the assembly. If the chemical potential is tuned to a *coexistence* value such that the assembly grows at an infinitesimally slow rate, then the structure of the assembly and its composition can be predicted by computing the equilibrium partition function and free energy G^{eq} appropriate to the set of interaction energies (Fig 1.1 Right). For values of the chemical potentials more favorable than the coexistence chemical potential, the assembly grows at a non-zero rate. In such instances, the structure and composition of the growing assembly might not have sufficient time to relax to values characteristic of the equilibrium partition function [11, 18, 19].

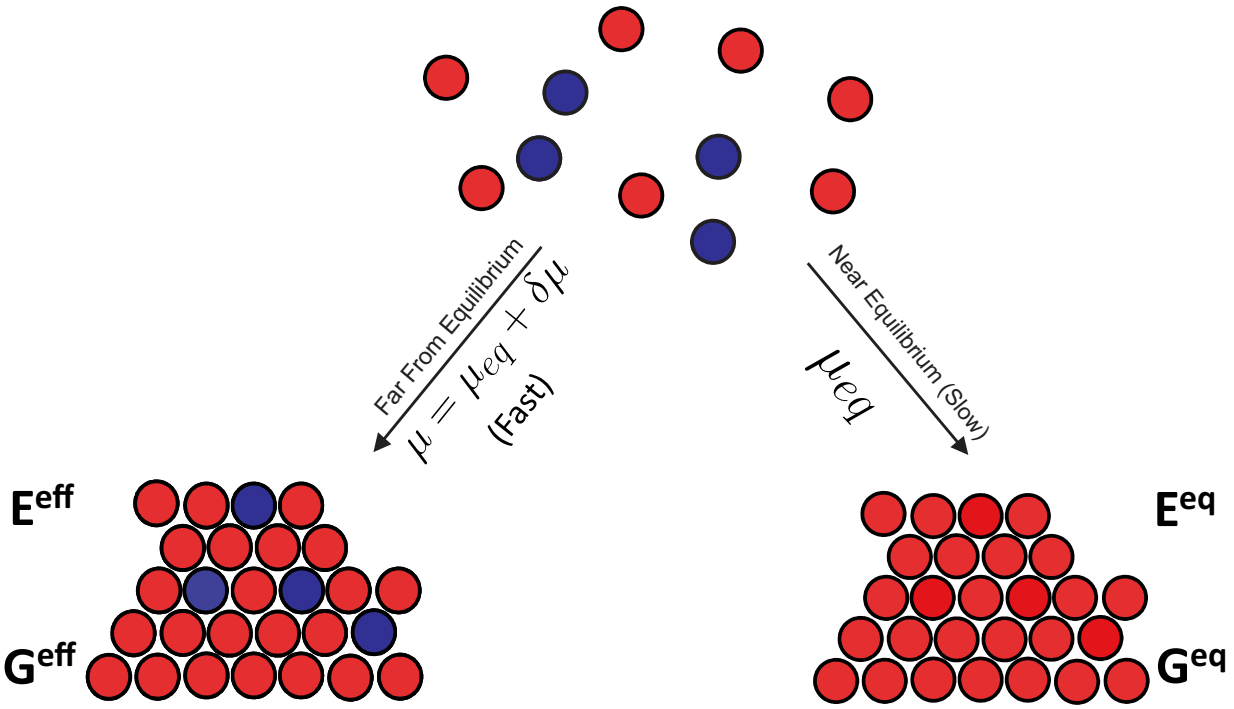

Figure 1.1: Schematic of the self-assembly problem considered in the dissertation. Right: When the chemical potential is at equilibrium, μ_{eq}, the assembly grows slowly with structured determined by the equilibrium energy landscape E^{eq} and its free energy G^{eq}. Left: When the chemical potential is higher than the equilibrium chemical potential, the assembly grows fast with a new structure. Let's assume that the new structure is determined by an effective energy landscape E^{eff} with its free energy G^{eff}.

Defects are accumulated as the self assembled structure grows at a non-zero rate. The time taken for a defect to anneal increases rapidly with distance from the interface of the growing structure (Fig 1.1 Left). Due to the resulting kinetically-trapped states, the crystal can assume structures very different from those representatives of the equilibrium state [11, 18, 19].

By applying the second law of thermodynamics and the formalism of stochastic thermodynamics, we derive a surprising thermodynamic relation that is applicable to the above-mentioned kinetic processes. This relation provides constraints on the configurations that are achievable in a non-equilibrium self-assembly process,

$$\langle \dot{N} \rangle \left[\delta\mu - \frac{D[p_N(\omega)||p_N^{\mathrm{eq}}(\omega)]}{N} \right] \geq 0 \,, \tag{1.1}$$

where N is the size of the assembly at some instant of time, $\langle \dot{N} \rangle$ is the average rate of the growth of the assembly, $p_N(\omega)$ is probability distribution associated with a configuration ω in the growing assembly, $p_N^{\mathrm{eq}}(\omega) \equiv \exp[-(E^{\mathrm{eq}}(\omega) - G_N^{\mathrm{eq}})/k_B T]$ is the equilibrium probability distribution obtained when the assembly is grown at an infinitesimally slow rate and $D[p||q] = \int p \ln p/q \geq 0$ is the relative entropy between distributions p and q. The relative entropy is a measure of distinguishability between distributions p and q. It is zero only when the two distributions are identical and is nonzero otherwise. We have assumed that the chemical potential of each monomer is the same and exceeds the equilibrium coexistence value by $\delta\mu$ (i.e. the concentrations of monomers in solution exceeds the equilibrium concentration required for assembly). The chemical potential difference $\delta\mu$ provides the non-equilibrium driving force for self assembly.

An alternative and presumably more practical formulation of the central result is in terms of interaction energies. Imagine that we wish to generate compositions and structures in the growing assembly which are characteristic of a Hamiltonian E^{eff} different from the Hamiltonian governing the interactions between species E^{eq}. The central result places a bound on the minimum required excess chemical potential $\delta\mu$ required to achieve such an

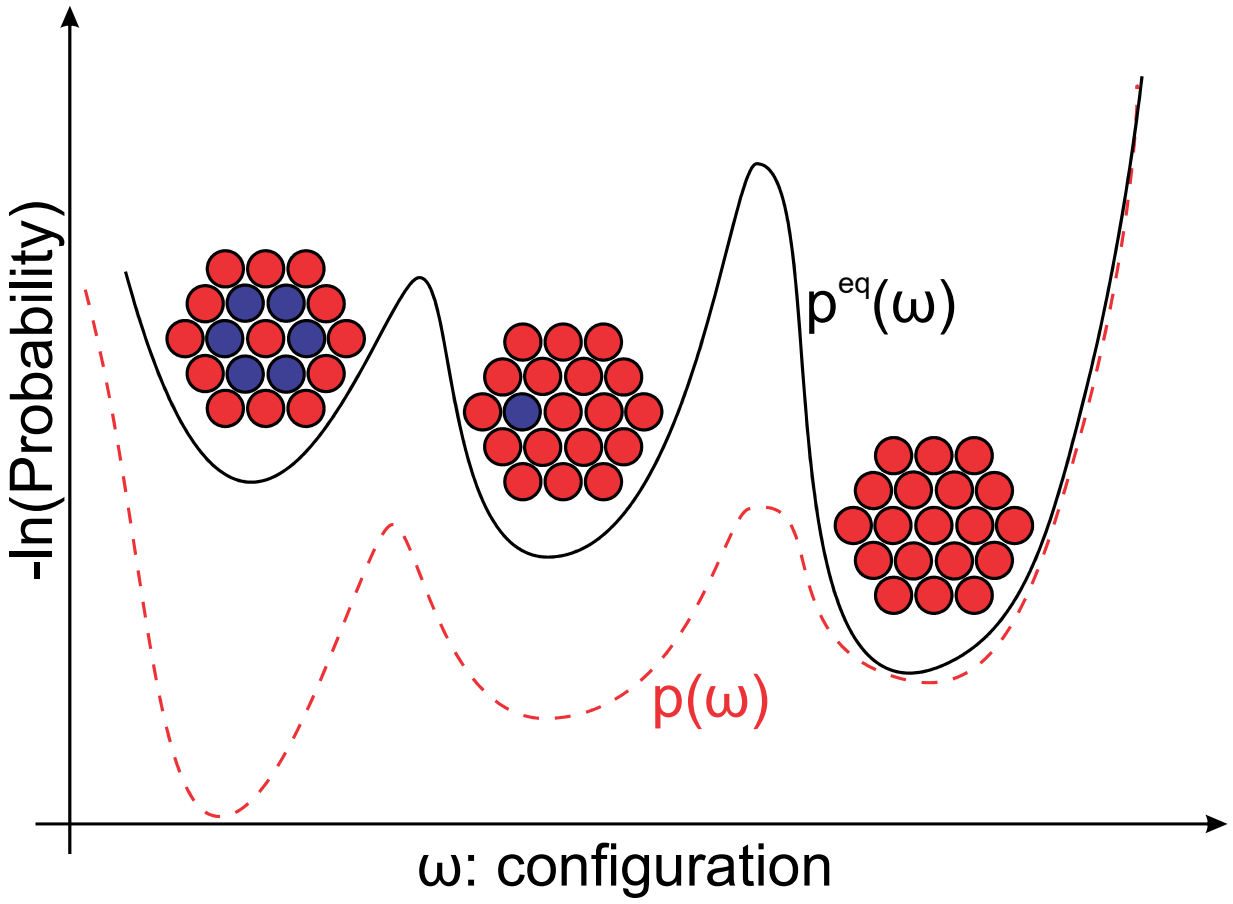

Figure 1.2: Schematic of the possible structures the assembly can adapt. The probability of observing structural and compositional fluctuations in the growing assembly, $p(\omega)$ can be different from the canonical distribution $p^{\mathrm{eq}}(\omega)$ specified by the interaction energies E^{eq}. Our central result, Eq. 1.1 constrains the set of compositional fluctuations that can be achieved under a chemical potential drive $\delta\mu$.

assembly,

$$\langle \dot{N} \rangle \left[\frac{-G_N^{\text{eff}} + G_N^{\text{eq}} + \langle E^{\text{eff}} - E^{\text{eq}} \rangle_N}{N} + \delta\mu \right] \geq 0 \,. \tag{1.2}$$

Here G_N^{eff} is the free energy of N particle system described by the Hamiltonian E^{eff}. The free energies differences can either be computed directly from simulations or estimated using an analytical framework.

Hence, given a chemical potential drive Eq. 1.1, Eq. 1.2 constrain the set of allowed non-equilibrium structures found in the assembly. Alternately, given a target distribution $p_N(\omega)$ or a target effective Hamiltonian E^{eff}, the central result sets a bound on the minimum chemical potential driving force required to achieve the assembly. If the chemical potentials of the monomers can be varied, $\delta\mu$ in Eq. 1.1 and Eq. 1.2 is replaced by an average, $\langle \sum_i \delta\mu_i \rangle_N / N$. The bound can be used to variationally optimize non-equilibrium driving forces $\{ \dots \mu_i \dots \}$ that result in configurations characteristic of a desired effective energy landscape.

An even tighter bound can be obtained with the thermodynamics uncertainty relations. These newly discovered relations state that the relative fluctuations of all currents in a process are bound by its entropy production. Close to equilibrium, these relations are equivalent to statements of the fluctuation dissipation relation or linear response theory. Many applications and extensions of these relations have been proposed [20, 21, 22, 23, 24, 25, 26]. By adopting the thermodynamic uncertainty relations to the problem of non-equilibrium self-assembly, we can obtain another form of the design principle:

$$\langle \dot{N} \rangle \left[\frac{-G_N^{\text{eff}} + G_N^{\text{eq}} + \langle E^{\text{eff}} - E^{\text{eq}} \rangle_N}{N} + \delta\mu \right] \geq \frac{2\langle \dot{N} \rangle^2}{Var(\dot{N})} \tag{1.3}$$

Here $Var(\dot{N})$ is the variance for the growth rate of the system. Since the term on the right is always positive, Eq. 1.3 offers a tighter bound than Eq. 1.2. Thus, with extra information from the kinetics of the process, we can further refine our prediction on the structures of the growing assembly.

In the following chapters, we will derive our central results and explore its applications to various models. But first, in Chapter 2, we will introduce many basic concepts and framework about the self-assembly process that will be used throughout this dissertation. The design principles will then emerge out from these foundations at the end of the chapter. Chapter 3 will examine the framework introduced in Chapter 2 by studying two simple but important growing self-assembly systems, the 1D and 2D lattice assembly. The 1D lattice assembly is one of the few problems that can be solved exactly with our approach. The results of the model will then be compared directly to those from Kinetic Monte Carlo simulations. In addition to confirming this approach, we will explore how non-equilibrium drive can affect correlations and defects in the 1D lattice assembly and how the design principles can be used to make predictions on the structure of the assembly. Next, we will look at the growing of the 2D lattice assembly, which exhibits a phase transition from a demixed phase to a mixed phase. Even though this transition is similar to the one in the 2D Ising model, it is driven by the non-equilibrium driving force and not temperature. We will use our framework to write an equation predicting how the chemical driving force drives the transition.

In Chapters 4 and 5, we will turn to problems with more biological flavors. Specifically, Chapter 4 looks at a model of an elastic membrane in which non-equilibrium forcing can cause the membrane to buckle and undergo a morphological transformation. We will demonstrate how the design principles can be used to predict this transformation phenomenologically. In the process, we will also extend our framework from a system with just compositional fluctuation to one with continuous structural fluctuation. Inspired by recent experiments showing how actin growth rates tune the morphology of the whole bundle [27], in Chapter 5, we develop a minimal model to study this phenomenon. There, we will also expand our design principles to include multiple drives and kinetics.

In Chapter 6, we will look at self-assembly with periodic drive. Specifically, we will extend our framework to work with a system under a periodic drive using a bipartile Markov

network setup and a mean-field setup. In chapter 7, we will give a conclusion and brief outlook for future projects.

CHAPTER 2

SETTING UP THE PROBLEM

2.1 Introduction

Here we will sketch out the self-assembly growth process used throughout this dissertation. As a matter of convenience, we will set $k_B T = 1$. Let's first consider an assembly in a bath. This assembly is made up by many elements n_i. The elements here can mean many things: it can be a monomer in a polymer; it can be a molecule, atom, or spin for other kinds of assembly. For now, let us think of these elements as particles making up a 1D solid assembly in a bath. As we go through the dissertation, we will see that the analysis described here can be generalized to a more complex setup.

The state of the 1D lattice assembly is then fully described by the elements making it: $\omega^N = \{n_1, n_2, ...n_N\}$. Here N is the total number of elements, and n_i indicates a different kind of elements. In the bath, the assembly will grow and shrink stochastically. We will assume that the assembly only grows in one end n_N. In the limit of large N, this assumption should not reduce the complexity of the problem since the behavior of the other end is identical to the one we are considering. We will also assume that there are little or very slow internal relaxations inside the assembly because fast internal relaxations will eventually transform the assembly into its equilibrium structure. We will now use the probability $P(n_1, n_2, ...n_N)$ to describe the assembly and its time evolution.

Usually, to analyze a growing assembly, we look at the complete configurations probabilities of an assembly after a long time. This is usually done with simulations because the probability space of the assembly is quite big for analytical consideration. Suppose there are no internal relaxations inside the assembly. In that case, however, we can look at the system in another way: observe and record the elements coming into the assembly one by one during its growth, then reconstruct the entire configuration from there. This will be the

main approach that we will use in this dissertation. There are two main reasons for this. First, this will make writing down entropy production much easier because it focuses more on all the possible transitions taking place, not the configuration of the whole assembly. Second, the thermodynamics uncertainty relations that we adapt for our design principles were originally derived for finite Markov state graphs with periodic boundary conditions not on a system with increasing size like a growing assembly [21]. This issue can be overcome with the second approach. We also would like to mention that this approach has been used by many to study assembly in other contexts such as copolymerization [28, 29].

2.2 The Master Equations For Growing An Assembly

As the system grows from state $(n1, ..., n_N)$ to $(n1, ..., n_N, n_{N+1})$, we assign its transitions as:

$$\begin{aligned} &W_{add}(n_1, ..., n_N \to n_1, ..., n_{N+1}) \\ &\quad = P_{gen}(n_1, ..., n_{N+1}|n_1, ..., n_N) k_{add}(n_1, ..., n_N \to n_1, ..., n_{N+1}) \end{aligned} \tag{2.1}$$

$$W_{rem}(n_1, ..., n_N \leftarrow n_1, ..., n_{N+1}) = k_{rem}(n_1, ..., n_N \leftarrow n_1, ..., n_{N+1}) \tag{2.2}$$

Here $k_{add}(n_1, ..., n_N \to n_1, ..., n_{N+1})$ and $k_{rem}(n_1, ..., n_N \leftarrow n_1, ..., n_{N+1})$ are the addition and removal rates of the n_{N+1} particle respectively. $P_{gen}(n_1, ..., n_{N+1}|n_1, ..., n_N)$ is the probability of getting a particular n_{N+1} from the bath which depends on the concentrations in the bath and the property of the interface. With this, we can write out the master

equations for the probabilities of the full configurations:

$$\begin{aligned}\frac{dP(n_1,...,n_N)}{dt} &= -P(n_1,...,n_N)\Big[k_{rem}(n_1,...,n_{N-1} \leftarrow n_1,...,n_N) \\ &+ \sum_{n_{N+1}} P_{gen}(n_1,...,n_{N+1}|n_1,...,n_N)k_{add}(n_1,...,n_N \rightarrow n_1,...,n_{N+1})\Big] \\ &+ \Big[\sum_{n_{N+1}} P(n_1,...,n_{N+1})k_{rem}(n_1,...,n_N \leftarrow n_1,...,n_{N+1})\Big] \\ &+ \Big[P(n_1,...,n_{N-1})P_{gen}(n_1,...,n_N|n_1,...,n_{N-1})k_{add}(n_1,...,n_{N-1} \rightarrow n_1,...,n_N)\Big]\end{aligned} \tag{2.3}$$

To proceed forward, we will now make an assumption that the addition and removal rates only depend on the two furthest particles of the assembly. If the actual rates depend more than that, we can expand the element n until the rates depend only on the furthest two elements. We then rewrite: $k_{add}(n_1,...,n_N \rightarrow n_1,...,n_{N+1}) = k_{add}(n_{N-1},n_N \rightarrow n_N,n_{N+1})$, $k_{rem}(n_1,...,n_N \leftarrow n_1,...,n_{N+1}) = k_{rem}(n_{N-1},n_N \leftarrow n_N,n_{N+1})$ and $P_{gen}(n_1,...,n_{N+1}|n_1,...,n_N) = P_{gen}(n_{N+1}|n_N)$. We then define the probability:

$$P^N(n_{N-1},n_N) = \lim_{N\rightarrow\infty} \sum_{n_1,...,n_{N-2}} P(n_1,...,n_N) \tag{2.4}$$

This is the probability of observing the two furthest elements when they are attached to a big assembly. The first N in $P^N(n_{N-1},n_N)$ is mainly to distinguish it from the normal probability $P(n_1,...,n_N)$. The other Ns in the parenthesis $P^N(n_{N-1},n_N)$ are there as indexes. Next, we sum over the master equations of the full probability, $P(n_1,...,n_N)$, to

arrive at the master equations for the new one, $P^N(n_{N-1}, n_N)$:

$$\begin{aligned}
\frac{dP^N(n_{N-1},n_N)}{dt} &= -P^N(n_{N-1},n_N)\Big[\sum_{n_{N+1}} P_{gen}(n_{N+1}|n_N)k_{add}(n_{N-1},n_N \to n_N,n_{N+1})\Big] \\
&- \Big[\sum_{n_1,...,n_{N-2}} P(n_1,...,n_N)k_{rem}(n_{N-2},n_{N-1} \leftarrow n_{N-1},n_N)\Big] \\
&+ \Big[\sum_{n_1,...,n_{N-2},n_{N+1}} P(n_1,...,n_{N+1})k_{rem}(n_{N-1},n_N \leftarrow n_N,n_{N+1})\Big] \\
&+ \Big[\sum_{n_{N-2}} P^{N-1}(n_{N-2},n_{N-1})P_{gen}(n_N|n_{N-1})k_{add}(n_{N-2},n_{N-1} \to n_{N-1},n_N)\Big]
\end{aligned} \tag{2.5}$$

Next we rewrite the second term as:

$$\begin{aligned}
&\sum_{n_1,...,n_{N-2}} P(n_1,...,n_N)k_{rem}(n_{N-2},n_{N-1} \leftarrow n_{N-1},n_N) \\
&= P^N(n_{N-1},n_N) \sum_{n_1,...,n_{N-2}} \frac{P(n_1,...,n_N)}{\sum_{n_1,...,n_{N-2}} P(n_1,...,n_N)} k_{rem}(n_{N-2},n_{N-1} \leftarrow n_{N-1},n_N) \\
&= P^N(n_{N-1},n_N) \sum_{n_{N-2}} P_{sys}(n_{N-2}|n_{N-1},n_N)k_{rem}(n_{N-2},n_{N-1} \leftarrow n_{N-1},n_N)
\end{aligned} \tag{2.6}$$

Similarly, we can write the third term as:

$$\begin{aligned}
&\sum_{n_1,...,n_{N-2},n_{N+1}} P(n_1,...,n_{N+1})k_{rem}(n_{N-1},n_N \leftarrow n_N,n_{N+1}) \\
&= \sum_{n_{N+1}} P^{N+1}(n_{N-1},n_N,n_{N+1})k_{rem}(n_{N-1},n_N \leftarrow n_N,n_{N+1}) \\
&= \sum_{n_{N+1}} P^{N+1}(n_N,n_{N+1})P_{sys}(n_{N-1}|n_N,n_{N+1})k_{rem}(n_{N-1},n_N \leftarrow n_N,n_{N+1})
\end{aligned} \tag{2.7}$$

In the limit of large N, we will assume that:

$$P_{sys}(n_{N-1}|n_N, n_{N+1}) = P_{sys}(n_{N-1}|n_N) = \frac{P^N(n_{N-1}, n_N)}{P^N(n_N)} \tag{2.8}$$

Eq. 2.8 says that one will only need the identity of the nearest element to predict the probability of an element next to it. The conditional probability $P_{sys}(\cdot|\cdot)$ can then be used to recover the full original probability of the entire assembly:

$$P(n_1, n_2, ..., n_N) = P_{sys}(n_1|n_2)P_{sys}(n_2|n_3)...P_{sys}(n_{N-1}|n_N)P^N(n_N) \tag{2.9}$$

To get the probability of an element that is M deep inside the assembly we simply use:

$$\begin{aligned} P^N(n_{N-M}) &= \sum_{n_N, n_{N-1}, ..., n_{N+1-M}} P_{sys}(n_{N-M}|n_{N+1-M})...P_{sys}(n_{N-1}|n_N)P^N(n_N) \\ &= \left((\mathbf{P_{sys}})^M P^N\right)(n_{N-M}) \end{aligned} \tag{2.10}$$

Here we have written the conditional probability like an operator that transforms the probability vector of all elements in the interface to the probability vector of all elements inside. In the limit of large M but still smaller than N, we have $P^N(n_{N-M}) = P^N(n_{N-1-M}) = \mathbf{P_{sys}}P^N(n_{N-M})$. Thus the normalized eigenvectors of $\mathbf{P_{sys}}$ corresponding to the eigenvalue 1 will give us the probabilities of the elements deep inside the assembly. With this, instead of solving the large differential equations of $P(n_1, ..., n_N)$, we can solve reduced differential equations of $P^N(n_{N-1}, n_N)$ at steady-state and use $\mathbf{P_{sys}}$ to recover the probabilities deep inside the assembly. However, the cost of reducing the differential equations is that we have introduced non-linearity into the equations making it still if not more difficult to solve in many situations. For better description, from now on we will use the notation $P^N(n_i, n_j)$ in place of $P^N(n_{N-1}, n_N)$ to indicate the probability at the interface and the notation

$P^N_{inside}(n_i, n_j)$ to indicate the probability inside the assembly. In the limit of large N, we make our third assumption:

$$P^N(n_i, n_j) = P^{N-1}(n_i, n_j) = P^{N+1}(n_i, n_j) \tag{2.11}$$

Eq. 2.11 means that in the limit of large N, the probabilities of observing an assembly with different particles by a small amount are about the same.

With these assumptions, the master equations reduce to:

$$\begin{aligned}
\frac{dP^N(n_i, n_j)}{dt} &= -P^N(n_i, n_j)\Big[\sum_{n_k} P_{gen}(n_k|n_j)k_{add}(n_i, n_j \to n_j, n_k)\Big] \\
&- P^N(n_i, n_j)\Big[\sum_{n_k} P_{sys}(n_k|n_i)k_{rem}(n_k, n_i \leftarrow n_i, n_j)\Big] \\
&+ \Big[\sum_{n_k} P^N(n_j, n_k)P_{sys}(n_i|n_j)k_{rem}(n_i, n_j \leftarrow n_j, n_k)\Big] \\
&+ \Big[\sum_{n_k} P^N(n_k, n_i)P_{gen}(n_j|n_i)k_{add}(n_k, n_i \to n_i, n_j)\Big]
\end{aligned} \tag{2.12}$$

With this, we have completely transformed an infinite hierarchy of coupled master equations 2.3 to a smaller set of master equations 2.12 with the cost of linearity. The above master equations make up a Markov network. Each node in the network will consist of two components: (n_i, n_j). n_j, the element to the right, is the element that is directly exposed to the bath while n_i, the element to the left, is between the n_j and the assembly. Because of the structure of the assembly, node (n_i, n_j) can only grow into those of (n_j, n_k) and shrink into those of (n_k, n_i). The current as the system grow from node (n_i, n_j) into (n_j, n_k) is:

$$\begin{aligned}
&J(n_i, n_j \to n_j, n_k) = \\
&P^N(n_i, n_j)P_{gen}(n_k|n_j)k_{add}(n_i, n_j \to n_j, n_k) - P^{N+1}(n_j, n_k)P_{sys}(n_i|n_j)k_{rem}(n_i, n_j \leftarrow n_j, n_k)
\end{aligned} \tag{2.13}$$

At equilibrium, the system will obey detailed balance ie every current will vanish and the distribution will follow the Boltzmann distribution $J(n_i, n_j \to n_j, n_k) = 0$. With some rearrangements, we will have

$$\begin{aligned} P_{gen}(n_k|n_j)\frac{k_{add}(n_i, n_j \to n_j, n_k)}{k_{rem}(n_i, n_j \leftarrow n_j, n_k)} &= \frac{P_{eq}^{N+1}(n_j, n_k)P_{sys}^{eq}(n_i|n_j)}{P_{eq}^{N}(n_i, n_j)} \\ = \frac{P_{eq}^{N+1}(n_i, n_j, n_k)}{P_{eq}^{N}(n_i, n_j)} &= \frac{\exp(-E^{\text{eq}}_{n_j|n_k})}{Z} \end{aligned} \tag{2.14}$$

Here $E^{\text{eq}}_{n_j|n_k}$ is the energy interaction between two elements and Z is the partition function. By setting the additional and removal rates according to Eq. 2.14, the assembly will adopt a configuration following the Boltzmann distribution with an energy landscape E^{eq} at equilibrium. Every time Eq. 2.14 is violated the system will be out of equilibrium. If the left side is bigger, the assembly will grow. If it is lesser, the assembly will shrink. Alternatively, we can rearrange 2.14 to:

$$ZP_{eq}^{N}(n_j, n_k) = \sum_{n_i} \exp(-E^{\text{eq}}_{n_j|n_k})P_{eq}^{N}(n_i, n_j) \tag{2.15}$$

which can be used to set up a matrix, $\exp(-\mathbf{E}^{\text{eq}})$, with the partition function as its eigenvalues and the probabilities: $P_{eq}^{N}(n_j, n_k)$, its eigenvectors.

2.3 The Currents Are Eigenvectors Of The Conditional Probability. $\mathbf{P_{sys}}$

As mentioned earlier, the elements of the eigenvector with eigenvalue one of the conditional probability operator $\mathbf{P_{sys}}$ are the probabilities of the elements deep inside the assembly. Here, we will prove that the currents constructed in 2.13 are also elements of the eigenvector of the conditional probability operator $\mathbf{P_{sys}}$ with eigenvalue one. Thus, one can use the

currents to figure out the probabilities of the element deep inside the assembly. This is equivalent to saying that by observing the elements coming into the assembly, one can predict the configurations inside the assembly when there is no internal relaxation.

When the system is at steady state we have: $\frac{dP^N(n_i,n_j)}{dt} = 0$

$$
\begin{aligned}
0 = &-P^N_{ss}(n_i,n_j)\Big[\sum_{n_k} P_{gen}(n_k|n_j)k_{add}(n_i,n_j \to n_j,n_k)\Big] \\
&- P^N_{ss}(n_i,n_j)\Big[\sum_{n_k} P^{ss}_{sys}(n_k|n_i)k_{rem}(n_k,n_i \leftarrow n_i,n_j)\Big] \\
&+ \Big[\sum_{n_k} P^N_{ss}(n_j,n_k)P^{ss}_{sys}(n_i|n_j)k_{rem}(n_i,n_j \leftarrow n_j,n_k)\Big] \\
&+ \Big[\sum_{n_k} P^N_{ss}(n_k,n_i)P_{gen}(n_j|n_i)k_{add}(n_k,n_i \to n_i,n_j)\Big]
\end{aligned}
\tag{2.16}
$$

The "ss" has been added to the variables to indicate steady state. Now in Eq. 2.16 we will arrange the term into:

$$
\begin{aligned}
&\Big[\sum_{n_k} P^N_{ss}(n_i,n_j)P_{gen}(n_k|n_j)k_{add}(n_i,n_j \to n_j,n_k) - \\
&P^N_{ss}(n_j,n_k)P^{ss}_{sys}(n_i|n_j)k_{rem}(n_i,n_j \leftarrow n_j,n_k)\Big] \\
&= \Big[\sum_{n_k} P^N_{ss}(n_k,n_i)P_{gen}(n_j|n_i)k_{add}(n_k,n_i \to n_i,n_j) - \\
&P^N_{ss}(n_i,n_j)P^{ss}_{sys}(n_k|n_i)k_{rem}(n_k,n_i \leftarrow n_i,n_j)\Big]
\end{aligned}
\tag{2.17}
$$

We then write the first term of the equation to be:

$$\begin{aligned}
&\sum_{n_k} \Big[P_{ss}^{N}(n_i, n_j) P_{gen}(n_k|n_j) k_{add}(n_i, n_j \rightarrow n_j, n_k) - \\
&P_{ss}^{N}(n_j, n_k) P_{sys}^{ss}(n_i|n_j) k_{rem}(n_i, n_j \leftarrow n_j, n_k) \Big] \\
&= \sum_{n_k} \Big[P_{sys}^{ss}(n_i|n_j) P_{ss}^{N}(n_j) P_{gen}(n_k|n_j) k_{add}(n_i, n_j \rightarrow n_j, n_k) - \\
&P_{ss}^{N}(n_j, n_k) P_{sys}^{ss}(n_i|n_j) k_{rem}(n_i, n_j \leftarrow n_j, n_k) \Big] \\
&= P_{sys}^{ss}(n_i|n_j) \sum_{n_k} \Big[P_{ss}^{N}(n_j) P_{gen}(n_k|n_j) k_{add}(n_i, n_j \rightarrow n_j, n_k) - \\
&P_{ss}^{N}(n_j, n_k) k_{rem}(n_i, n_j \leftarrow n_j, n_k) \Big] \\
&= P_{sys}^{ss}(n_i|n_j) \sum_{n_i, n_k} \Big[P_{ss}^{N}(n_i, n_j) P_{gen}(n_k|n_j) k_{add}(n_i, n_j \rightarrow n_j, n_k) - \\
&P_{ss}^{N}(n_j, n_k) P_{sys}(n_i|n_j) k_{rem}(n_i, n_j \leftarrow n_j, n_k) \Big]
\end{aligned} \tag{2.18}$$

The transition from the third term to the fourth term is possible because in our first assumption, the additional and removal rate depends only the first two term and not the inner layer of the assembly. We then define the terms

$$\begin{aligned}
V(n_j, n_k) = \sum_{n_i} \Big[&P_{ss}^{N}(n_i, n_j) P_{gen}(n_k|n_j) k_{add}(n_i, n_j \rightarrow n_j, n_k) - \\
&P_{ss}^{N}(n_j, n_k) P_{sys}(n_i|n_j) k_{rem}(n_i, n_j \leftarrow n_j, n_k) \Big]
\end{aligned} \tag{2.19}$$

$$\begin{aligned}
V(n_j) = \sum_{n_i, n_k} \Big[&P_{ss}^{N}(n_i, n_j) P_{gen}(n_k|n_j) k_{add}(n_i, n_j \rightarrow n_j, n_k) - \\
&P_{ss}^{N}(n_j, n_k) P_{sys}(n_i|n_j) k_{rem}(n_i, n_j \leftarrow n_j, n_k) \Big]
\end{aligned} \tag{2.20}$$

$V(n_j)$ and $V(n_j, n_k)$ are the rates the element n_j and (n_i, n_j) is being added into the assembly. Plugging Eq. 2.20, Eq. 2.19, Eq. 2.18 into Eq. 2.17 and we have:

$$V(n_i, n_j) = P_{sys}(n_i|n_j) V(n_j) \tag{2.21}$$

Sum over all n_j in Eq. 2.21 and we obtain:

$$V(n_i) = \sum_{n_j} P_{sys}(n_i|n_j)V(n_j) = (\mathbf{P_{sys}}V)(n_i) \tag{2.22}$$

This equation indicates that the growth rate of a certain element is also an eigenvector of the conditional probability operator. However, we have also established earlier that the probability of an element deep inside the assembly is also an eigenvector. This suggests that $V(n_i) \propto P^N_{inside}(n_i)$. Using the normalization of probability, we then have:

$$P^N_{inside}(n_i) = \frac{V(n_i)}{\sum_{n_i} V(n_i)} = \frac{V(n_i)}{\langle \dot{N} \rangle} \tag{2.23}$$

$$P^N_{inside}(n_i, n_j) = \frac{V(n_i, n_j)}{\langle \dot{N} \rangle} \tag{2.24}$$

2.4 The Entropy Production

Now let us calculate the entropy production of the growing process. Using the formula from stochastic thermodynamics, the entropy production as the system grow from node (n_i, n_j) into (n_j, n_k) is:

$$\begin{aligned} \dot{S}(n_i, n_j \to n_i, n_k) &= J(n_i, n_j \to n_i, n_k) \ln\left(\frac{P^N_{ss}(n_i, n_j)\, W(n_i, n_j \to n_i, n_k)}{P^N_{ss}(n_j, n_k)\, W(n_i, n_j \leftarrow n_i, n_k)}\right) \\ &= J(n_i, n_j \to n_j, n_k)\left[\ln\left(P_{gen}(n_k|n_j)\frac{k(n_i, n_j \to n_j, n_k)}{k(n_i, n_j \leftarrow n_i, n_k)}\right) - \ln\left(\frac{P^N_{ss}(n_i, n_j, n_k)}{P^N_{ss}(n_i, n_j)}\right)\right] \end{aligned} \tag{2.25}$$

Here we have split the entropy production into two terms. Using Eq. 2.14, we can rewrite the first term as:

$$\ln\left(P_{gen}(n_k|n_j)\frac{k(n_i, n_j \to n_j, n_k)}{k(n_i, n_j \leftarrow n_i, n_k)}\right) = \ln\left(\frac{\exp(\delta\mu - E^{\mathrm{eq}}_{n_j|n_k})}{Z^{\mathrm{eq}}}\right) \tag{2.26}$$

Here $\delta\mu$ is the extra chemical potential that is driving the system out of equilibrium. Next, we define an effective energy function E^{eff} to describe the probability of the assembly as if it is in equilibrium:

$$\ln\left(\frac{P_{ss}^{N}(n_i,n_j,n_k)}{P_{ss}^{N}(n_i,n_j)}\right)=\ln\left(\frac{\exp(-E_{n_j|n_k}^{\text{eff}})}{Z^{\text{eff}}}\right) \tag{2.27}$$

With this we can rewrite the entropy production of the growing process:

$$\begin{aligned}\dot{S}(n_i,n_j\to n_j,n_k)&=J(n_i,n_j\to n_j,n_k)\left[\delta\mu-E_{n_j|n_k}^{\text{eq}}-\ln Z^{\text{eq}}+E_{n_j|n_k}^{\text{eff}}+\ln Z^{\text{eff}}\right]\\&=J(n_i,n_j\to n_j,n_k)\left[\delta\mu-E_{n_j|n_k}^{\text{eq}}+G^{\text{eq}}+E_{n_j|n_k}^{\text{eff}}-G^{\text{eff}}\right]\end{aligned} \tag{2.28}$$

As we sum over all possible transitions, the total entropy production is:

$$\begin{aligned}\dot{S}_{total}&=\sum_{n_i,n_j,n_k}J(n_i,n_j\to n_j,n_k)\left[\delta\mu-E_{n_j|n_k}^{\text{eq}}+G^{\text{eq}}+E_{n_j|n_k}^{\text{eff}}-G^{\text{eff}}\right]\\&=\langle\dot{N}\rangle\sum_{n_j,n_k}P_{inside}^{N}(n_j,n_k)\left[\delta\mu-E_{n_j|n_k}^{\text{eq}}+G^{\text{eq}}+E_{n_j|n_k}^{\text{eff}}-G^{\text{eff}}\right]\\&=\langle\dot{N}\rangle\left[\delta\mu-\langle E^{\text{eq}}\rangle+G^{\text{eq}}+\langle E^{\text{eff}}\rangle-G^{\text{eff}}\right]\\&=\langle\dot{N}\rangle(\delta\mu-\epsilon_{diss})\end{aligned} \tag{2.29}$$

Here $\epsilon_{diss}=\langle E^{\text{eq}}\rangle-\langle E^{\text{eff}}\rangle-G^{\text{eq}}+G^{\text{eff}}$. Alternatively, we can write the left terms of Eq. 2.27 and 2.26 to:

$$\begin{aligned}&\ln\left(\frac{P_{ss}^{N}(n_i,n_j,n_k)}{P_{ss}^{N}(n_i,n_j)}\right)=\ln\left(\frac{P_{sys}^{ss}(n_i|n_j)P_{ss}^{N}(n_j,n_k)}{P_{ss}^{N}(n_i,n_j)}\right)=\ln\left(\frac{P_{ss}^{N}(n_j,n_k)}{\sum_{n_i}P_{ss}^{N}(n_i,n_j)}\right)\\&=\ln\left(P_{sys}^{ss}(n_j|n_k)\right)+\ln\left(\frac{\sum_{n_j}P_{ss}^{N}(n_j,n_k)}{\sum_{n_i}P_{ss}^{N}(n_i,n_j)}\right)=\ln\left(P_{sys}^{ss}(n_j|n_k)\right)+\ln\left(\frac{P_{ss}^{N}(n_k)}{P_{ss}^{N}(n_j)}\right)\end{aligned} \tag{2.30}$$

$$\begin{aligned}\ln\left(P_{gen}(n_k|n_j)\frac{k(n_i,n_j\to n_j,n_k)}{k(n_i,n_j\leftarrow n_i,n_k)}\right) &= \delta\mu + \ln\left(\frac{P^N_{eq}(n_i,n_j,n_k)}{P^N_{eq}(n_i,n_j)}\right)\\ &= \delta\mu + \ln\left(P^{eq}_{sys}(n_j|n_k)\right) + \ln\left(\frac{P^N_{eq}(n_k)}{P^N_{eq}(n_j)}\right)\end{aligned} \tag{2.31}$$

The terms $\ln\left(\frac{P^N_{eq}(n_k)}{P^N_{eq}(n_j)}\right)$ and $\ln\left(\frac{P^N_{ss}(n_k)}{P^N_{ss}(n_j)}\right)$ will sum up to 0 when we add all the contribution from all the currents. So the total entropy production reduces to:

$$\dot{S}_{total} = \langle\dot{N}\rangle\left[\delta\mu - \sum_{n_k} P^N_{ss}(n_k)D\left(P^{ss}_{sys}(n_j|n_k)||P^{eq}_{sys}(n_j|n_k)\right)\right] \tag{2.32}$$

Eq. 2.29 and Eq. 2.32 say that to calculate the total entropy of the production we don't need to obtain all the individual edgewise entropy productions but simply the steady state and equilibrium state of the system together with the driving force behind the process.

2.5 The Thermodynamics Uncertainty Relations

The thermodynamics uncertainty relation (TUR) is one of the most intriguing results from the field of stochastic thermodynamics. It describes how a process's dissipation bounds all its current fluctuation. First discovered by Barato and Seifert [30], the TUR was later proven in [21] through the use of large deviation theory. Briefly, it is shown that the rate function of an arbitrary current j_d of a Markov process satisfies the inequality:

$$I(j_d) \geq \frac{(j_d - j^\pi_d)^2}{4(j^\pi_d)^2}\Sigma^\pi \tag{2.33}$$

Here Σ^π is the entropy production of the system at steady state, $I(j_d)$ is the rate function of j_d and $j_d = \sum_{y<z} d(y,z)j(y,z)$ where $j(y,z)$ is the current between nodes y, z and $d(y,z)$ are arbitrary constants that determine j_d. j^π_d is the average steady state current. The rate

function can then be further expanded into:

$$I(j_d) \approx \frac{2(j_d - j_d^\pi)^2}{Var(j_d)} \tag{2.34}$$

Using 2.33 and 2.34, we arrive at the TUR:

$$\Sigma^\pi \geq \frac{2\langle j_d^\pi \rangle^2}{Var(j_d^\pi)} \tag{2.35}$$

Using the above TUR, we can predict the entropy production of a process without the full knowledge of the details of the system. Indeed, with its simplicity and generality, the TUR has been applied to different systems and further extended to systems with time-dependent drive and systems with unidirectional transitions. [24, 31]

2.6 The Design Principles

We now have all the ingredients for our design principles. The first design principle involves the form of the entropy production in Eq. 2.29 and the second law of thermodynamics which states that the entropy production has to be positive. Since the system is growing: $\langle \dot{N} \rangle > 0$, we can simplify the second law into:

$$\delta\mu \geq \epsilon_{diss} \tag{2.36}$$

This equation tells us the minimum energy required to transform an assembly with an equilibrium energy landscape E^{eq} to an assembly with an effective energy landscape E^{eff}. Next, we use the TUR with the current $j_d^\pi = \langle \dot{N} \rangle$:

$$\delta\mu \geq \epsilon_{diss} + \frac{2\langle \dot{N} \rangle}{Var(\dot{N})} \tag{2.37}$$

Equations 2.36 and 2.37 are our main results. In the following chapters, we will explore how to use these results in various systems.

CHAPTER 3

APPLICATIONS TO LATTICE SYSTEMS

3.1 Introduction

This chapter will apply what we learn from the last chapter to lattice systems: the growing of 1D and 2D assembly. For the 1D assembly, we will first examine whether the reduced master equations from the last chapter 2 can produce the same results from kinetic Monte Carlo simulation with the full probabilities. We will then investigate how the design principles: Eq. 2.36 and Eq. 2.37 can be used to predict how driving forces change the correlation length of the system without solving the problem directly. Similarly, for the 2D polymer, we will demonstrate that the bounds can be used to predict a phase transition of the model.

3.2 Growing of 1D Assembly

We first look at the application of the last chapter technique to a system of a growing 1D assembly growing in a bath containing two types of particles: red and blue, as depicted in Fig. 3.1. As a start, let's first look at the case that there is no bias between the particles in the bath. The bias here can come from different concentrations of monomers in the bath or different energy interactions. We will then extend the cases to different biases for each particle later. In the assembly, only nearest neighbors can interact with energy ϵ_s if they are the same and ϵ_d if they are different. We then add particles into the assembly with rate $\exp(\mu)$ and remove them with the rate $\exp(-\epsilon_i)$ (i can be s or d depending on the configuration of the particle). The chemical potentials, μ, of particles, are related to its concentration, c, by the relation: $\mu = \ln(c)$. As the assembly grows, we only allow particles to attach or detach at the outermost block of the polymer.

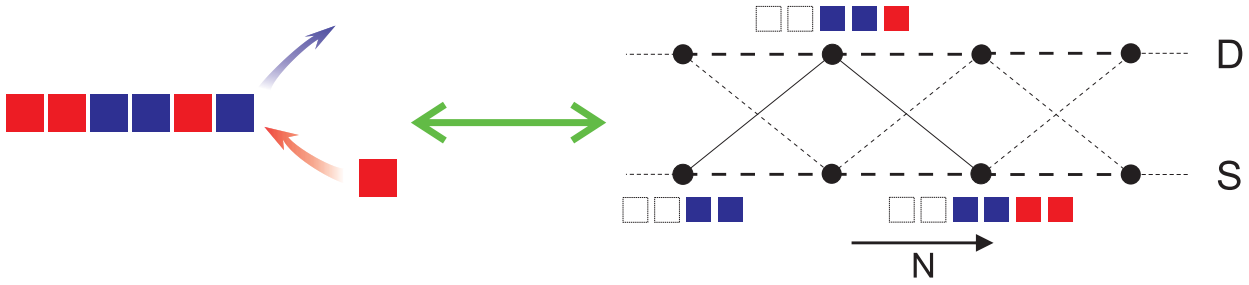

Figure 3.1: Application of the bounds to 1D lattice growth model. Left: Schematic of the 1D assembly growth process. The assembly is assembled from a bath composed of two particle types (Red and Blue). Right: Schematic of the Markov state model. This Markov state model resolves the nature of terminal bond in the self-assembled system (vertical rungs), $S \equiv$ bond between like particles and $D \equiv$ bond between unlike particles, and the number of particles in the self assembled system (horizontal axis).

3.2.1 Setting Up The Master Equations

We will now set up the master equations for the Growing 1D Lattice Assembly. Because the concentrations and energy interactions between the particles are the same in this case, we can simplify the master equations with:

$$\begin{aligned} P^N(R,B) &= P^N(B,R) = \frac{P^N(D)}{2} \\ P^N(R,R) &= P^N(B,B) = \frac{P^N(S)}{2} \\ P^N(R,R) &+ P^N(R,B) = 0.5 \\ P^N(B,B) &+ P^N(B,R) = 0.5 \end{aligned} \tag{3.1}$$

Here R/B stands for red/blue particle. S/D stands for same/different particles. Following the procedures in the last chapter, we transform the master equations with full probabilities to reduced ones as shown in Fig. 3.2:

$$\frac{dP^N(D)}{dt} = -(c + e^{-\epsilon_d})P^N(D) + P^N(D)(e^{-\epsilon_d}P^N(D) + e^{-\epsilon_s}P^N(S)) + \frac{c}{2}(P^N(D) + P^N(S)) \tag{3.2}$$

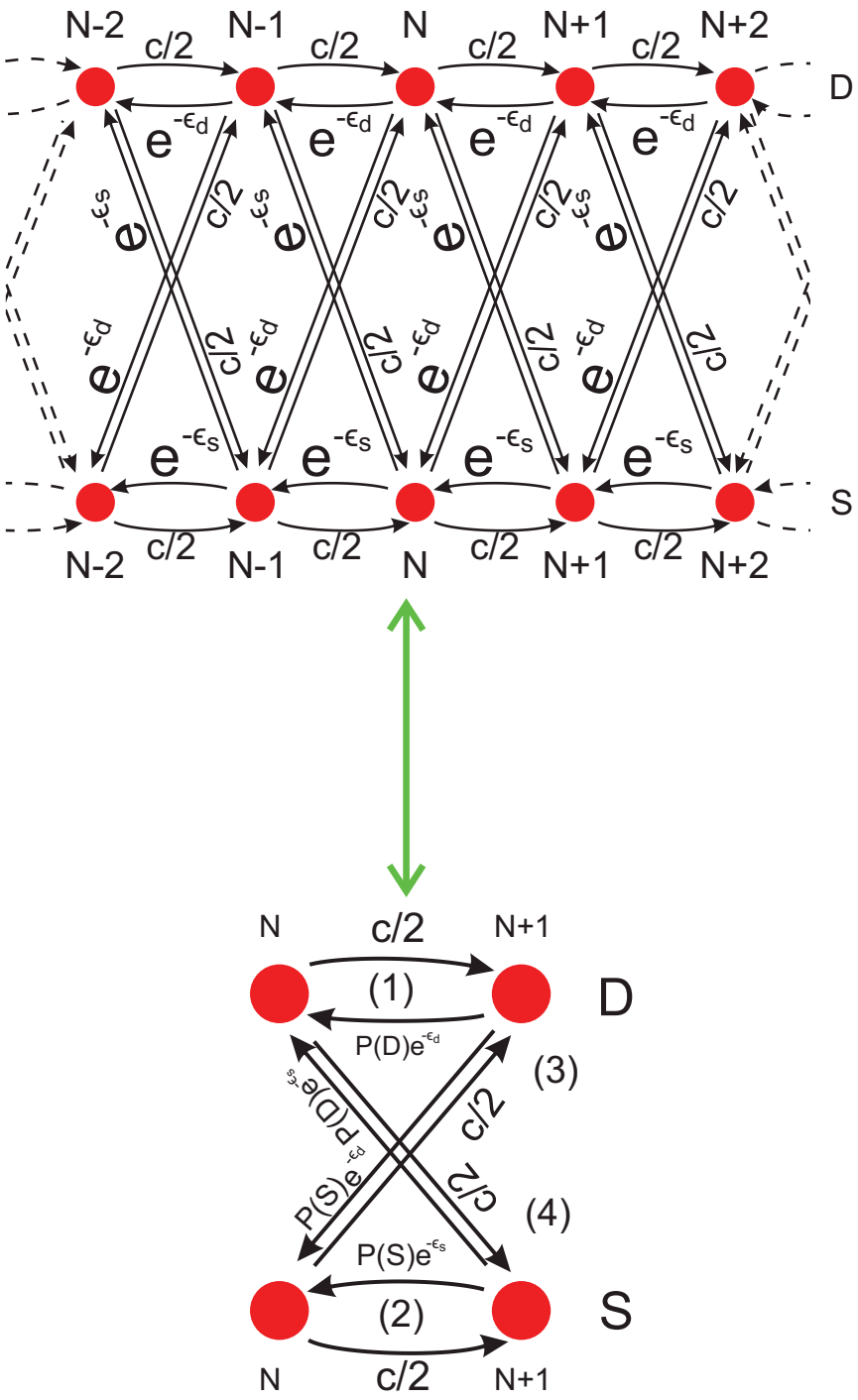

Figure 3.2: Schematics of the Markov networks. The circles are all possible states of the polymer. The circles in the first row represent the states in which two neighbor particles are different. The circles in the second row represent the states in which two neighbor particles are the same. Only horizontal and diagonal transitions are allowed to reflect the fact that the particle cannot change from one type to another type. Up: The full Markov network of the Growing 1D Polymer model. Down: The reduced Markov network with modified growth rates.

$$\frac{dP^N(S)}{dt} = -(c + e^{-\epsilon_s})P^N(S) + P^N(S)(e^{-\epsilon_d}P^N(D) + e^{-\epsilon_s}P^N(S)) + \frac{c}{2}(P^N(D) + P^N(S)) \tag{3.3}$$

When the system is at a steady-state, the above differential equations are set to 0. Together with the condition: $P^N(S) + P^N(D) = 1$, we can solve for $P^N(S)$ and $P^N(D)$ as long as the system is not shrinking. When the system does not grow on average, it is at equilibrium, and the Markov network satisfies detail balance; that is, all the currents between nodes have to be zero. With the detail balance condition, we can solve for $c_{eq}, P^N_{eq}(S), P^N_{eq}(D)$ for the equilibrium system. For this system, these quantities equal:

$$c_{eq} = \frac{2}{\exp(\epsilon_s) + \exp(\epsilon_d)} \tag{3.4}$$

$$P^N_{eq}(D) = \frac{\exp(\epsilon_d)}{\exp(\epsilon_s) + \exp(\epsilon_d)} \tag{3.5}$$

$$P^N_{eq}(S) = \frac{\exp(\epsilon_s)}{\exp(\epsilon_s) + \exp(\epsilon_d)} \tag{3.6}$$

3.2.2 Connection to the 1D Ising Model

By assign the red particle with value 1 and the blue particle with value -1, we can write the energy function of the assembly into:

$$E = -\sum_i^N \left[\frac{\epsilon_s - \epsilon_d}{2} s_i s_{i+1} + \frac{\epsilon_s + \epsilon_d}{2}\right] \tag{3.7}$$

This energy is equivalent to the 1D-Ising model with magnetic coupling constant $J = (\epsilon_s - \epsilon_d)/2$ with an extra term $(\epsilon_s + \epsilon_d)/2$. Thus, when the system is at equilibrium, it can be completely characterized by the 1D Ising model with a partition function:

$$Z = \exp\left(\frac{\epsilon_s + \epsilon_d}{2}\right)[\exp(J) + \exp(-J)] \tag{3.8}$$

The $c_{eq}, P^N_{eq}(S), P^N_{eq}(D)$ above can be rewritten as:

$$c_{eq} = \frac{2\exp(-\frac{\epsilon_s+\epsilon_d}{2})}{\exp(\frac{\epsilon_s-\epsilon_d}{2}) + \exp(\frac{\epsilon_d-\epsilon_s}{2})} = \frac{2\exp(-\frac{\epsilon_s+\epsilon_d}{2})}{\exp(J)+\exp(-J)} = 2/Z \tag{3.9}$$

$$P^N_{eq}(D) = \frac{\exp(-J)}{\exp(J)+\exp(-J)} \tag{3.10}$$

$$P^N_{eq}(S) = \frac{\exp(J)}{\exp(J)+\exp(-J)} \tag{3.11}$$

3.2.3 Comparison to Kinetic Monte Carlo Simulation

We will now perform Kinetic Monte Carlo simulation for the growing of the 1D polymer using the above rules. We will use the average domain length as an observable in the simulation, which can be connected to $P(S)$:

$$\xi = 1 + P(S) + P(S)^2 + ... = \frac{1}{1-P(S)} = 1 + \exp(2J) \tag{3.12}$$

In Fig. 3.3(a), we compare the relation between $\delta\mu$ and ξ predicted by the effective model with results from simulations. The agreement between the two is excellent. In Fig. 3.3(b), we show that the average growth rate predicted by the effective model is in excellent agreement with the results from simulations. The variance of growth rate predicted by the effective model exhibits minor deviations from the simulation results, especially close to equilibrium. Still, the agreement is excellent otherwise (see Fig. 3.4 (a)). This might be because the current simulations were insufficient in sampling the system with a long correlation length near equilibrium. As we decrease the equilibrium correlation length of the system from $\xi_0 = 100$ to $\xi_0 = 5$, the variance predicted by the effective model fits much better with one from simulations as shown in Fig. 3.4 (b).

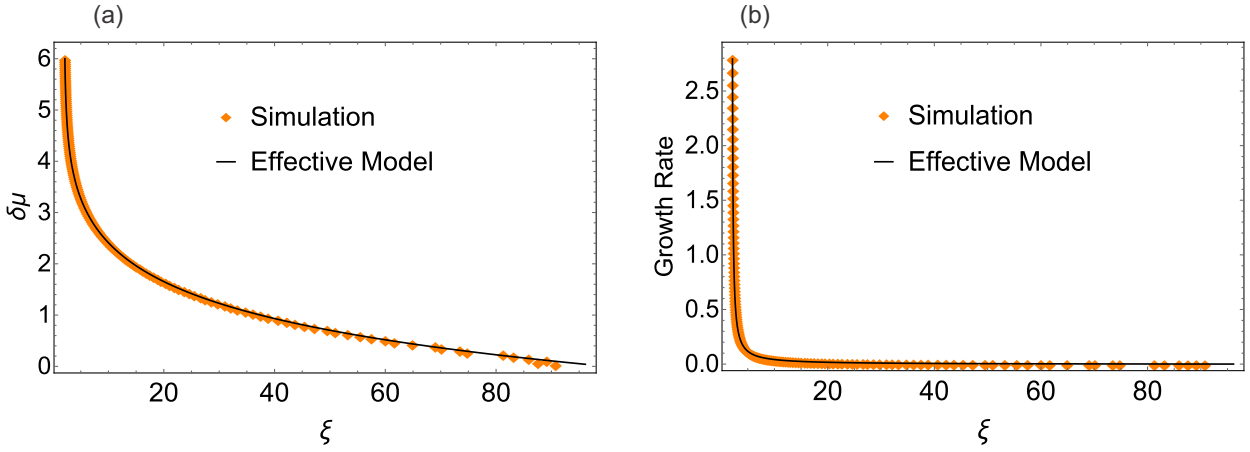

Figure 3.3: Comparison between the results from effective model and simulations (a)$\delta\mu$ vs. ξ at $\xi_0 = 100$ (b) Growth Rate vs. ξ at $\xi_0 = 100$

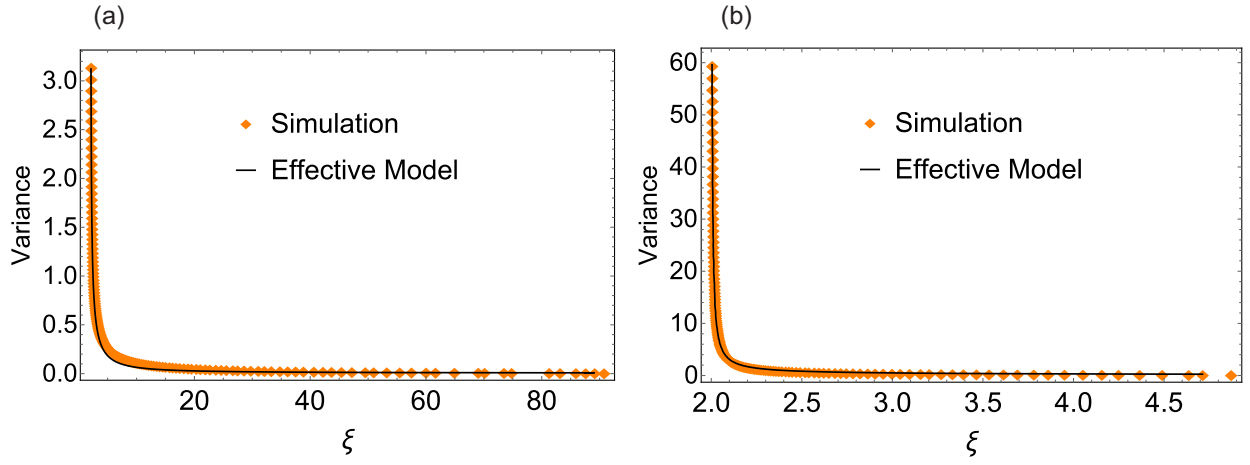

Figure 3.4: Comparison between the results from effective model and simulations (a) Variance vs. ξ at $\xi_0 = 100$ (b) Variance vs. ξ at $\xi_0 = 5$

3.2.4 Entropy Production Formula

Next, we show that the entropy production rate from the Markov state caricature equals that predicted by our thermodynamic result,

$$\dot{S}_{tot} = \langle \dot{N} \rangle \left[\delta\mu - \langle E^{\mathrm{eq}} \rangle + G^{\mathrm{eq}} + \langle E^{\mathrm{eff}} \rangle - G^{\mathrm{eff}} \right] \tag{3.13}$$

Let's look at the transitions of the effective model from state N to state N+1 (Fig. 3.2). For easy algebra manipulation, we group all possible transitions of the effective model into four different types, as shown in Fig. 3.2. The entropy production of four transitions can be written down as

$$\dot{S}_1 = \left(P^N(D)\frac{c}{2} - P^N(D)^2 e^{-\epsilon_d} \right) \ln\left(\frac{c/2}{P^N(D)e^{-\epsilon_d}} \right) \tag{3.14}$$

$$\dot{S}_2 = \left(P^N(S)\frac{c}{2} - P^N(S)^2 e^{-\epsilon_s} \right) \ln\left(\frac{c/2}{P^N(S)e^{-\epsilon_s}} \right) \tag{3.15}$$

$$\dot{S}_3 = \left(P^N(S)\frac{c}{2} - P^N(D)P^N(S) e^{-\epsilon_d} \right) \ln\left(\frac{c/2}{P^N(D)e^{-\epsilon_d}} \right) \tag{3.16}$$

$$\dot{S}_4 = \left(P^N(D)\frac{c}{2} - P^N(S)P^N(D) e^{-\epsilon_s} \right) \ln\left(\frac{c/2}{P^N(S)e^{-\epsilon_s}} \right) \tag{3.17}$$

Add all these transitions together and we obtain:

$$\begin{aligned}
\dot{S}_{total} &= (\frac{c}{2} - P^N(D)e^{-\epsilon_d})\ln\left(\frac{c/2}{P^N(D)e^{-\epsilon_d}} \right) + (\frac{c}{2} - P^N(S)e^{-\epsilon_s})\ln\left(\frac{c/2}{P^N(S)e^{-\epsilon_s}} \right) \\
&= (c - P^N(S)e^{-\epsilon_s} - P^N(D)e^{-\epsilon_d}) \Bigg(\ln(\frac{c}{c_{eq}}) + \frac{(\frac{c}{2} - P^N(D)e^{-\epsilon_d})}{(c - P^N(S)e^{-\epsilon_s} - P^N(D)e^{-\epsilon_d})} \ln(\frac{c_{eq}/2}{P^N(D)e^{-\epsilon_s}}) \\
&+ \frac{(\frac{c}{2} - P^N(S)e^{-\epsilon_s})}{(c - P^N(S)e^{-\epsilon_s} - P^N(D)e^{-\epsilon_d})} \ln(\frac{c_{eq}/2}{P^N(S)e^{-\epsilon_d}}) \Bigg)
\end{aligned} \tag{3.18}$$

The term $c - P^N(S)e^{(-\epsilon_s)} - P^N(D)e^{(-\epsilon_d)}$ in Eq. 3.18 can be considered as the average

velocity of the particle or the average growth rate of assembly. From the last chapter, we also have:

$$\frac{(\frac{c}{2} - P^N(D)e^{-\epsilon_d})}{(c - P^N(S)e^{-\epsilon_s} - P^N(D)e^{-\epsilon_d})} = P^N(D) \tag{3.19}$$

$$\frac{(\frac{c}{2} - P^N(S)e^{-\epsilon_s})}{(c - P^N(S)e^{-\epsilon_s} - P^N(D)e^{-\epsilon_d})} = P^N(S) \tag{3.20}$$

With this, the total entropy production becomes:

$$\begin{aligned}
\dot{S}_{total} &= \langle \dot{N} \rangle \left(\ln(\frac{c}{c_{eq}}) + P^N(S)\ln(\frac{c_{eq}/2}{P^N(S)e^{-\epsilon_s}}) + P^N(D)\ln(\frac{c_{eq}/2}{P^N(D)e^{-\epsilon_d}}) \right) \\
&= \langle \dot{N} \rangle \left(\ln(\frac{c}{c_{eq}}) + P^N(S)\ln(\frac{P^N_{eq}(S)}{P^N(S)}) + P^N(D)\ln(\frac{P^N_{eq}(D)}{P^N(D)}) \right) \\
&= \langle \dot{N} \rangle \left(\delta\mu + (1 - \frac{1}{\xi})\ln(\frac{\xi_{eq} - 1}{\xi - 1}) + \ln(\frac{\xi}{\xi_{eq}}) \right)
\end{aligned} \tag{3.21}$$

We have used Eq. 3.12 in the last line to convert the entropy production to the domain length, an observable for our system. Next, we will use our approach to calculate the entropy production. Since, at equilibrium, our system is already mapped to the 1D Ising model, we will use the 1D-Ising model to describe the configuration of the non-equilibrium system but with a modified J_{eff}. Using the 1D-Ising model, we can readily write $E^{\text{eff}}, E^{\text{eq}}, G^{\text{eff}}, G^{\text{eq}}$:

$$\langle E^{\text{eff}} \rangle = -\frac{\ln(\xi - 1)}{2}\left(1 - \frac{2}{\xi}\right) \tag{3.22}$$

$$\langle E^{\text{eq}} \rangle = -\frac{\ln(\xi_{eq} - 1)}{2}\left(1 - \frac{2}{\xi}\right) \tag{3.23}$$

$$G^{\text{eff}} = -\ln(\xi) + \frac{\ln(\xi - 1)}{2} \tag{3.24}$$

$$G^{\text{eq}} = -\ln(\xi_{eq}) + \frac{\ln(\xi_{eq} - 1)}{2} \tag{3.25}$$

Plug these into Eq. 2.29 will give us Eq. 3.21 indicating the validity of our framework. Next,

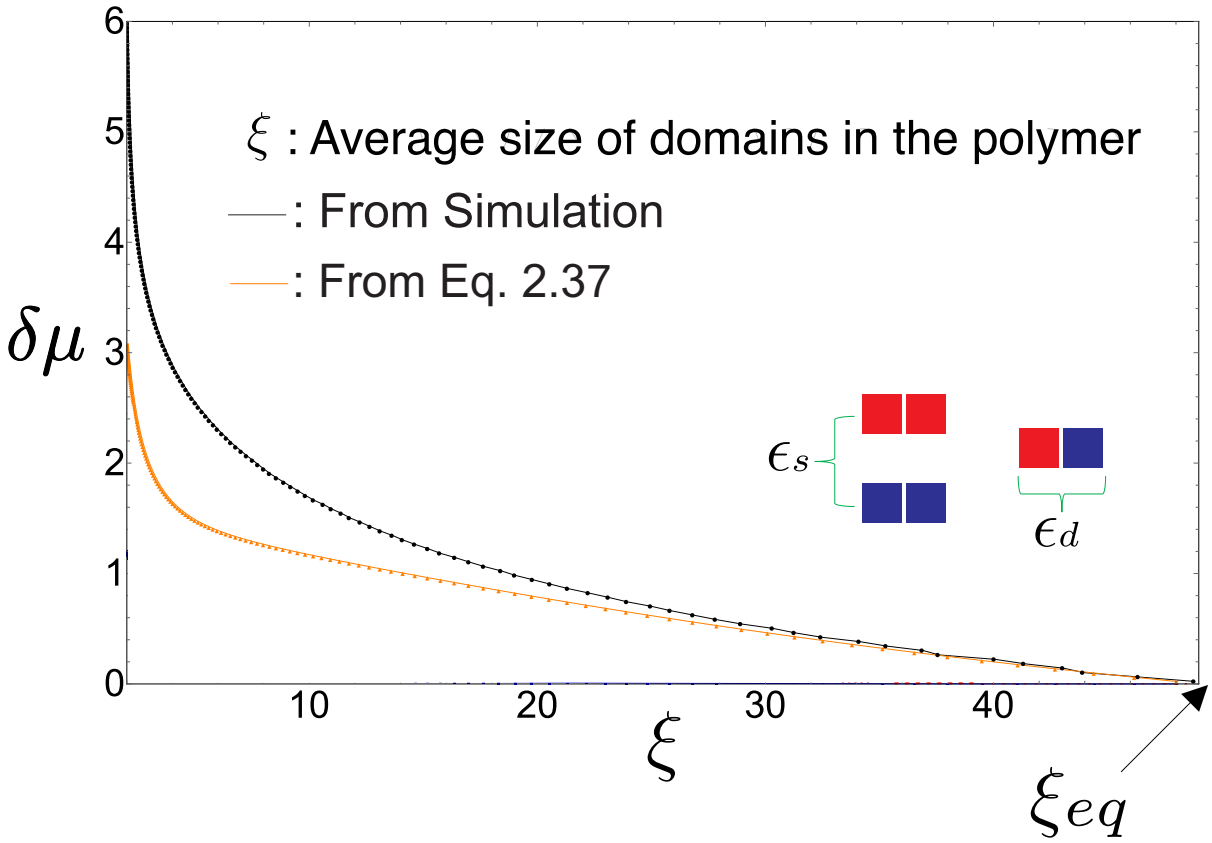

Figure 3.5: Application of the bounds to 1D assembly growth model: Comparison between the lower bounds of $\delta\mu$ obtained from Eq. 2.37 and the value of $\delta\mu$ obtained from simulations. The equilibrium domain length, ξ_0, for this plot is 50. Our thermodynamic bounds are valid and in spite of their minimal nature, do reasonable job of predicting the compositional fluctuations in the assembly.

in Fig. 3.5(c), we demonstrate how the thermodynamic bound in Eq. 2.37 for a particular kinetic model of polymer growth [32] can be used to predict the necessary chemical potential, $\delta\mu$, to transform the system with an equilibrium domain length ξ_{eq} to a new one, ξ.

These demonstrations prove the theoretical validity and effectiveness of our bound and pave the way for applications to more complex systems. Specifically, for systems with more than two particle types or particles with longer-ranged interactions, it is more convenient to express ϵ_{diss} in terms of the actual E^{eq} and effective E^{eff} interaction Hamiltonians. While effective Markov state caricatures for such systems can be complex and analytically intractable, our thermodynamic bounds are easily accessible and provide instrumental intuition for the

compositional fluctuations of the non-equilibrium assembly. We now demonstrate these ideas by considering a two-dimensional analog of the fiber growth process described above [33] (Fig. 3.6 (a))

3.3 Non-equilibrium two dimensional self assembly process

As a natural generalization of the one-dimensional assembly model, we imagine a two-dimensional assembly growing at one end as described in Fig 3.6 (a). We again imagine two particle types with interactions between like particles set by the energy scale ϵ_s and interactions between unlike particles set by the energy scale ϵ_d. When the chemical potential is set to the intensive equilibrium free energy of the assembly, $\mu_{\text{coex}} \approx 2\epsilon_s - k_{\text{B}}T \ln 2$, the assembly doesn't grow on average. Assigning spin $s = 1$ to the red particles and spin $s = -1$ to the blue particles, the statistics of the compositional fluctuations in the equilibrium assembly are equivalent to that of a 2D Ising model with coupling constant $J = \frac{\epsilon_s - \epsilon_d}{2}$. We will work in regimes where the coupling constant is above the critical coupling constant of the 2D Ising model, $J > J_c \approx 1/2.26$. We are interested in the statistics of compositional fluctuations as the growth rate of the assembly is tuned by changing the chemical potential.

We begin by assuming that the compositional fluctuations in the growing assembly can be described by an effective nearest-neighbor coupling constant J_{eff}. We performed simulations in which we extracted the value of J_{eff} as a function of the excess chemical potential $\delta\mu$ by measuring the assembly's average magnetization and converting it using Onsager's solution. The values of J_{eff} obtained from simulations are plotted in Fig. 3.7. As shown in Fig. 3.7, when the excess chemical potential is close to a certain value $\delta\mu_c$, the value of the effective coupling constant computed from simulations reaches the critical value of the two dimensional Ising model, J_c.

Using Eq. 2.36 and Eq. 2.37 we analytically computed a lower bound J_b on the values of the effective coupling constant as a function of $\delta\mu$. In Fig. 3.7, we plot J_b for various

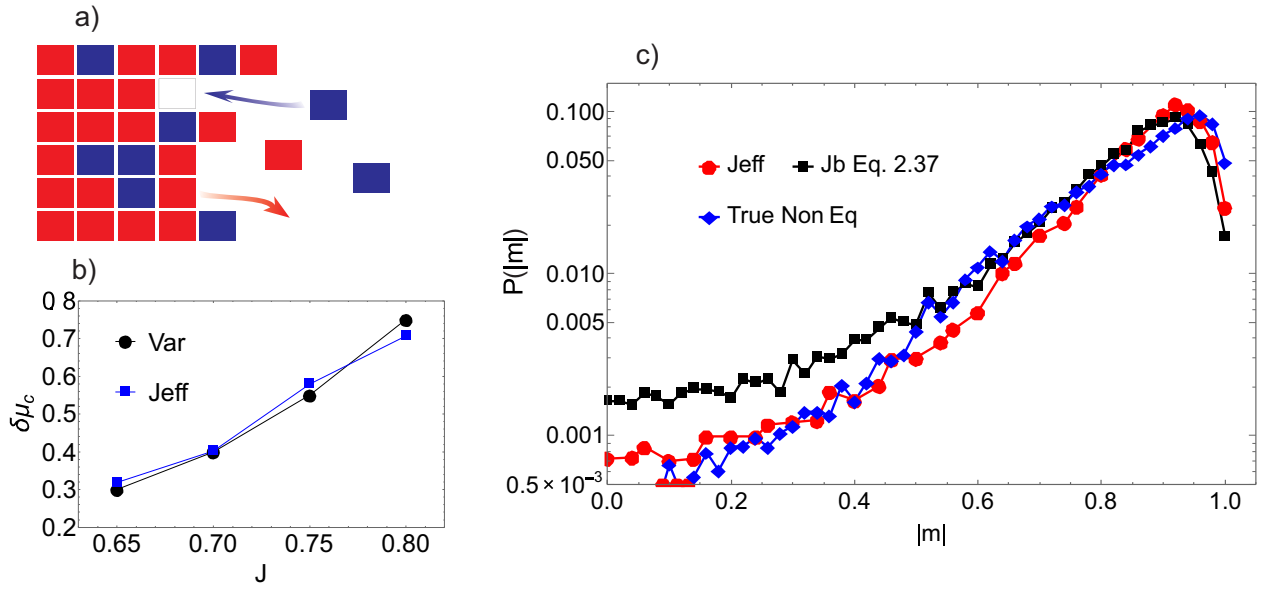

Figure 3.6: Application of the bounds to the non-equilibrium two-dimensional growth process (a) We assemble a two-dimensional structure from a particle bath containing red and blue particles. The energy of interaction between similar particles is ϵ_s while that between dissimilar particles is ϵ_d. As discussed in the text, when the assembly is grown at equilibrium, the statistics of compositional fluctuations in the assembly are equivalent to that of an Ising magnet with coupling constant $J = \frac{\epsilon_s - \epsilon_d}{2}$. (b) We compare the value of critical driving force $\delta\mu_c$ obtained by computing J_{eff} using the Onsager solution, as described in the main text, with that obtained by computing the variance of magnetization fluctuations as described in ref. [1]. The agreement between the two estimates confirms that the system has anomalously large fluctuations at the non-equilibrium critical driving force we identify. (c) We calculate the probability of magnetization from the non-equilibrium simulations and compare it with the distribution obtained by sampling an Ising model at Jeff and Jb from Eq. 2.37. These data were obtained for $J = 0.65$ and $\delta\mu = 0.1$. The system grows rapidly for these parameters, as evidenced by the value of J_{eff} computed for these parameters. We expect the system to be far from the linear response. The close agreement between the distribution predicted by J_b and the non-equilibrium distribution, even far from the mean, suggests that our theoretical bound accurately captures the fluctuations in this non-equilibrium system.

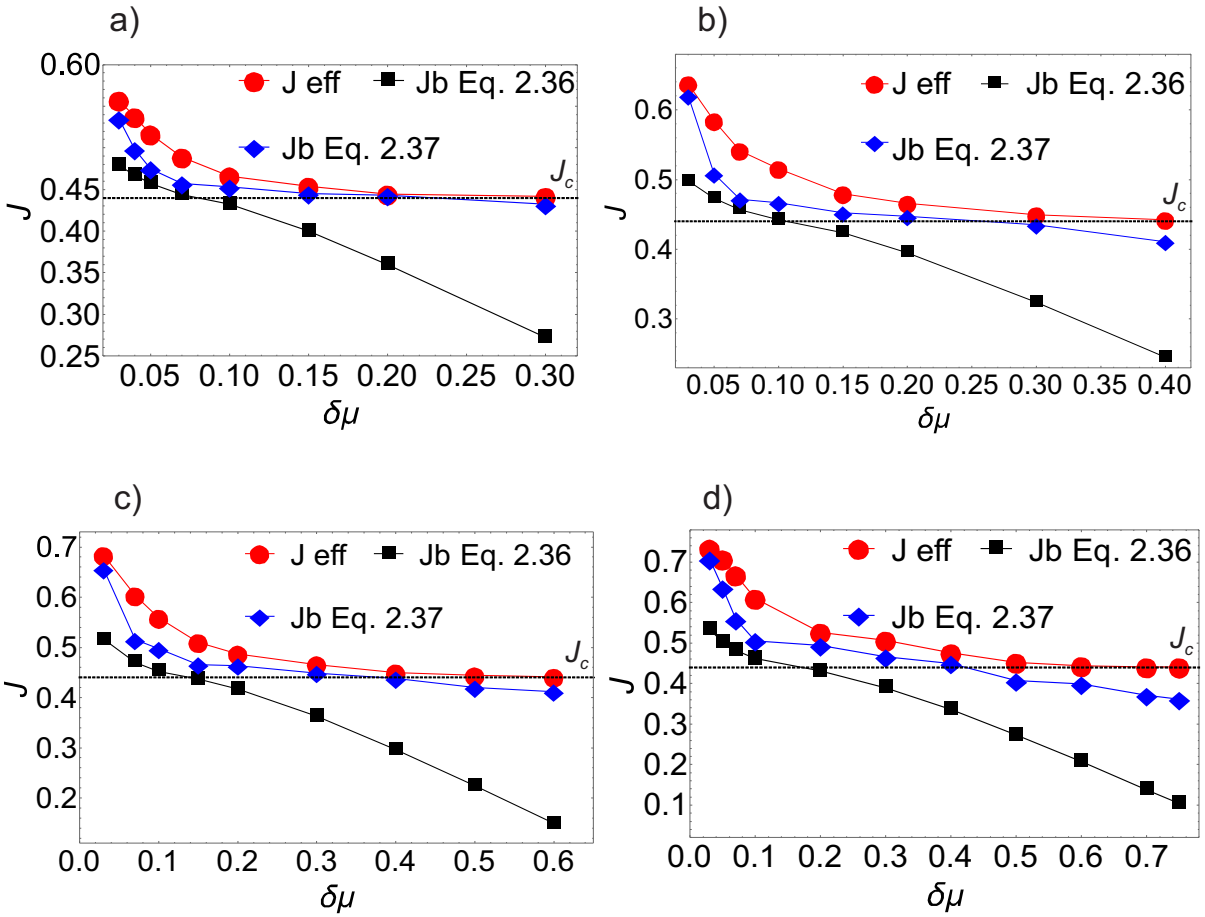

Figure 3.7: Comparison between Jeff from the simulations and Jb from Eqs. 2.36 and 2.37 for different values of J: J = 0.65 (A), J = 0.70 (B), J = 0.75 (C), and J = 0.80 (D).

values of the excess chemical potential. The bound obtained from Eq. 2.36 does a reasonable job of predicting the effective coupling constant. Including information about higher order cumulants again improves the bound and provides a close to an accurate estimate of the effective coupling constant J_{eff}. In particular, the bound obtained by including information from the higher cumulants (Eq. 2.37) does particularly well for values of $\delta\mu$ around the critical value, $\delta\mu_c$. This close agreement between the bound predicted by theory and the effective value computed from simulations in the critical regime is surprising given the minimal nature of our theory.

3.4 Applications and Conclusion

Using the framework of stochastic thermodynamics and physically justified approximations, we have put forward a general predictive framework for non-equilibrium self-assembly. Our central results, Eq. 2.36 and Eq. 2.37 are built around a simple and intuitive expression for entropy production in non-equilibrium self assembly process. This expression relates compositional fluctuations in the self assembled system to the chemical potential excess driving assembly process. Given a set of programmed interactions between particles and structures specified by the energy function E^{eq}, our central result constrains the set of allowed structures that can be obtained under a non-equilibrium drive. A unique feature of our result is its thermodynamic character: the bound doesn't depend on the details of the kinetic model chosen. Many recent theoretical and experimental studies have postulated that non-equilibrium protocols can potentially be used to overcome bottlenecks and enhance the yield of desired self-assembled structures [34]. Our framework is ideally suited to verify these postulates and explore connections between energy consumption and improved yield of target structures.

We anticipate that our results will find important applications in studies of crystal nucleation [19], self-assembly of metal organic frameworks [35], non-equilibrium roughening

transitions, and the synthesis of nano crystals using DNA and other biopolymers as building materials. In all these instances, the assembly process can occur far from equilibrium depending on the effective chemical potentials imposed. Our result provides a bound on the chemical potentials under which the desired structures can be robustly obtained even far from equilibrium. It also offers crucial intuition into how the equilibrium landscape [8, 6] and the capacity of the system to store structures [36] are modified under non-equilibrium conditions.

Finally, the variational structure of our central results provides a framework to optimally tune the chemical potential driving forces to maximize the yield of desired structures. In this context, our results complement recently derived theoretical results that suggest a heterogeneous set of excess chemical potentials is crucial for robust nucleation of large complex nanoscale assemblies using DNA origami [37, 38].

A mismatch of chemical potentials provides the non-equilibrium driving force in Eq. 2.36. Our results also apply to non-equilibrium error correction mechanisms for biopolymer assembly in which the assembly process is driven by consumption of energy rich ATP/GTP molecules. In such instances, the $\delta\mu$ term is replaced by the appropriate average energy consumption rate. In these biophysical applications, the non-equilibrium driving force generates structures that posses correlations greater than those in equilibrium. While such fibers are not achievable with the kinetic protocols described above, the thermodynamic nature of our bounds allows their application to these biophysical error correction mechanisms. Indeed, Sartori et al [39] have recently derived a similar bound for a specific model of kinetic proofreading. Our general thermodynamic bounds, particular that in Eq. 2.37 can elucidate the tradeoffs between speed accuracy and energy consumption in such non-equilibrium biochemical replication processes.

CHAPTER 4

APPLICATION TO SIMPLE MEMBRANE MODEL

4.1 Introduction

Non-equilibrium forcing can be used to uncover new strategies for self-assembly and organization [40, 41, 42, 33]. In biophysical contexts, it has been established that non-equilibrium forces play a crucial role in suppressing rogue fluctuations and enhancing the fidelity of molecular recognition [43, 42, 44, 45, 46], support robust oscillations crucial for the maintenance of circadian rhythms [47], and drive sensory adaptation processes [41, 42]. Non-equilibrium forces also play an important role in modulating cell shape and cell membrane fluctuations [48, 49]. For instance, local changes in surface tension or lateral pressure due to a spontaneous assembly of membrane proteins have been known to induce instabilities in membrane fluctuations [50, 51, 52, 53]. Such instabilities have been implicated as important precursors during cell division [48]. Non-equilibrium fluctuations are also important in cases where the cell membrane interacts with growing actin filaments. The important role played by such interactions in regulating the organization of the membrane has been well established. [54, 55].

In this chapter, with a simplified model of elastic membrane (Fig. 4.1), we will illustrate how the framework explored here can be used to investigate growth and morphological changes in membrane's growth [56, 57, 58, 59, 60, 61, 62, 63, 64, 65, 66, 67]. Our model consists of two-dimensional particles connected by elastic springs in a ring-like geometry (Fig 4.1) [61, 62, 63, 64, 65]. The ring assembly is allowed to exchange particles with a reservoir. The chemical potential of the reservoir controls the growth rate of the ring assembly and sets the non-equilibrium driving force in this system. This elastic model is adapted from an equilibrium model first introduced by Leibler and coworkers in Ref [61]. As demonstrated in Refs [61, 62, 63, 64, 65], despite their apparent simplicity, this class of

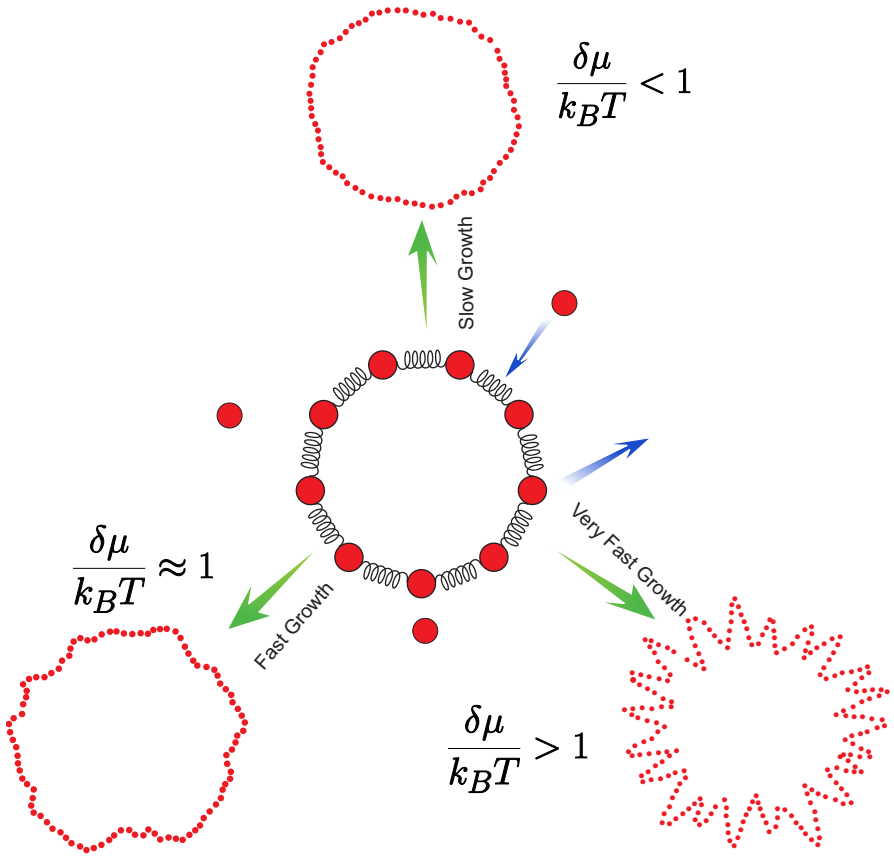

Figure 4.1: Schematic of the growing assembly. When the assembly grows slowly, its shape remains circular (top figure). As the assembly grows faster, its shape becomes more distorted (lower left) and ultimately it buckles into a star-shaped morphology (lower right).

elastic models possess many features [68, 61, 62, 63, 57, 58, 59, 64, 60, 69, 65] characteristic of three-dimensional membranes and can be used to obtain insights into how morphological changes in such systems can be excited under a non-equilibrium driving force.

Indeed, as we describe below, our numerical analysis shows that the elastic ring's effective surface tension and bending rigidity get modified under non-equilibrium growth conditions. Further, beyond a critical chemical potential driving force, the effective surface tension of the elastic ring is renormalized to zero, and the elastic ring exhibits a buckling instability and undergoes a non-equilibrium morphological transformation (Fig. 4.1). Such instabilities have been observed in experiments investigating the growth of model lipid membranes [59] and can potentially have implications for biophysical processes such as membrane fission and

endocytosis. We note that phenomenology similar to that described above can be observed in three-dimensional elastic membrane models in the later part of the chapter.

Using ideas from stochastic thermodynamics, we provide a thermodynamic prescription for how the non-equilibrium forces modify the surface tension and bending rigidity. The thermodynamic prescription only requires information about the magnitude of the non-equilibrium chemical potential driving force, the equilibrium surface tension and bending rigidity, the average rate of growth, and fluctuations in the growth rate. It is otherwise independent of the kinetic details of the growth process. The thermodynamic prescription is otherwise insensitive to any of the kinetic details used in the growth process. It provides bounds on the energetic requirements to induce morphological transformations such as the above-described non-equilibrium buckling transition.

4.2 Simulations and results

4.2.1 The Model and Simulation Move Set

Our model consists a system of particles in a ring like geometry interacting according to the energy,

$$E = \sum_{i}^{N} \frac{k_s}{2}(l_{i,i+1} - l_0)^2 + k_\theta(\theta_i - \pi)^2 \,, \tag{4.1}$$

where $l_{i,i+1}$ is the distance between particle i and particle $i+1$, l_0 is the equilibrium distance and θ_i is the angle that particle i makes with its neighbors. Fig. 4.2 describes the procedure used to simulate addition and removal moves in our numerical calculations. The initial configuration of the assembly is a circle consisting of N_0 particles with equal distance between them. Addition and removal events are chosen with equal probability. In an addition move, first a random particle in the assembly is chosen. As described in Fig. 4.2, an addition move is attempted in a region between the chosen random particle (B) and the next particle in the clockwise direction (C). The area of the region in which the addition is attempted

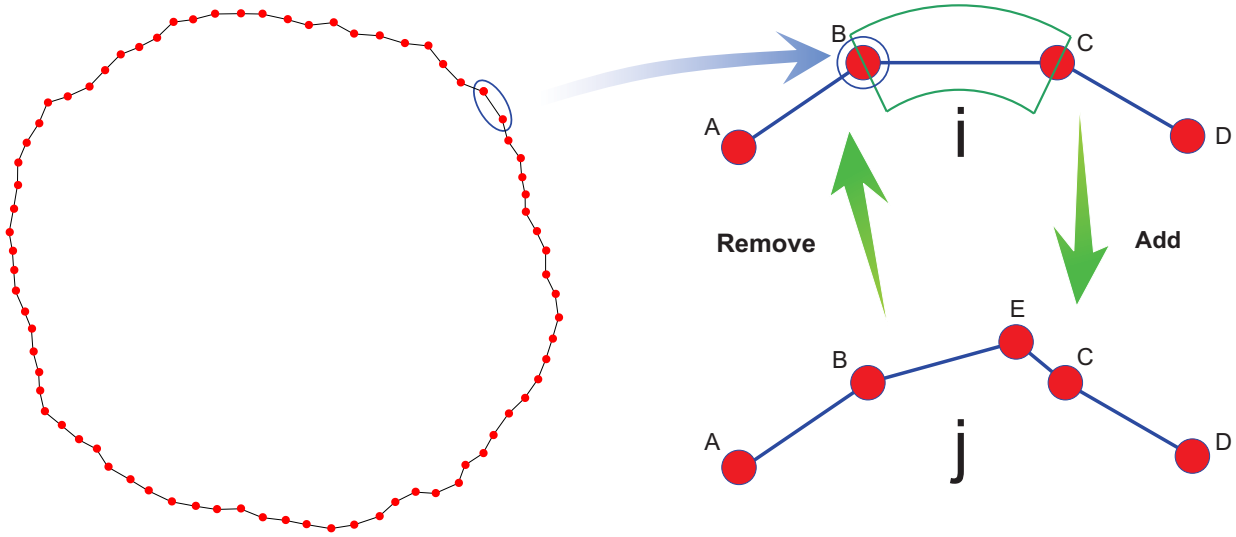

Figure 4.2: Schematic of the simulation's addition and removal moves. The addition rate is $W_{ij}^{N,N+1} = \frac{1}{NA}\text{Min}(\text{Exp}[\beta(-(\text{E}_\text{j} - \text{E}_\text{i}) + \mu), 1])$. The removal rate is $W_{ji}^{N+1,N} = \frac{1}{N+1}\text{Min}(\text{Exp}[\beta(-(\text{E}_\text{i} - \text{E}_\text{j}) - \mu)], 1)$. Here, A is the area of the arc which we keep constant $A = 4$, N is the number of particle in the assembly, $E_j = \frac{k_s}{2}(l_{BE} - l_0)^2 + \frac{k_s}{2}(l_{CE} - l_0)^2 + k_\theta(\widehat{ABE} - \pi)^2 + k_\theta(\widehat{ABE} - \pi)^2 + k_\theta(\widehat{ECD} - \pi)^2 + C$ and $E_i = \frac{k_s}{2}(l_{BC} - l_0)^2 + k_\theta(\widehat{ABC} - \pi)^2 + k_\theta(\widehat{BCD} - \pi)^2 + C$; C is the energy contribution of the other angles and strings

(denoted in Fig. 4.2) is kept a constant. An addition move is accepted with the probability $\mathrm{Min}(\mathrm{Exp}[\beta(-\Delta \mathrm{E} + \mu]), 1)$. In a removal move, a random particle is simply removed from the assembly with the probability $\mathrm{Min}(\mathrm{Exp}[\beta(-\Delta \mathrm{E} - \mu)], 1)$. Here $\beta = \frac{1}{k_B T}$. The transition rates of the simulations are:

$$W_{ij}^{N,N+1} = \frac{1}{AN}\mathrm{Min}(\mathrm{Exp}[\beta(-(\mathrm{E_j} - \mathrm{E_i}) + \mu)], 1) \tag{4.2}$$

$$W_{ji}^{N+1,N} = \frac{1}{N+1}\mathrm{Min}(\mathrm{Exp}[\beta(-(\mathrm{E_i} - \mathrm{E_j}) - \mu)], 1) \tag{4.3}$$

Here, i and j are used to denote the microstate the assembly is in. Thus, $W_{ij}^{N,N+1}$ is the transition that changes the assembly from state i to state j with a particle addition. $W_{ji}^{N+1,N}$ is the transition that the assembly goes from state j to i with a particle removal. A is the area in which we attempt to add a new particle which we keep constant $A = 4$, N is the total number of particles in the assembly, $E_j = \sum_n^{N+1} \frac{k_s}{2}(l_{n,n+1} - l_0)^2 + k_\theta(\theta_n - \pi)^2$, $E_i = \sum_n^{N} \frac{k_s}{2}(l_{n,n+1} - l_0)^2 + k_\theta(\theta_n - \pi)^2$, where n labels the particles in the ring, $l_{n,n+1}$ is the spring length between particle n and n+1, θ_n is the made by the bonds connecting the n^{th} particle. Monte-Carlo simulations are performed with these rules. Each Monte-Carlo step in the simulation is an attempt to add or remove a particle. Each simulation is run for at least 10^9 Monte-Carlo steps. For each value of $\delta\mu$, we generate at least 100 trajectories in this fashion and use this ensemble to measure the fluctuations of the membrane assembly as described in the main text.

4.2.2 Equilibrium dynamics

When the system is at equilibrium, we have the condition of detailed balance:

$$\begin{aligned} &P_i(l_{1,2}, l_{2,3}, ..., l_{N,1}, \theta_1, \theta_2, ..., \theta_N) W_{ij}^{N,N+1} = \\ &P_j(l_{1,2}, l_{2,3}, ..., l_{N,N+1}, l_{N+1,1}, \theta_1, \theta_2, ..., \theta_N, \theta_{N+1}) W_{ji}^{N+1,N} \end{aligned} \tag{4.4}$$

Here $P_i(l_{1,2}, l_{2,3}, ..., l_{N,1}, \theta_1, \theta_2, ..., \theta_N)$ represents the probability associated with generating an assembly with N particles at state i. Similarly, $P_j(l_{1,2}, ..., l_{N,N+1}, l_{N+1,1}, \theta_1, ..., \theta_N, \theta_{N+1})$ represents the probability associated with generating an assembly with $N+1$ particles at state j. With some rearrangement, and using the Monte-Carlo dynamics described above, we can rewrite Eq. 4.4 as:

$$\frac{1}{A}\mathrm{Exp}[\beta(-(\mathrm{E_j}-\mathrm{E_i})+\mu_{\mathrm{eq}})] = \frac{\mathrm{P_j}(\mathrm{l_{1,2}}, \mathrm{l_{2,3}}, ..., \mathrm{l_{N,N+1}}, \mathrm{l_{N+1,1}}, \theta_1, \theta_2, ..., \theta_{\mathrm{N}}, \theta_{\mathrm{N+1}})}{\mathrm{P_i}(\mathrm{l_{1,2}}, \mathrm{l_{2,3}}, ..., \mathrm{l_{N,1}}, \theta_1, \theta_2, ..., \theta_{\mathrm{N}})} \qquad (4.5)$$

Here we have introduced the notation μ_{eq} to denote the value of the chemical potential parameter corresponding to equilibrium dynamics, and have used $\frac{N+1}{N} \approx 1$ in the limit of large N. Using $P_i(l_{1,2}...l_{N,1}, \theta_1...\theta_N) = \exp(-\beta E_i + \beta G_N)$ and $P_j(l_{1,2}...l_{N+1,1}, \theta_1...\theta_{N+1}) = \exp(-\beta E_j + \beta G_{N+1})$ in Eq 4.5, we have $\mu_{\mathrm{eq}} = G_{N+1} - G_N + \beta^{-1}\mathrm{lnA}$. We also assume that $\lim_{N\to\infty} G_{N+1} - G_N \approx g$ making μ_{eq} independent of assembly size in the large N limit. Eq. 4.4 also implies that at equilibrium there is no particle current in average. With this, we can numerically determine μ_{eq} as the value of μ for which the size of the system does not change in our simulation. For the values of $k_s = 4$ and $k_\theta = 6$, the $\beta\mu_{\mathrm{eq}}$ was approximately 2.23.

The rate of growth of the elastic assembly can be tuned by varying the parameter μ. For values of μ above the coexistence value μ_{eq}, the system is driven away from equilibrium, and the elastic ring polymer starts to grow. When $\delta\mu/k_{\mathrm{B}}T \equiv (\mu - \mu_{\mathrm{eq}})/k_{\mathrm{B}}T$ is small, the elastic assembly grows slowly and roughly retains its circular shape. With increasing $\delta\mu/k_{\mathrm{B}}T$, the elastic assembly grows faster; its shape becomes more distorted. Ultimately, the elastic assembly buckles resulting in spikes growing out of the circle as shown in Fig. 4.1.

4.2.3 Measurement of The Surface Tension and Bending Rigidity

To study the above-mentioned morphological changes (Fig. 4.1), we examine how the fluctuations of the elastic ring polymer are modified as a function of its growth rate. Specifically, we divide the circumference of the assembly into N equal segments with length $\langle l \rangle \equiv L/N$, where N is the number of particles in the assembly at that instance of time, and L is the circumference of the assembly. We then measure fluctuations in $\hat{h}(x_n)$ where $x_n \equiv n\langle l \rangle$, $\hat{h}(x_n)$ denotes the deviation of the n^{th} segment from the average radius of the elastic assembly, $\hat{h}(x_n) \equiv h(x_n) - \langle h \rangle$. The ensemble over which the fluctuations are measured was constructed by initiating simulations with a certain initial elastic assembly nucleus with size N_0 and allowing the nucleus to grow for a time t_{measure}. In ensembles constructed in this manner, we measured $\langle |\delta h(q)|^2 \rangle$ where $\delta h(q)$ is the Fourier transform of the radial fluctuations defined with the convention: $\hat{h}(x_n) = \frac{1}{\sqrt{N}} \sum_q \delta h(q) \exp(iqx_n), q = \frac{2\pi m}{N\langle l \rangle}, m = 1, 2, ..., N$.

At or close to equilibrium, $\delta\mu/k_{\text{B}}T \ll 1$, by measuring fluctuations and averaging over the above-described ensembles, we find that $\langle |\delta h(q)|^2 \rangle$ follows an exponential distribution as shown in Fig. 4.3. Its magnitude scales likes q^{-2} in the low q regime (red line in Fig. 4.5) and scales like q^{-4} in the high q regime (blue line in Fig. 4.5). This suggests that at equilibrium, the fluctuations of the elastic ring can be effectively described using the Helfrich Hamiltonian [68]:

$$E^{\text{eq}} = \int \left\{ \frac{\gamma_{\text{eq}}}{2} (\nabla \hat{h})^2 + \frac{\kappa_{\text{eq}}}{2} (\Delta \hat{h})^2 \right\} dx. \tag{4.6}$$

Motivated by the scaling of the model, $\frac{1}{\gamma_{\text{eq}} q^2 + \kappa_{\text{eq}} q^4}$(Fig. 4.5), we refer to the parameter γ_{eq} as an effective surface tension and the parameter κ_{eq} as an effective bending rigidity.

Even as the assembly starts to grow, Fig. 4.4 and Fig. 4.6 show that the radial fluctuations are still described by an effective Helfrich Hamiltonian with renormalized surface tension and bending rigidity, γ and κ respectively. Indeed, Fig. 4.6 shows that the average $\langle |\delta h(q)|^2 \rangle$ is

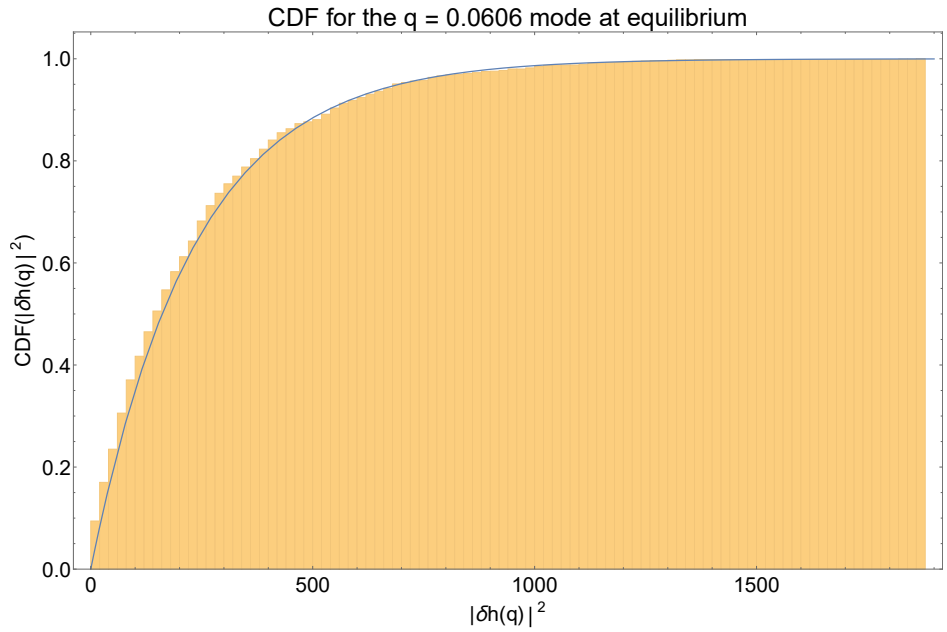

Figure 4.3: The shaded region is the CDF of $|\delta h(q)|^2$ at q = 0.0606 obtained from simulations at equilibrium. The line is the CDF of the exponential distribution: $1 - \exp \frac{|\delta h(q)|^2}{\langle |\delta h(q)|^2 \rangle_{\text{sim}}}$ here $\langle |\delta h(q)|^2 \rangle_{\text{sim}}$ is obtained from simulations.

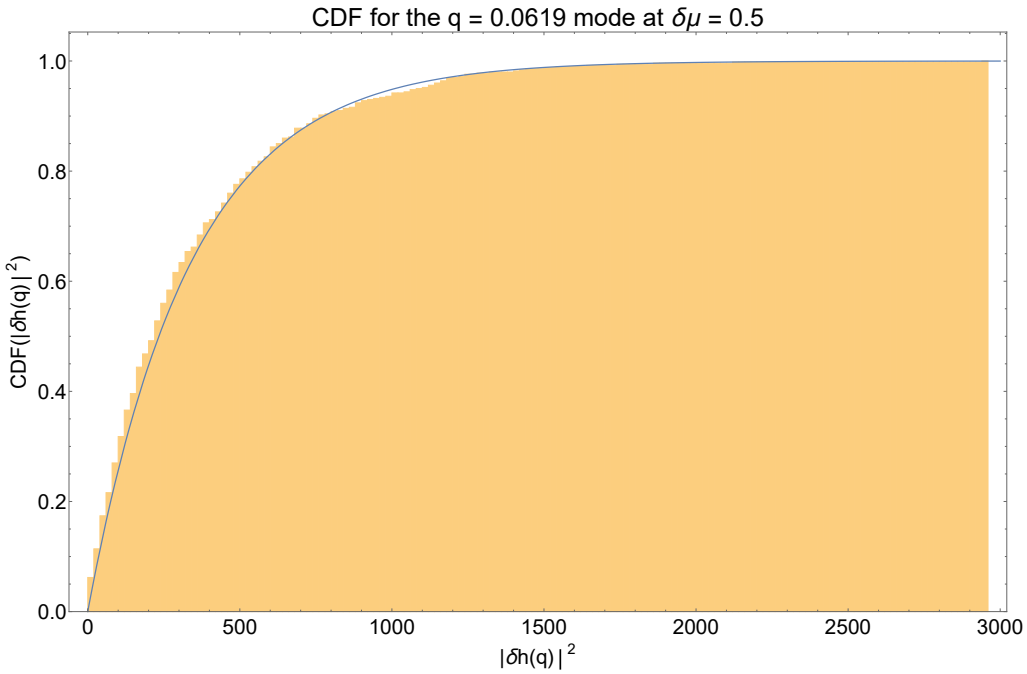

Figure 4.4: The shaded region is the CDF of $|\delta h(q)|^2$ at q = 0.0619 obtained from simulations at $\delta\mu = 0.5$ The line is the CDF of the exponential distribution: $1 - \exp \frac{|\delta h(q)|^2}{\langle |\delta h(q)|^2 \rangle_{\text{sim}}}$ here $\langle |\delta h(q)|^2 \rangle_{\text{sim}}$ is obtained from simulations.

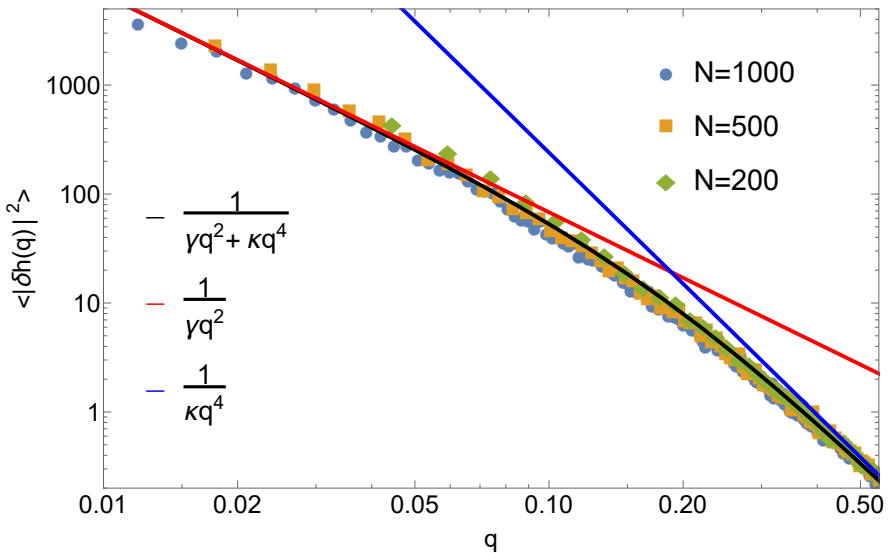

Figure 4.5: Power spectrum of interfacial fluctuations at equilibrium. For small wavevectors, q, $|\delta h(q)|^2 \propto q^{-2}$ while $|\delta h(q)|^2 \propto q^{-4}$ at high q in agreement with expectations Eq. 4.7. The data here is for $k_s = 4$ and $k_\theta = 6$. The diamond symbols are fluctuations of the assembly with 200 particles. The square symbols are fluctuations of the assembly with 500 particles. The circle symbols are fluctuation of the assembly with 1000 particles. Because the fluctuations here follow the Helfrich Hamiltonian, its standard deviation is exactly equal to its average magnitude due to the exponential nature of the distribution. Here $\gamma = 1.76$ and $\kappa = 39.1$ from the fit

well described by

$$\langle |\delta h(q)|^2 \rangle \propto \frac{k_B T}{(\gamma q^2 + \kappa q^4)}\,, \tag{4.7}$$

in accordance with Eq. 4.6 with renormalized effective surface tension and bending rigidity values. Closer inspection of the effective surface tension and bending rigidity extracted from Fig. 4.6 shows that the effective surface tension,γ decreases as $\delta\mu$ is increased, dropping to $\gamma \approx 0$ at a critical value of $\delta\mu = \delta\mu_c$ (Fig. 4.9). Beyond this point, the elastic assembly buckles and undergoes a morphological transformation to ring populated by spikes. The number of spikes appearing in a process increases with $\delta\mu$ and is proportional to the initial size of the assembly (see Fig. 4.9) and remains constant during the growing period. Reflecting the diminished effective surface tension cost under non-equilibrium conditions, the configurations with spikes allow the system to grow with minimal penalties for stretching.

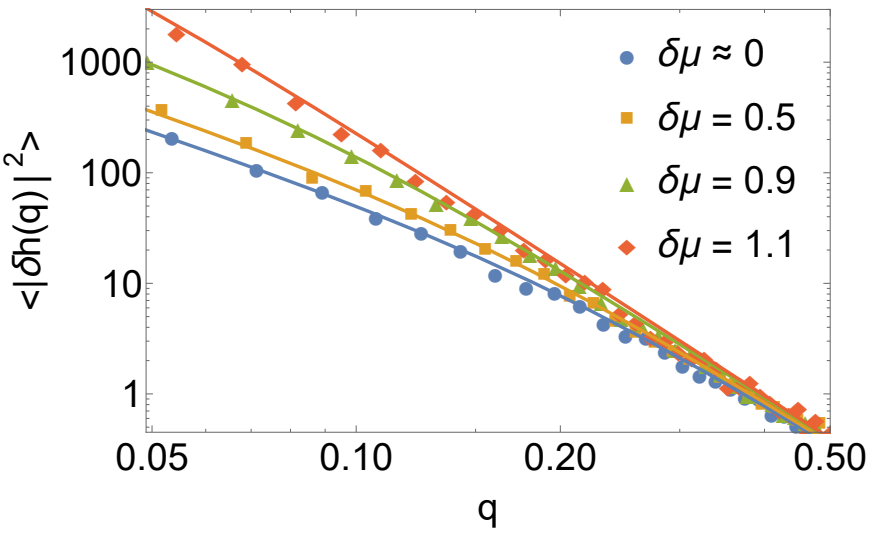

Figure 4.6: Power spectrum of interfacial fluctuations at different $\delta\mu$. Fitting these curves to Eq. 4.7 allows us to estimate γ and κ as described in the text. This analysis reveals that γ_{eff} decreases with increasing $\delta\mu$. The data here is for $k_s = 4$ and $k_\theta = 6$.

The bending rigidity does not seem to change by a large amount as indicated by fits obtained from Fig. 4.6.

In order to study how these elastic quantities depend on membrane size, we extracted the effective renormalized values of the surface tension and bending rigidity for multiple values of initial size N_0 and simulation time t_{measure}. We find that to a good numerical approximation, the effective elastic constants, γ, κ and values of the parameters μ_{coex}, and $\delta\mu_c$, are time and size-independent in all our simulations as shown in Fig. 4.7 and 4.8.

Before moving on to develop a theory of membrane effective surface tension, we would like to mention the method we used to calculate the surface tension and bending rigidity. Since the distribution of $|\delta h(q)|^2$ is exponential, its standard deviation is the same as its average. This is a property of the exponential distribution. And since the average value of $|\delta h(q)|^2$ is proportional to $\frac{1}{(\gamma q^2+\kappa q^4)}$, the smaller q, the bigger the average and its standard deviation will be. When fitting the power spectrum data to obtain estimates of γ and κ, we accounted for the varying standard deviation by appropriately reweighting the errors in a q mode by its inverse magnitude. With this, the fit will not overvalue the contribution of the

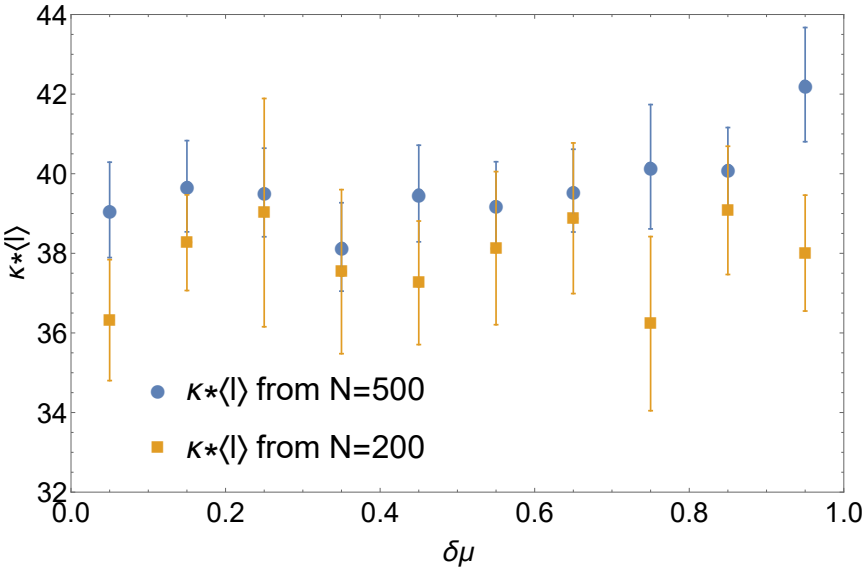

Figure 4.7: $\kappa\langle l\rangle$ vs. $\delta\mu$. This graph shows how the bending rigidity , κ, changes with $\delta\mu$ from two different assembly's sizes. Unlike the surface tension which decreases with increasing $\delta\mu$, the bending rigidity does not change much from its equilibrium value. The data here is for $k_s = 4$ and $k_\theta = 6$. The error bar represents the 95% confidence interval from fitting.

errors from the small q modes.

4.3 A non-equilibrium thermodynamic theory for renormalization of surface tension and morphological changes

Compare to the systems in the previous chapter, the membrane system here has some fundamental differences. First, the membrane does not have a bulk like a lattice system. Second, the fluctuation considered here is structural and not compositional. Thus, it is not clear if the framework developed for lattice systems can be applied here. We now show how these issues can be overcome in order to adapt our framework to the membrane growth process. Towards this goal, we will focus on, and represent using a Markov process, the dynamics of a segment of the ring-like assembly depicted in Fig. 4.10 as the membrane assimilates and gives up particles. The ring-like segment is assumed to be composed of M beads with periodic conditions at the ends. A state ω of this segment can transition to a state ω' after an

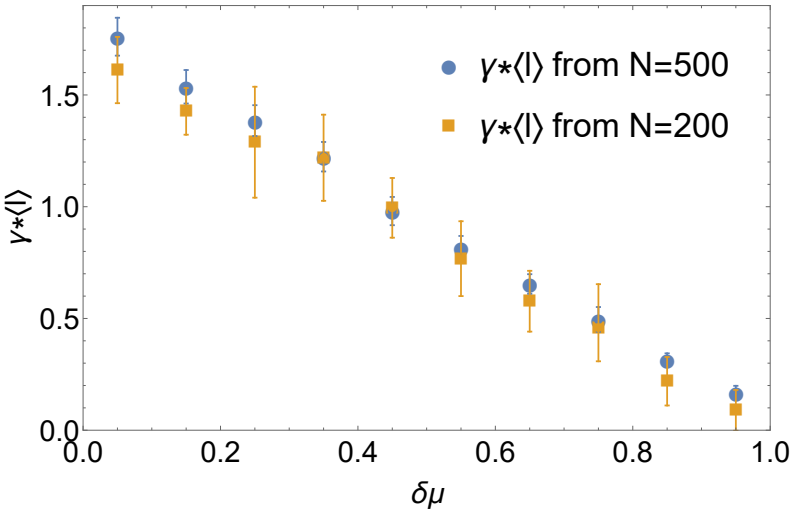

Figure 4.8: $\gamma\langle l\rangle$ vs. $\delta\mu$. This graph shows how the surface tension , γ, changes with $\delta\mu$ from two different assembly's sizes. The data here is for $k_s = 4$ and $k_\theta = 6$. The error bar represents the 95% confidence interval from fitting.

addition event through a pathway of the sort depicted in Fig. 4.10. Specifically, a particular particle addition event is allowed to take place with a rate $k_{\text{add}}(\omega, \tilde{\omega})$ where $\tilde{\omega}$ denotes an intermediate state with $M + 1$ beads. Since we are only interested in focusing on segments with M beads, we then construct ω' from $\tilde{\omega}$ by simply resolving the first M beads in the clockwise direction without loss of generality.

A transition from ω' to ω due to a particle removal event proceeds according to the schematic in Fig 4.10. Here, we first imagine extending the segment ω' to construct a $M + 1$ bead segment, $\tilde{\omega}$ by including the bead from the full membrane that is adjacent to the clockwise end of ω'. The probability associated with generating this intermediate configuration can be represented as $P(\tilde{\omega}|\omega')$ and depends on the correlations and steady-state generated as the membrane is grown at a given value of $\delta\mu$. Next, a particle removal event is allowed to take place with a rate $k_{\text{remove}}(\tilde{\omega}, \omega)$.

As an aside, we note that this set of dynamics of the M bead segment requires an input: the conditional probability $P(\tilde{\omega}|\omega')$. Alternately, one can imagine evolving the above described dynamics for a test conditional probability distribution $P_{\text{test}}(\tilde{\omega}|\omega')$. For sufficiently

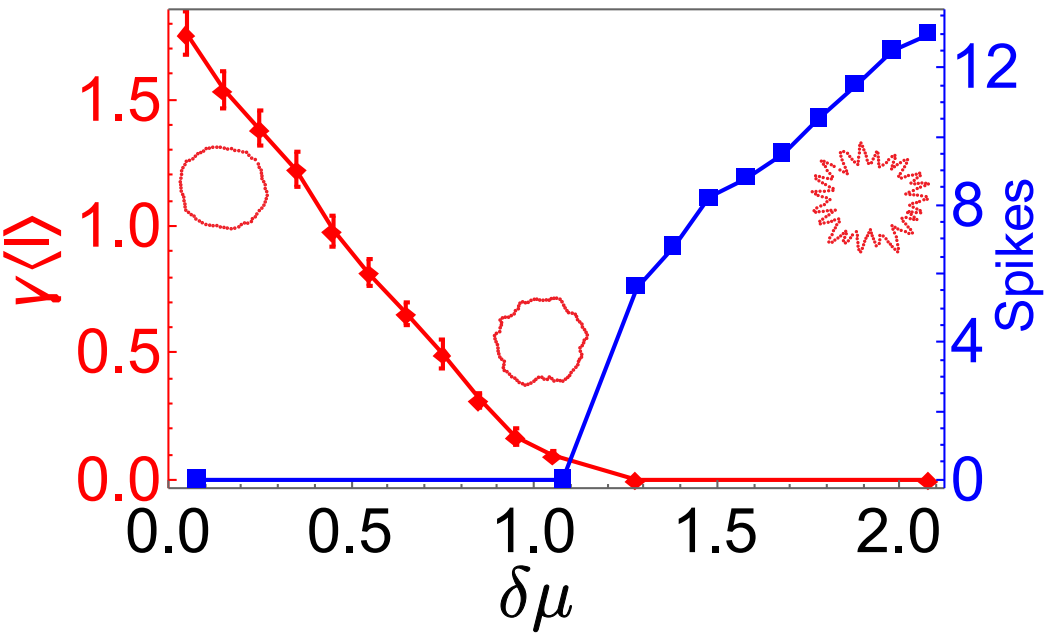

Figure 4.9: Phase diagram for data at $k_s = 4$ and $k_\theta = 6$. As $\delta\mu$ is increased, the effective surface tension γ decreases eventually reaching $\gamma \approx 0$ for $\delta\mu \approx 1.1$. Increasing $\delta\mu$ beyond this value induces a morphological change to a configuration with spikes. The data was obtained with $N_0 = 200$. The red curve in the figure represents the surface tension γ of the assembly before the instability. The error bar represents the 95% confidence interval from fitting. After the instability, γ is negative and cannot be measure using the Fourier transform technique. We then use the number of spikes (the blue curve) in the assembly, which can be used to infer the instabilities' wavelength, to indicate the systems at different drive post the instability.

large values of M, the steady-state generated under the above described dynamics can be used to self consistently generate the conditional probability $P_{\rm ss}(\tilde{\omega}|\omega')$ where the subscript ss is meant to denote that the conditional probability has been generated by analyzing the steady state of the M bead segment. For instance, let's imagine on a subsection consisting of M beads segment of size L. For dynamics generated with the correct input conditional probability, $P(\tilde{\omega}|\omega')$, when $L, M \gg 1$ and the size of the M bead segment is far greater than any correlation length in the system, the conditional probability computed from the M bead subsections, $P_{\rm ss}(\tilde{\omega}|\omega')$, should closely resemble $P(\tilde{\omega}|\omega')$. Now, coming back to the dynamics generated with a test conditional probability, $P_{\rm test}(\tilde{\omega}|\omega')$, the self consistency condition $P_{\rm test}(\tilde{\omega}|\omega') = P_{\rm ss}(\tilde{\omega}|\omega')$ can be used to progressively refine the input estimate.

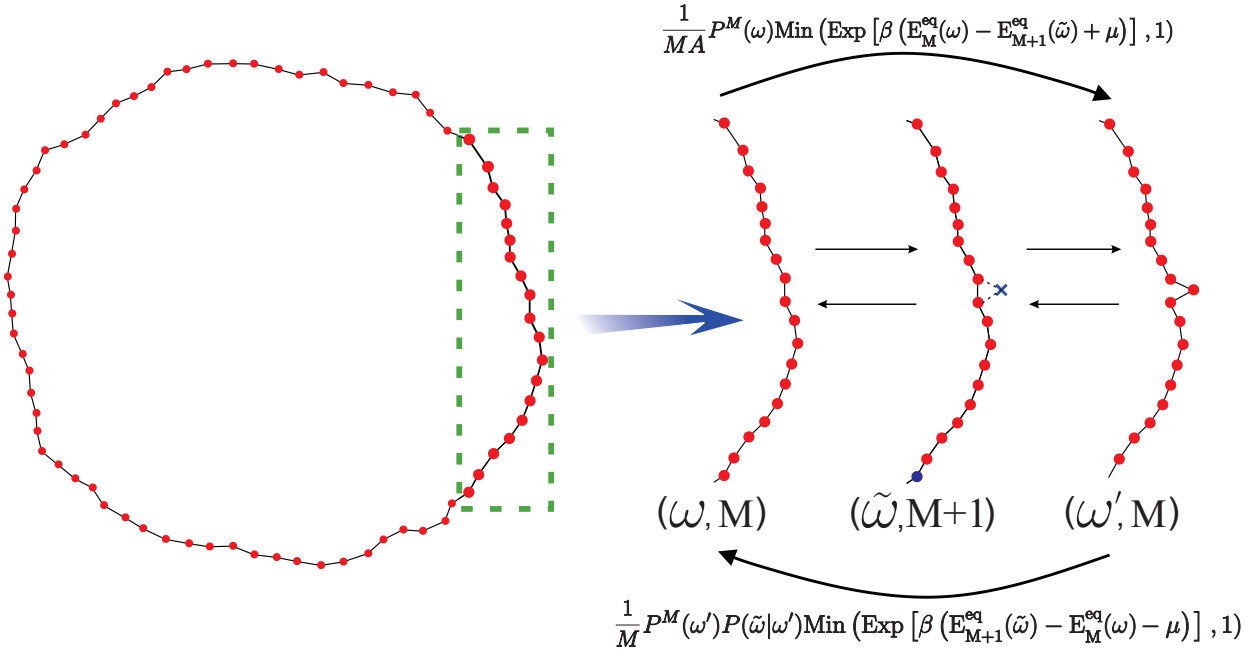

Figure 4.10: Schematic of the addition/removal and rescaled moves of our Markov system. In our Markov network, to reach ω' from ω, the system has to go through an intermediate state $\tilde{\omega}$. From ω to $\tilde{\omega}$, a new particle is added to the assembly. From $\tilde{\omega}$ to ω', a particle at the bottom is removed to preserve the same number of particles. We have colored the to be added or removed particle blue to distinguish it from the other particles in the assembly.

In this manner, the dynamics of the M bead segment can potentially be used to obtain estimates of the correlations and steady states generated in the original non-equilibrium growth process.

Following the set up above, the addition rate and removal rate of a bead in our segment are

$$W_{\text{add}}(\omega, \tilde{\omega}, \omega') = \frac{1}{MA} k_{\text{add}}(\omega, \tilde{\omega}) \tag{4.8}$$

$$W_{\text{rem}}(\omega, \tilde{\omega}, \omega') = \frac{1}{M} P(\tilde{\omega}|\omega') k_{\text{remove}}(\tilde{\omega}, \omega) \tag{4.9}$$

In addition, we note that the ratio of add and removal transition rates are informed by the microscopic dynamics and satisfy

$$\frac{k_{\text{add}}(\omega, \tilde{\omega})}{k_{\text{remove}}(\tilde{\omega}, \omega)} = e^{\beta\left(\left[E_M^{\text{eq}}(\omega) - E_{M+1}^{\text{eq}}(\tilde{\omega})\right] + \mu\right)} \tag{4.10}$$

where $\beta^{-1} \equiv k_B T$ sets the thermal energy scale, $E_M^{\text{eq}}(\omega)$ is the intrachain potential energy of the M bead segment and $E_{M+1}^{\text{eq}}(\tilde{\omega})$ is the intrachain potential energy of the $M+1$ bead segment. The condition in Eq. 4.10 is consistent with the microscopic dynamics used in this paper. Because the intermediate state $\tilde{\omega}$ can be inferred from the initial state ω and final state ω', we will shorten our notations into: $W_{\text{add}}(\omega, \tilde{\omega}, \omega') = W_{\text{add}}(\omega, \omega')$ and $W_{\text{rem}}(\omega, \tilde{\omega}, \omega') = W_{\text{rem}}(\omega, \omega')$

Now, let's consider the probability $P^M(\omega_{n-1}, \omega_n)$ that is the probability of a transformation of a segment of M beads with configuration ω_{n-1} to configuration ω_n through an addition of a bead. The n subscript here is simply used as index for convenient of distinguishing between addition and removal move in the equation. We can then write down the

master equation for this probability.

$$\begin{aligned}
&\frac{dP^M(\omega_n,\omega_{n+1})}{dt} = \sum_{\omega_{n-1}} P^M(\omega_{n-1},\omega_n)W_{\text{add}}(\omega_n,\omega_{n+1}) \\
&+ \sum_{\omega_{n+2}} P^M(\omega_{n+2})W_{\text{rem}}(\omega_{n+1},\omega_{n+2})P^M(\omega_n|\omega_{n+1}) \\
&- \sum_{\omega_{n-1}} P^M(\omega_{n+1})W_{\text{rem}}(\omega_n,\omega_{n+1})P^M(\omega_{n-1}|\omega_n) \\
&- \sum_{\omega_{n+2}} P^M(\omega_{n+1})W_{\text{add}}(\omega_{n+1},\omega_{n+2})P^M(\omega_n|\omega_{n+1}) \\
=&P^M(\omega_n)W_{\text{add}}(\omega_n,\omega_{n+1}) + P^M(\omega_n|\omega_{n+1})\sum_{\omega_{n+2}} P^M(\omega_{n+2})W_{\text{rem}}(\omega_{n+1},\omega_{n+2}) \\
&- P^M(\omega_{n+1})W_{\text{rem}}(\omega_n,\omega_{n+1}) - P^M(\omega_n|\omega_{n+1})\sum_{\omega_{n+2}} P^M(\omega_{n+1})W_{\text{add}}(\omega_{n+1},\omega_{n+2})
\end{aligned} \tag{4.11}$$

Now we consider the system at steady state:

$$\begin{aligned}
&P^M_{\text{ss}}(\omega_n)W_{\text{add}}(\omega_n,\omega_{n+1})) - P^M_{\text{ss}}(\omega_{n+1})W_{\text{rem}}(\omega_n,\omega_{n+1}) = \\
&P^M_{\text{ss}}(\omega_n|\omega_{n+1})\big(\sum_{\omega_{n+2}} P^M_{\text{ss}}(\omega_{n+1})W_{\text{add}}(\omega_{n+1},\omega_{n+2}) - P^M_{\text{ss}}(\omega_{n+2})W_{\text{rem}}(\omega_{n+1},\omega_{n+2})\big)
\end{aligned} \tag{4.12}$$

$$J_{\Delta N}(\omega_n,\omega_{n+1}) = P^M_{\text{ss}}(\omega_n|\omega_{n+1})\sum_{\omega_{n+2}} J_{\Delta N}(\omega_{n+1},\omega_{n+2}) \tag{4.13}$$

Here we have write:

$$J_{\Delta N}(\omega_n,\omega_{n+1}) = P^M_{\text{ss}}(\omega_n)W_{\text{add}}(\omega_n,\omega_{n+1}) - P^M_{\text{ss}}(\omega_{n+1})W_{\text{rem}}(\omega_n,\omega_{n+1}) \tag{4.14}$$

We have add the ss subscript to indicate steady state. Next, we write $V_{\Delta N}(\omega_{n+1}) = \sum_{\omega_{n+2}} J_{\Delta N}(\omega_{n+1},\omega_{n+2})$. $V_{\Delta N}(\omega_{n+1})$ is the growth rate of the configuration ω_{n+1} in the

segment, and its sum, $\sum_{\omega_{n+1}} V^s(\omega_{n+1}) = \langle \dot{N} \rangle$, is the growth rate of the assembly. We then sum over all ω_{n+1} configuration in Eq. 4.13.

$$\sum_{\omega_{n+1}} J_{\Delta N}(\omega_n, \omega_{n+1}) = \sum_{\omega_{n+1}} P_{\rm ss}^M(\omega_n|\omega_{n+1}) V_{\Delta N}(\omega_{n+1}) \tag{4.15}$$

$$V_{\Delta N}(\omega_n) = \sum_{\omega_{n+1}} P_{\rm ss}^M(\omega_n|\omega_{n+1}) V_{\Delta N}(\omega_{n+1}) \tag{4.16}$$

If we consider $P_{\rm ss}^M(\omega_n|\omega_{n+1})$ as an element of the matrix $\mathbf{P_{ss}^M}$ and $V_{\Delta N}(\omega_n)$ an element of the vector $\mathbf{V_{\Delta N}}$, the above equation indicate that $\mathbf{V_{\Delta N}}$ is the eigenvector of matrix $\mathbf{P_{ss}^M}$ with eigenvalue 1. In addition, we also have

$$P_{\rm ss}^M(\omega_n) = \sum_{\omega_{n+1}} P_{\rm ss}^M(\omega_n, \omega_{n+1}) = \sum_{\omega_{n+1}} P_{\rm ss}^M(\omega_n|\omega_{n+1}) P_{\rm ss}^M(\omega_{n+1}) \tag{4.17}$$

Eq. 4.16 and Eq. 4.17 suggests that $V_{\Delta N}(\omega_n) \propto P_{ss}^M(\omega_n)$. Using the normalization of the probability, we then have:

$$P_{\rm ss}^M(\omega_n) = \frac{V_{\Delta N}(\omega_n)}{\sum_{\omega_n} V_{\Delta N}(\omega_n)} = \frac{\sum_{\omega_{n+1}} J_{\Delta N}(\omega_n, \omega_{n+1})}{\langle \dot{N} \rangle} \tag{4.18}$$

4.4 Entropy Production For The Membrane Growth

Given the description of the above dynamics, an expression for entropy production rate for a particle addition event resulting in a transition from a state ω to a state ω' through an intermediate state $\tilde{\omega}$ is simply given by

$$\begin{aligned} k_B^{-1} \dot{S}(\omega, \tilde{\omega}, \omega') = & J_{\Delta N}(\omega, \tilde{\omega}, \omega') \\ & \ln \frac{P_{\rm ss}^M(\omega) k_{\rm add}(\omega, \tilde{\omega})}{P_{\rm ss}^M(\omega') P_{\rm ss}(\tilde{\omega}|\omega') k_{\rm remove}(\tilde{\omega}, \omega) A} \end{aligned} \tag{4.19}$$

where

$$J_{\Delta N}(\omega, \tilde{\omega}, \omega') \equiv \\ \frac{1}{M}\left[\frac{1}{A} P_{\rm ss}^{M}(\omega) k_{\rm add}(\omega, \tilde{\omega}) - P_{\rm ss}^{M}(\omega') P_{\rm ss}(\tilde{\omega}|\omega') k_{\rm remove}(\tilde{\omega}, \omega)\right] \tag{4.20}$$

Note also that the conditional probability can be expressed as $P_{\rm ss}(\tilde{\omega}|\omega') = P_{\rm ss}(\tilde{\omega}, \omega')/P_{\rm ss}^{M}(\omega')$ where $P_{\rm ss}(\tilde{\omega}, \omega')$ is simply the joint probability associated with sampling $\tilde{\omega}$ and ω'. Since the M bead segment ω' is a subset of the $M+1$ bead segment $\tilde{\omega}$, the joint probability $P_{\rm ss}(\tilde{\omega}, \omega')$ can be compactly expressed using the symbol $P_{\rm ss}^{M+1}(\tilde{\omega})$, the steady state probability distribution associated with sampling the $M+1$ length segment, $\tilde{\omega}$.

We also define $P_{\rm eq}^{M}(\omega) = \exp(-\beta E_{M}^{\rm eq}(\omega))/Z_{M}^{\rm eq}$ where $Z_{M}^{\rm eq} = \sum_{\omega} \exp -\beta E_{M}^{\rm eq}(\omega)$ and $P_{\rm eq}^{M+1}(\tilde{\omega}) = \exp(-\beta E_{M+1}^{\rm eq}(\tilde{\omega}))/Z_{M+1}^{\rm eq}$ where $Z_{M+1}^{\rm eq} = \sum_{\tilde{\omega}} \exp -\beta E_{M+1}^{\rm eq}(\tilde{\omega})$. Formally, $P_{\rm eq}^{M}(\omega)$ and $P_{\rm eq}^{M+1}(\tilde{\omega})$ denote the equilibrium Boltzmann probability distributions associated with the M and $M+1$ segments, ω and $\tilde{\omega}$ respectively.

Using these definitions and symbols, and using Eq. 4.10, we can write Eq. 4.19 as

$$k_B^{-1} \dot{S}(\omega, \tilde{\omega}, \omega') = J_{\Delta N}(\omega, \tilde{\omega}, \omega') \left[\ln \frac{P_{\rm ss}^{M}(\omega)}{P_{\rm eq}^{M}(\omega)} - \ln \frac{P_{\rm ss}^{M+1}(\tilde{\omega})}{P_{\rm eq}^{M+1}(\tilde{\omega})}\right] \\ + J_{\Delta N}(\omega, \tilde{\omega}, \omega') \beta \delta\mu \tag{4.21}$$

where $\delta\mu \equiv \mu - (G_{M+1}^{\rm eq} - G_{M}^{\rm eq}) - \beta^{-1}{\rm lnA}$ where $G_{M+1}^{\rm eq} = -\beta^{-1} \ln Z_{M+1}^{\rm eq}$ and $G_{M}^{\rm eq} = -\beta^{-1} \ln Z_{M}^{\rm eq}$, is the excess chemical potential driving the non-equilibrium growth process. To get an expression for the overall entropy production rate, we now sum over all possible transitions. Since every allowed transition between a pair of states ω and ω' has a unique $M+1$ bead intermediate state, $\tilde{\omega}$, the sum over allowed transitions is formally equivalent to summing over all possible pairs of M and $M+1$ bead states, ω and $\tilde{\omega}$.

Performing this summation, an expression for the total entropy production can be written

as

$$k_B^{-1}\dot{S} = \beta\langle\dot{N}\rangle\delta\mu + \sum_{\omega} \ln\frac{P_{\rm ss}^{M}(\omega)}{P_{\rm eq}^{M}(\omega)} \sum_{\tilde{\omega}} J_{\Delta N}(\omega,\tilde{\omega}) - \sum_{\tilde{\omega}} \ln\frac{P_{\rm ss}^{M+1}(\tilde{\omega})}{P_{\rm eq}^{M+1}(\tilde{\omega})} \sum_{\omega} J_{\Delta N}(\omega,\tilde{\omega}) \quad (4.22)$$

where we have dropped the dependence of J on ω' for ease of notation and we have used the fact that the sum of all currents J is simply the net average rate of growth, $\langle\dot{N}\rangle$. To proceed further, we use Eq. 4.18 to arrive at: $\sum_{\tilde{\omega}} J_{\Delta N}(\omega,\tilde{\omega}) = \langle\dot{N}\rangle P^{M}(\omega)$. Similarly, with Eq. 4.18 and the condition of probability flux conservation we have: $\sum_{\omega} J_{\Delta N}(\omega,\tilde{\omega}) = \langle\dot{N}\rangle P^{M+1}(\tilde{\omega})$. With these equations, the expression for entropy production reads

$$k_B^{-1}\dot{S} = \langle\dot{N}\rangle[\beta\delta\mu - (D[P_{\rm ss}^{M+1}(\tilde{\omega})||P_{\rm eq}^{M+1}(\tilde{\omega})] - D[P_{\rm ss}^{M}(\omega)||P_{\rm eq}^{M}(\omega)])] \quad (4.23)$$

where $D[p||q]$ denotes the relative entropy between distributions p and q. Finally, noting the fact that $D[P_{\rm ss}^{M+1}(\tilde{\omega})||P_{\rm eq}^{M+1}(\tilde{\omega})]$ and $D[P_{\rm ss}^{M}(\omega)||P_{\rm eq}^{M}(\omega)]$ are relative entropies between non-equilibrium and equilibrium distributions of segments of length $M+1$ and M respectively, and using

$$D[P_{\rm ss}^{M+1}(\tilde{\omega})||P_{\rm eq}^{M+1}(\tilde{\omega})] - D[P_{\rm ss}^{M}(\omega)||P_{\rm eq}^{M}(\omega)] \approx \frac{D[P_{\rm ss}^{M}(\omega)||P_{\rm eq}^{M}(\omega)]}{M} \quad (4.24)$$

in the limit $M \gg 1$ we can write Eq. 4.23 as

$$k_B^{-1}\dot{S} = \langle\dot{N}\rangle\left[\beta\delta\mu - \frac{D[P_{\rm ss}^{M}(\omega)||P_{\rm eq}^{M}(\omega)]}{M}\right] \quad (4.25)$$

and since $\langle\dot{N}\rangle \geq 0$ for all our cases, the second law of thermodynamics requires that:

$$\delta\mu - \frac{D[P_{\rm ss}^{M}(\omega)||P_{\rm eq}^{M}(\omega)]}{\beta M} \geq 0 \quad (4.26)$$

Finally, by defining a new energy $E_M^{\rm eff}(\omega)$ with: $P_{\rm ss}^{M}(\omega) \equiv \exp\left(-\beta E_M^{\rm eff}(\omega)\right)/Z_M^{\rm eff}$ and $G_M^{\rm eff} =$

$-\beta^{-1}\ln Z_M^{\text{eff}} = -\beta^{-1}\ln\sum_\omega \exp\left(-\beta E_M^{\text{eff}}(\omega)\right)$ we can rewrite the Eq. 4.26 as:

$$\delta\mu - \frac{\langle E_M^{\text{eq}} - E_M^{\text{eff}}\rangle + G_M^{\text{eff}} - G_M^{\text{eq}}}{M} \geq 0 \tag{4.27}$$

By focusing on a ring segment with finite M beads instead of the whole assembly, we can write down a finite periodic Markov network for the segment. This then allows us to import the proof of the thermodynamics uncertainty relations, which has been previously proven for arbitrary periodic Markov network [20, 21]. The thermodynamics uncertainty relation states that:

$$k_B^{-1}\dot{S} \geq \frac{J_\alpha^2}{D_\alpha} \tag{4.28}$$

Here J_α is any current of the Markov network and D_α is its diffusion constant. If we use the particle current $J_\alpha = \langle\dot{N}\rangle$ and plug in Eq. 4.25 then we have:

$$\delta\mu - \frac{\langle E_M^{\text{eq}} - E_M^{\text{eff}}\rangle + G_M^{\text{eff}} - G_M^{\text{eq}}}{M} \geq \frac{\langle\dot{N}\rangle}{\beta D_N} \tag{4.29}$$

4.5 Entropy Production As A Function Of Surface Tension

Here we will detail how to expression the entropy production as a function of surface tension. From simulations (see Fig. 4.7), the normalization of the bending rigidity, κ, is minimal. Thus, we will further assume that $\kappa = \kappa_{\text{eq}}$ to make the calculation simpler. With this approximation, we have $\langle E^{\text{eq}}\rangle = \langle l\rangle\sum_q \left(\frac{1}{2}\gamma_{\text{eq}}q^2 + \frac{1}{2}\kappa_{\text{eq}}q^4\right)|\delta h(q)|^2$, $\langle E^{\text{eff}}\rangle = \langle l\rangle\sum_q \left(\frac{1}{2}\gamma q^2 + \frac{1}{2}\kappa_{\text{eq}}q^4\right)|\delta h(q)|^2$ and $|\delta h(q)|^2 = \frac{k_BT}{\langle l\rangle(\gamma q^2+\kappa_{\text{eq}}q^3)}$. If we convert the sum here to integral using $dq = \frac{2\pi}{L}$:

$$\langle E^{\text{eq}}\rangle = \frac{Lk_BT}{4\pi}\int_0^{2\pi/\lambda}\frac{\gamma_{\text{eq}}q^2 + \kappa_{\text{eq}}q^4}{\gamma q^2 + \kappa_{\text{eq}}q^4}dq \tag{4.30}$$

Here λ is the smallest wavelength allowed by the assembly which we will take to be

$\langle l \rangle \approx l_0$. With some algebra we will have:

$$\langle E^{\mathrm{eq}} \rangle = \frac{N k_B T}{2} \left(1 - \frac{\lambda(\gamma - \gamma_{\mathrm{eq}}) \arctan\left[\frac{2\pi\sqrt{\kappa_{\mathrm{eq}}}}{\sqrt{\gamma}\lambda}\right]}{2\pi\sqrt{\gamma\kappa_{\mathrm{eq}}}} \right) \tag{4.31}$$

We have used: $N = \frac{L}{\langle l \rangle} = \frac{L}{\lambda}$.The same procedure with E_{eff} yields:

$$\langle E^{\mathrm{eff}} \rangle = \frac{N k_B T}{2} \tag{4.32}$$

The free energy is $G^{\mathrm{eff}} = -k_B T \ln\left(\int \exp\left[-\mathrm{E}^{\mathrm{eff}}(\delta \mathrm{h})\right] \delta \mathrm{h}\right)$. Here if we plug in E^{eff} and realize that the integral of δh is a Gaussian integral, we can simplify the free energy to:

$$G^{\mathrm{eff}} = -k_B T \ln\left(\prod_{\mathrm{q}} \frac{2\pi}{\gamma \mathrm{q}^2 + \kappa_{\mathrm{eq}} \mathrm{q}^4}\right)^{(1/2)} = \frac{-\mathrm{k_B T}}{2} \sum_{\mathrm{q}} \ln\left(\frac{2\pi}{\gamma \mathrm{q}^2 + \kappa_{\mathrm{eq}} \mathrm{q}^4}\right) \tag{4.33}$$

We then use a similar procedure as in the case of E_{eq} to turn the sum into an integral. With a few line of algebras, we will obtain:

$$G^{\mathrm{eff}} = \frac{N k_B T \lambda}{2\pi} \left(\sqrt{\frac{\gamma}{\kappa_{\mathrm{eq}}}} \arctan\left[\frac{2\pi}{\lambda}\sqrt{\frac{\kappa_{\mathrm{eq}}}{\gamma}}\right] - \frac{\pi}{\lambda}\left(2 + \ln\left[\frac{2\pi\lambda^2}{4\pi^2\kappa_{\mathrm{eq}} + \gamma\lambda^2}\right]\right)\right) \tag{4.34}$$

Similarly, the expression for the G^{eq} is:

$$G^{\mathrm{eq}} = \frac{N k_B T \lambda}{2\pi} \left(\sqrt{\frac{\gamma_{\mathrm{eq}}}{\kappa_{\mathrm{eq}}}} \arctan\left[\frac{2\pi}{\lambda}\sqrt{\frac{\kappa_{\mathrm{eq}}}{\gamma_{\mathrm{eq}}}}\right] - \frac{\pi}{\lambda}\left(2 + \ln\left[\frac{2\pi\lambda^2}{4\pi^2\kappa_{\mathrm{eq}} + \gamma_{\mathrm{eq}}\lambda^2}\right]\right)\right) \tag{4.35}$$

If we plug in the definition of ϵ_{diss}:

$$\epsilon_{diss} = \frac{\langle E^{\text{eq}} - E^{\text{eff}} \rangle + G^{\text{eff}} - G^{\text{eq}}}{N}$$
$$= \frac{k_B T \lambda}{4\pi} \left(\frac{(\gamma + \gamma_{\text{eq}}) \text{arctan}[\frac{2\pi\sqrt{\kappa_{\text{eq}}}}{\lambda\sqrt{\gamma}}]}{\sqrt{\gamma \kappa_{\text{eq}}}} - \frac{(2\sqrt{\gamma_{\text{eq}}\gamma}) \text{arctan}[\frac{2\pi\sqrt{\kappa_{\text{eq}}}}{\lambda\sqrt{\gamma_{\text{eq}}}}]}{\sqrt{\gamma \kappa_{\text{eq}}}} - \frac{2\pi \left(\ln \left[\frac{4\pi^2 \kappa_{\text{eq}} + \gamma_{\text{eq}} \lambda^2}{4\pi^2 \kappa_{\text{eq}} + \gamma \lambda^2} \right] \right)}{\lambda} \right) \tag{4.36}$$

Before proceeding to use Eq. 4.29 to elucidate how the thermodynamic driving forces control the renormalization of material properties and morphologies, we first consider Eq. 4.29 without the term non-negative term ϵ_{diss} [1]. The bound in Eq. 4.29 reduces to the following relation between driving force $\delta\mu$ and ratio v/D, $\delta\mu \geq \frac{v k_B T}{D}$. In Fig. 4.11 we numerically verify that our simulations at two different sizes do indeed satisfy this simplified connection. Further, in the limit of slow driving, $\delta\mu/k_B T \ll 1$, Fig. 4.11 reveals that most of the driving force is used up in maintaining a growth rate with very little remaining for renormalization of material parameters. In this limit, $\delta\mu \approx v/D$. At larger values of the driving, $\delta\mu$ deviates significantly from v/D. Larger value of the thermodynamic cost associated with renormalized fluctuations, ϵ_{diss}, are hence allowed by our thermodynamic bound in these regimes. Indeed, our simulations (Fig. 4.1) show how a dramatic change in morphologies can be achieved for $\delta\mu/k_B T \approx 1$. We will now use Eq. 4.29 to understand how γ can be controlled by tuning $\delta\mu$. The predicted $\delta\mu$s are plotted in Fig. 4.12 alongside the scaling of γ with $\delta\mu$ extracted from simulations. In particular, the lower bound suggested by Eq. 4.29 is surprisingly close to the actual non-equilibrium driving force $\delta\mu$ required to renormalize membrane tension and induce morphological transformations ($\gamma \sim 0$). Unlike the usual approaches, the bounds here do not require extensive knowledge of the kinetics of the system. Indeed, as evidenced by the performance of the bound in Eq. 4.29 in Fig. 4.12, our results

1. The statement $\epsilon_{\text{diss}} \geq 0$ can be proven by applying Jensen's inequality to: $\langle \exp\left[-(E^{\text{eq}} - E^{\text{eff}})\right] \rangle = \exp\left[-(G^{\text{eq}} - G^{\text{eff}})\right]$

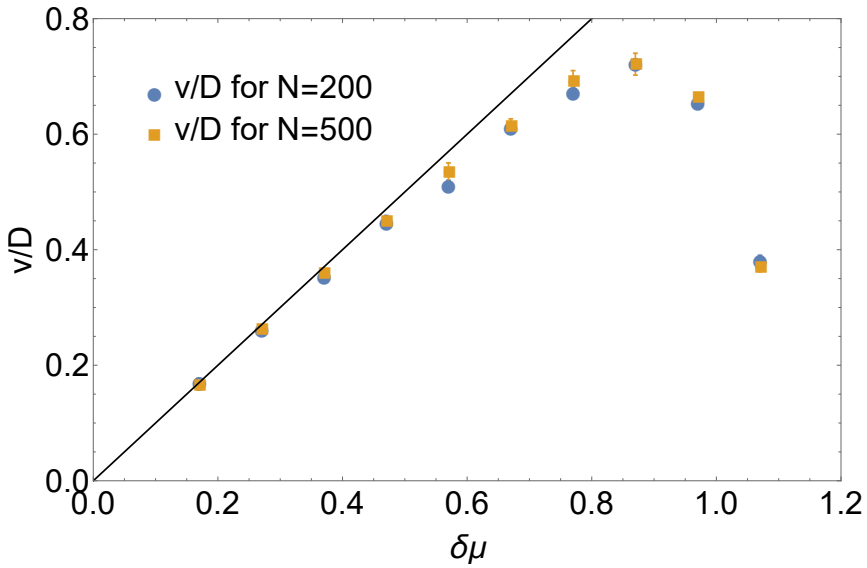

Figure 4.11: $\frac{v}{D}$ vs. $\delta\mu$. In this case, $k_{\mathrm{B}}T$ is set to 1. The dark line is predicted from linear response. The error bar represents the 95% confidence interval from the fit $\delta\mu = v/D$. The blue dot is from the assemblies of 200 particles, while the orange dot is from the assemblies of 500 particles. The two measurements overlaps with some minor error.

show how a large component of the non-equilibrium renormalization of membrane material properties is effectively controlled by two (experimentally accessible) parameters, the driving force $\delta\mu$, and the ratio v/D.

4.6 3D Model Membrane Simulation

In this section, we detail calculations that qualitatively suggest that the results obtained with the 2D model in the main text can be extended to non-equilibrium growth problems with three dimensional vesicles/membranes. Following Ref. [66], we model a three dimensional fluid vesicle using a triangulated mesh. The nodes of the mesh are meant to represent membrane particles in a coarse-grained fashion. The energy associated with a specific configuration of the vesicle is given by
$H = \sum_{\text{faces}} \left[(k_A(A - A_0)^2 + \sum_{i=1}^{3} k_\theta(\theta_i - \pi/3)^2 + \sum{}' k_\phi(\phi - \pi)^2) \right]$, where $\sum_{\text{faces}}$ is a sum over the triangulated faces, A is the area of a triangulated face, θ_i are the angles inside a

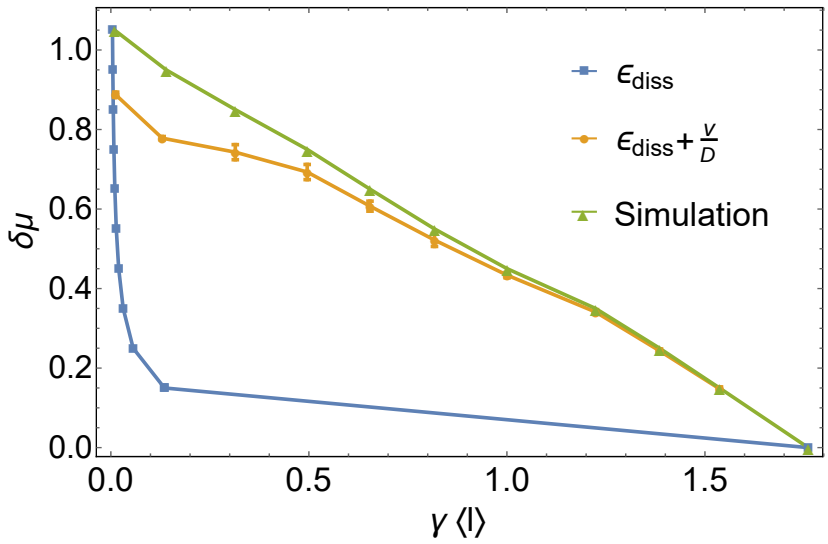

Figure 4.12: Thermodynamic bounds on the surface tension as a function of the non-equilibrium driving force $\delta\mu$. The bound stipulated by the blue curve is from Eq. 4.27. The bound stipulated by the orange curve is from Eq. 4.29. The green curve is obtained by measuring γ from simulations and is consistent with the bounds specified by Eq. 4.27 and Eq. 4.29. These bounds provide rough estimates for the energetic costs required to modify the morphology and fluctuations in the elastic membrane. The error bars in the second bound is obtained from 95% confidence intervals of fitting. $\frac{v}{D}$.

triangulated face, $\sum'$ denotes a sum over different adjacent phases and ϕ denotes the angle between two adjacent faces.

In our model, the number of bonds or connections a particular particle can make is limited from 5 to 7. Similar to the 2D model, we attempt to add and remove particle in our Monte Carlo simulation. In the addition move, a point is chosen in a triangulated surface to add the new particle. In the removal move, a particle will be fused with one of its neighbors. Like the 2D model simulation, the acceptance rate for addition is $\text{Min}(\text{Exp}[\beta(-\Delta\text{E}+\mu]), 1)$ and the removal rate is $\text{Min}(\text{Exp}[\beta(-\Delta\text{E}-\mu)], 1)$. Since the overall connectivity of the particles changes in the course of the addition and removal moves, this membrane model will exhibit fluid like behavior and will not have crumpling transitions of the sort in [70]. Fig. 4.13 shows the shape of our 3D membrane model at equilibrium. Fig. 4.14 is a heat map showing the relative radii of the models when it is at equilibrium and at the instability.

In order to apply the bounds in the main text, we decompose the fluctuations of the 3D membrane model into spherical harmonic modes [71]. Fig. 4.15 shows how our bounds apply to the 3D membrane model. We plan to further investigate these ideas in future work.

4.7 Conclusion

The role played by non-equilibrium forces in biological processes such as those responsible for modulating cell shapes, and dynamics is well established [48, 50, 51, 49, 58, 59]. In this paper, we have shown how ideas from stochastic thermodynamics, particularly an adaptation of the recently derived thermodynamic uncertainty relations, can be used to obtain general non-equilibrium thermodynamic constraints on membrane morphologies and material properties. Our thermodynamic bounds are minimal depending on the details of the kinetic processes responsible for membrane growth. We anticipate that such thermodynamic ideas will find broad applicability and reveal how material properties and morphologies can be robustly controlled even far from equilibrium.

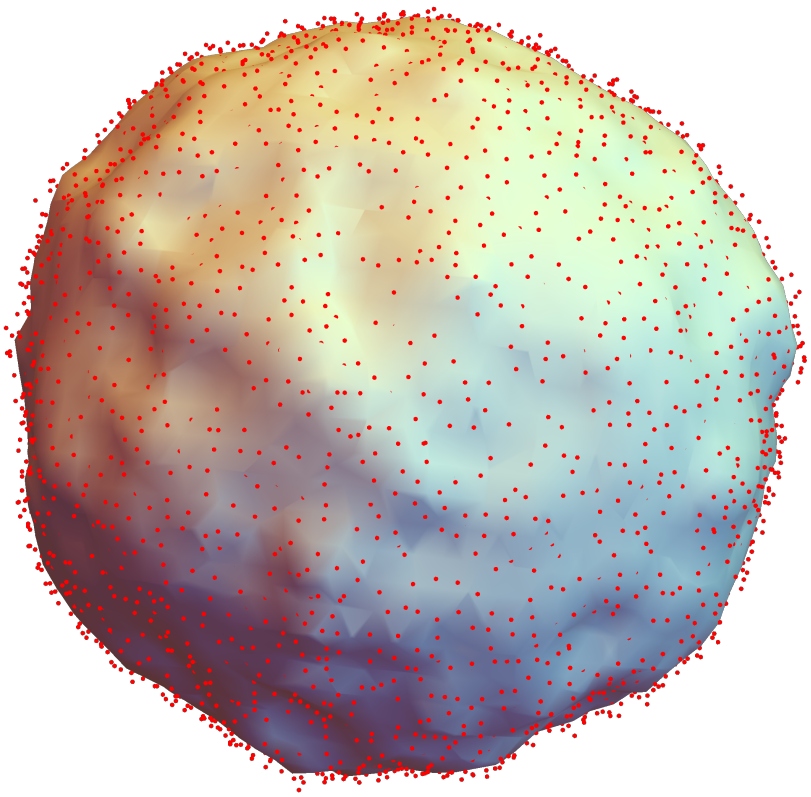

Figure 4.13: The shape of our 3D membrane model at equilibrium. The red dots represent the particles in our 3D membrane model. The surface in this figure is made from the particles(the red dot) using Mathematica. The particles are triangulated and interact according to the Hamiltonian:
$H = \sum_{\text{faces}} \Big[(k_A(A - A_0)^2 + \sum_{i=1}^{3} k_\theta(\theta_i - \pi/3)^2 + \sum{}' k_\phi(\phi - \pi)^2) \Big]$, where $\sum_{\text{faces}}$ is a sum over the triangulated faces, A is the area of a triangulated face, θ_i are the angles inside a triangulated face, $\sum'$ denotes a sum over different adjacent faces and ϕ denotes the angle between two adjacent faces.

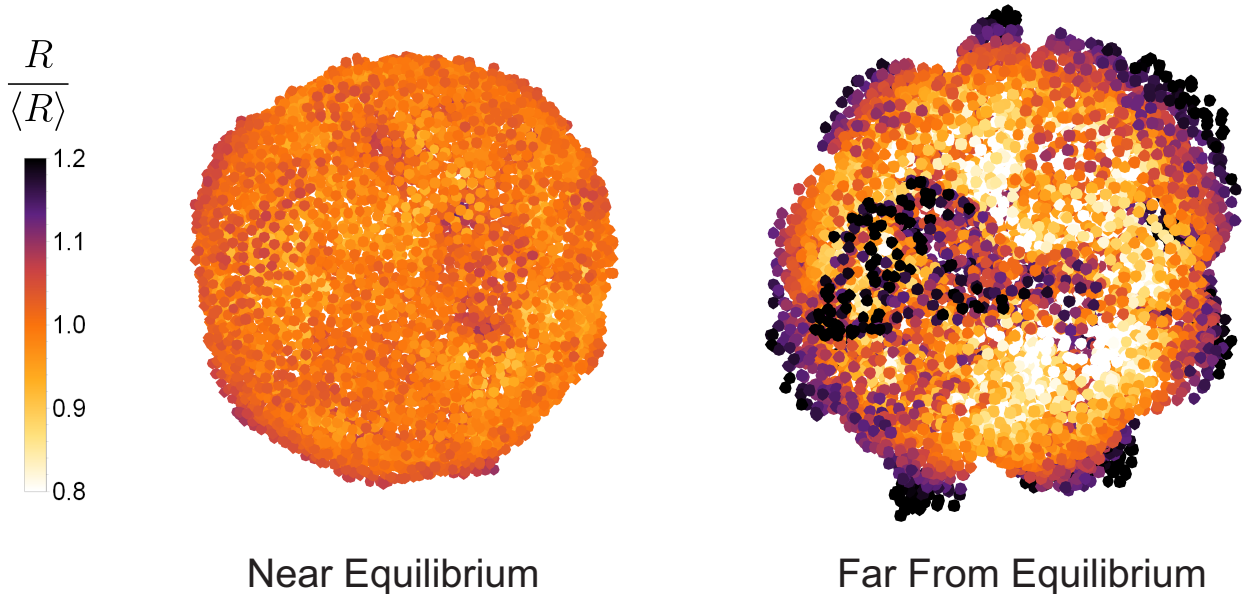

Figure 4.14: A heat map detailing the deviations of particles from the averaged radius of the assembly. The heat map on the left is for the assembly near equilibrium. The heat map on the right is for the assembly far from equilibrium. The fluctuations in the heat map on the right are reminiscent of the buckling observed in the 2D model far from equilibrium

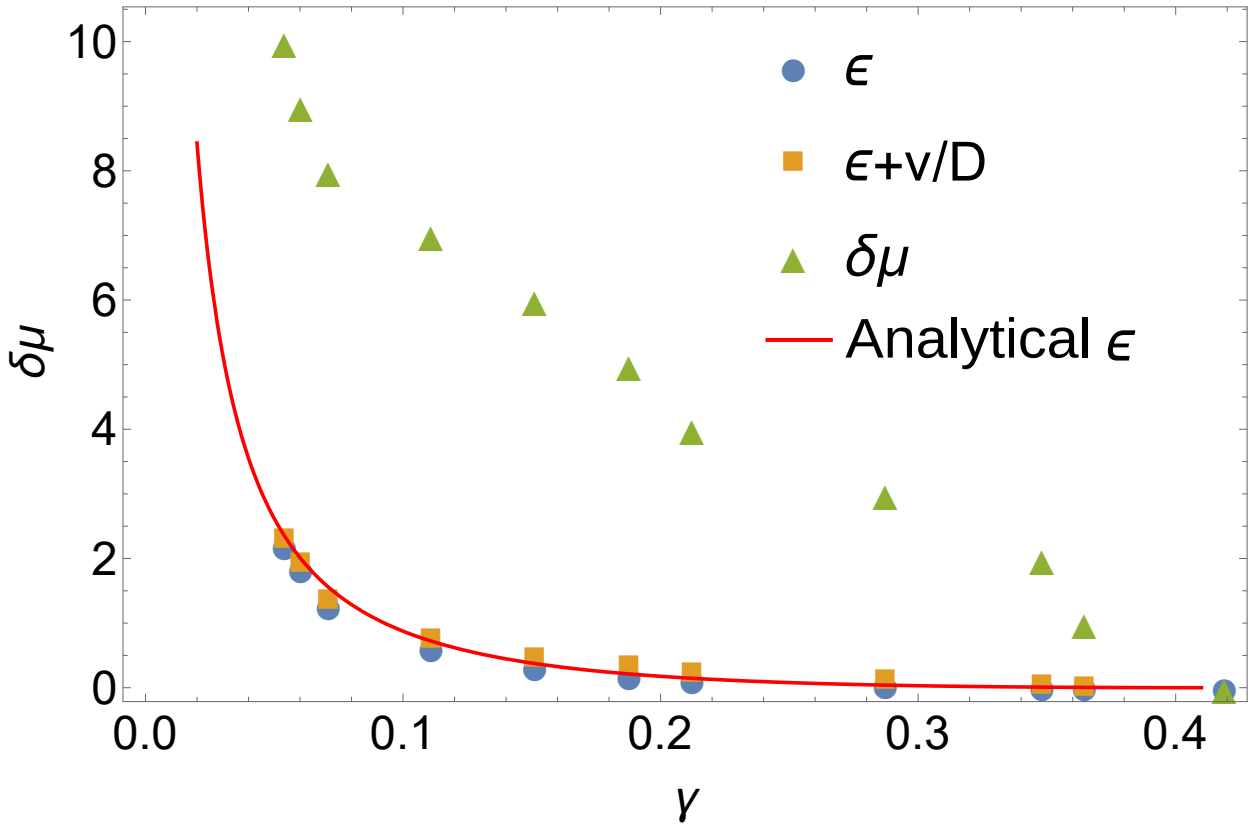

Figure 4.15: This figure is similar to Fig. 4.12 but for 3D model. The reorganization cost ϵ_{diss} is computed by decomposing the membrane fluctuations into spherical harmonic modes as explained in the text. We note that the contributions from v/D are much lower in the three dimensional membrane system than they are in the 2D membrane system. This could potentially be due to the fact that the overall particle flux $\dot{N}$ is coarse grained and hence provides a weak bound on the driving force $\delta\mu$. Further decomposing $\dot{N}$ into growth rates associated with various microscopic structures (such as individually considering growth rates of particles with connectivity $5, 6, 7$ might improve the performance of the bound. The red curve in the graph is the analytical result for ϵ_{diss}.

CHAPTER 5

APPLICATION TO THE SORTING OF ACTIN BUNDLE

5.1 Introduction

The actin cytoskeleton harnesses chemical energy to perform mechanical work that enables cells to migrate, divide, and exert forces on their surroundings, among other functions [72, 73, 74, 75, 76, 77]. To perform these varied functions, a cell must be able to control the organization of its many components in both space and time. A growing body of evidence suggests that, surprisingly, much of this organization can arise due to passive competition between actin-binding proteins (ABPs) [78]. At the same time, other processes such as the formation of a cytokinetic ring require irreversible polymerization and motor activity [79, 80]. This suggests that cells can regulate their internal structures and, in turn, function by tuning the relative contributions of passive and active processes. Support for this idea comes from recent *in vitro* experiments and simulations that demonstrate that the morphology of a growing actin bundle can be tuned not only by the binding affinities of the crosslinkers but also by the actin polymerization rates [27].

These observations, together with recent advances in non-equilibrium statistical mechanics [81, 82, 83, 84, 21, 41], raise the question of whether the non-equilibrium driving—here due to polymerization—can be related to the emergent structure *quantitatively*. Here, we address this question and present a theoretical framework that bounds the dynamics of a growing actin bundle. In particular, expanding from the previous chapters, we derive constraints on a set of three matrices characterizing the process—a matrix containing the various non-equilibrium driving forces ($\boldsymbol{\delta\mu}$, Eq. 5.23), a matrix encoding the equilibrium and non-equilibrium morphologies ($\mathbf{D}$, Eq. 5.24), and a matrix characterizing the covariance of the

molecular fluxes ($\mathbf{L^{-1}}$). For these three matrices, we show that

$$\mathrm{Tr}[\boldsymbol{\delta\mu} - \mathbf{D} - \mathbf{L^{-1}}] \geq 0\,, \mathrm{Det}[\boldsymbol{\delta\mu} - \mathbf{D} - \mathbf{L^{-1}}] \geq 0\,. \tag{5.1}$$

Eq. 5.1 has a flavor of the fluctuation-dissipation relation. Indeed, when the equality is satisfied, Eq. 5.1 can be used to obtain a linear-response-like formula connecting the non-equilibrium forcing, the bundle morphology, and the response to fluctuations in molecular fluxes (Eq. 5.25). Eq. 5.1 thus provides strong thermodynamic constraints on the non-equilibrium forcing, actin bundle morphology, and speed of growth. Notably, $\mathbf{D}$ and $\mathbf{L^{-1}}$ are experimentally accessible, such that Eq. 5.1 can be used to bound $\boldsymbol{\delta\mu}$, which is not straightforward to measure directly.

In what follows, we first outline a minimal model that captures the salient features of actin polymerization and bundling and show that it captures the observations described above. We then proceed to derive our central results and show how these thermodynamic uncertainty relations constrain the dynamics.

5.2 Actin polymerization drives sorting of actin bundling proteins

Inspired by the experiments in Refs. [2, 27], we consider a bundle consisting of two parallel actin filaments and two types of ABPs, α and β. The growth of a parallel actin bundle involves continuous actin monomer addition at one end, as well as continual binding and 'zipping' of the bundle by ABP binding at that same end. In the specific case shown in Fig. 5.1, α and β represent crosslinking proteins α-actinin and fascin, respectively, such that the bundles formed by the α ABPs are substantially more widely spaced than those formed by the β ABPs. Consequently, the bending penalty of actin implicitly favors addition of the current crosslinker at the growing end, as it costs energy to switch from one type to the

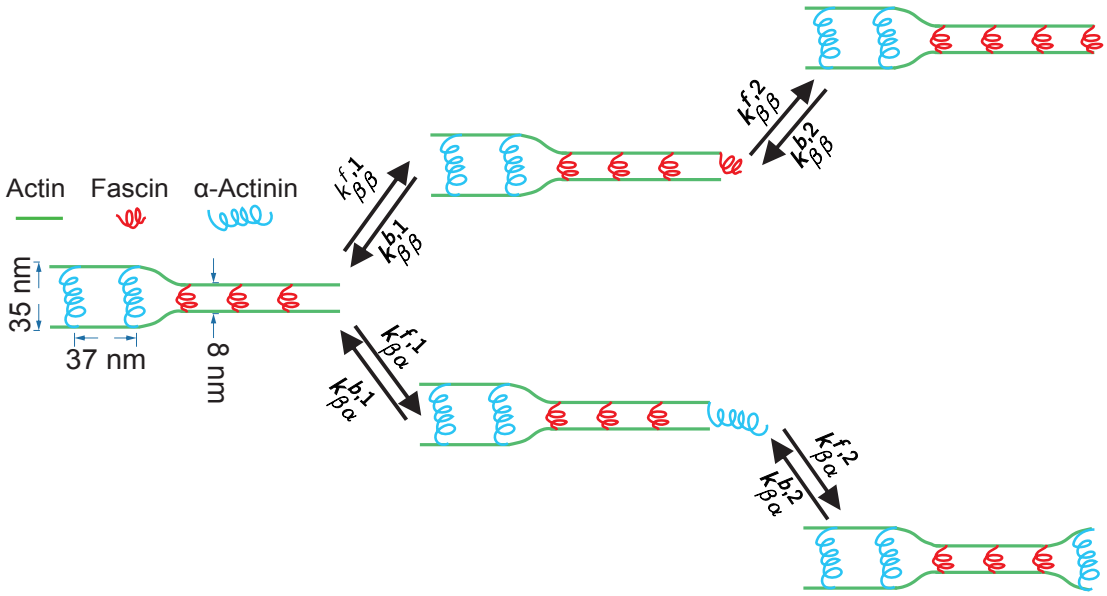

Figure 5.1: Schematic of adding one ABP at the tip of a growing actin bundle. Here, α and β represent α-actinin and fascin, which are 35 nm and 8 nm in size, respectively. The energetic cost of bending actin disfavors the binding a fascin after an α-actinin, or *vice versa*, resulting in domains of consecutive α or β types of ABPs. $k_{ij}^{f,1}$ and $k_{ij}^{b,1}$ ($k_{ij}^{f,2}$ and $k_{ij}^{b,2}$) are the forward and backward rates for the first (second) site of an ABP binding, where i and j are the types of the last two ABPs at the tip; $k_{\alpha\alpha}^{f,1} = k_{\beta\alpha}^{f,1}$ because both rates represent the binding of the first site of an α ABP (similarly, $k_{\beta\beta}^{f,1} = k_{\alpha\beta}^{f,1}$). An analogous schematic can be drawn for the case that the second-to-last ABP is α, and this case introduces four additional pairs of forward and backward rates with corresponding constraints.

other. Under conditions of equilibrium, the cost of bending actin favors the formation of distinct domains of only α or β ABPs. In the case of *in vitro* experiments using an equimolar mixture of fluorescently labeled α-actinin and fascin binding to growing actin bundles, these domains are on the order of several micrometers ($\sim$ 100 crosslinkers) long [2]. As noted above, it has been demonstrated that the domain length statistics can be modulated by the rate of actin polymerization [27] .

We construct a minimal model of this system with the following simplifications: first, we assume that the actin-binding proteins can only bind and unbind from the sites at the leading edge and not from the bulk of the bundle, and second, we assume that the two binding sites of each ABP bind sequentially and do not allow an ABP to bind to a single filament with both its sites. As a result, we need two pairs of forward rates $k_{ij}^{f,1}$ and backward rates $k_{ij}^{b,1}$ to describe the binding of first site of each ABP and two other pairs, $k_{ij}^{f,2}$ and $k_{ij}^{b,2}$, for their second site Fig. (5.1). The consideration of both ABP binding sites independently is more sophisticated than the kinetic Monte Carlo (KMC) models considered in Refs. [2, 27] but is consistent with the experimental and simulation data therein.

Here, we further decompose the forward rate of $k_{ij}^{f,m}$ into an equilibrium component, $k_{ij,eq}^{f,m}$, that satisfies a local detailed balance rule and accounts for all the energetics associated with ABP binding and filament deformations, and a component $dk_{ij}^{f,m}$ that can model any non-equilibrium contributions to the rate,

$$k_{ij}^{f,m} = k_{ij,eq}^{f,m} dk_{ij}^{f,m}. \tag{5.2}$$

We assert that only the forward rates are modified by any non-equilibrium effects, including actin polymerization, and we set all the $k_{ij}^{b,m}$ to unity. The equilibrium factor $k_{ij,eq}^{f,m}$ accounts for the binding affinity of an ABP. In cases where an attached ABP binds to the second actin filament, this equilibrium part also accounts for the energy penalty associated with bending the actin filament if the newly bound ABP is different from the previous ABP at the tip

(e.g., rate $k^{f,2}_{\beta\alpha,eq}$ in Fig. 5.1) and the free energy associated with zipping the actin bundle (e.g., rates $k^{f,2}_{\beta\beta,eq}$ and $k^{f,2}_{\beta\alpha,eq}$ in Fig. 5.1).

The non-equilibrium component in our model, $dk^{f,m}_{ij}$, heuristically accounts for any effects due to the finite rate of actin growth and polymerization, excess concentration or chemical potential of various ABPs in solution, and their molecular structure. Given this, we generically decompose the non-equilibrium components as

$$dk^{f,m}_{ij} = dk_j = 1 + f_{\text{molecular},j} f_{\text{density},j} f_{\text{pol},j} \tag{5.3}$$

where i and j are the types of ABPs at the bundle tip. The factor f_{pol} models the modulation of the rates due to the finite rate of growth of the actin filaments (k_{grow}). Specifically, over a time scale τ, the average increase in the number of binding sites on the filaments is $k_{\text{grow}}\tau$ and $k^{f,1}_{ij,eq}\tau$ is the number of binding events per binding site. Assuming Poisson statistics, the net rate of ABP binding is hence modulated by the factor,

$$f_{\text{pol},i} = 1 - e^{-k^{f,1}_{ii,eq} k_{\text{grow}} \tau^2} \tag{5.4}$$

The factor f_{pol} is essentially the probability of binding at least one ABP within time τ. f_{pol} increases from a value of 0 when k_{grow} is negligible to a value of 1 for rapid actin polymerization. It acts as a scaling factor that tunes the rates from their equilibrium values $k^{f,m}_{ij,eq}$ to their maximum rates.

The ABP concentrations also influence the rates of ABP binding in solution around the actin filaments. The phenomenological factor f_{density} accounts for these effects. Finally, the phenomenological factor, $f_{\text{molecular}}$ has been introduced to account for any remaining kinetic differences between the ABPs. Such factors could modulate the maximum rates of adding ABPs in fast-growing bundles. Still, they do not affect the equilibrium rates $k^{f,m}_{ij,eq}$ and the corresponding equilibrium structure of the bundle [27].

KMC simulations of this minimal model reproduce the crossover of domain lengths in fast-growing actin bundles (Fig. 5.2) [27]. It thus captures the essential physics of the system and serves as a meaningful starting point for the development of a theoretical framework that shows that a general energy-speed-morphology relation bounds the behavior.

5.3 Connections between the growth and morphology of actin bundles: A Markov state model

We now introduce a mean-field treatment for the various configurations that arise at the tip as ABPs associate and dissociate sequentially (Fig. 5.3). The forward rates $k_{ij}^{f,m}$ are consistent with those used in KMC simulations, accounting for the energetic terms in binding ABPs and the effect of actin polymerization. The backward rates in the finite-state model self-consistently account for the probability of finding the appropriate ABP in the bulk of the actin bundle. For instance, using L_α to denote the domain lengths of α type ABPs and L_β for its β counterpart, the probability of finding one α at the bundle tip is $L_\alpha/(L_\alpha + L_\beta)$ and the probability of finding a consecutive pair $\alpha\alpha$ is $(L_\alpha - 1)/(L_\alpha + L_\beta)$. The chance of reaching an $\alpha\alpha*$ configuration (where $*$ stands for half bound state as in Fig. 5.3) after unbinding an α at the bundle tip is essentially the conditional probability of finding $\alpha\alpha$ in the bundle given that the bundle tip is an α, which can be computed by dividing the $\alpha\alpha$ probability by the α probability to obtain $(L_\alpha - 1)/(L_\alpha)$. In computing the unbinding rate $k_{ij}^{b',m}$ used in the finite-state model, we multiply the backward rates $k_{ij}^{b,m}$ in KMC simulations by these corresponding conditional probabilities. Note that the effective backward rate for unbinding the first head of an ABP, $k_{ij}^{b',1}$, is equal to $k_{ij}^{b,1}$ in KMC simulations because the conditional probabilities in these transitions are 1. The difference in $k_{ij}^{b',1}$ and $k_{ij}^{b',2}$ is because the unbinding of an ABP's first site $k_{ij}^{b',1}$ initiates from state $ij*$ and reaches state i, so the type of the preceding ABP is known from the current state, while the unbinding of ABP's second site $k_{ij}^{b',2}$ initiates from state j and the type of the preceding ABP i is uncertain (see

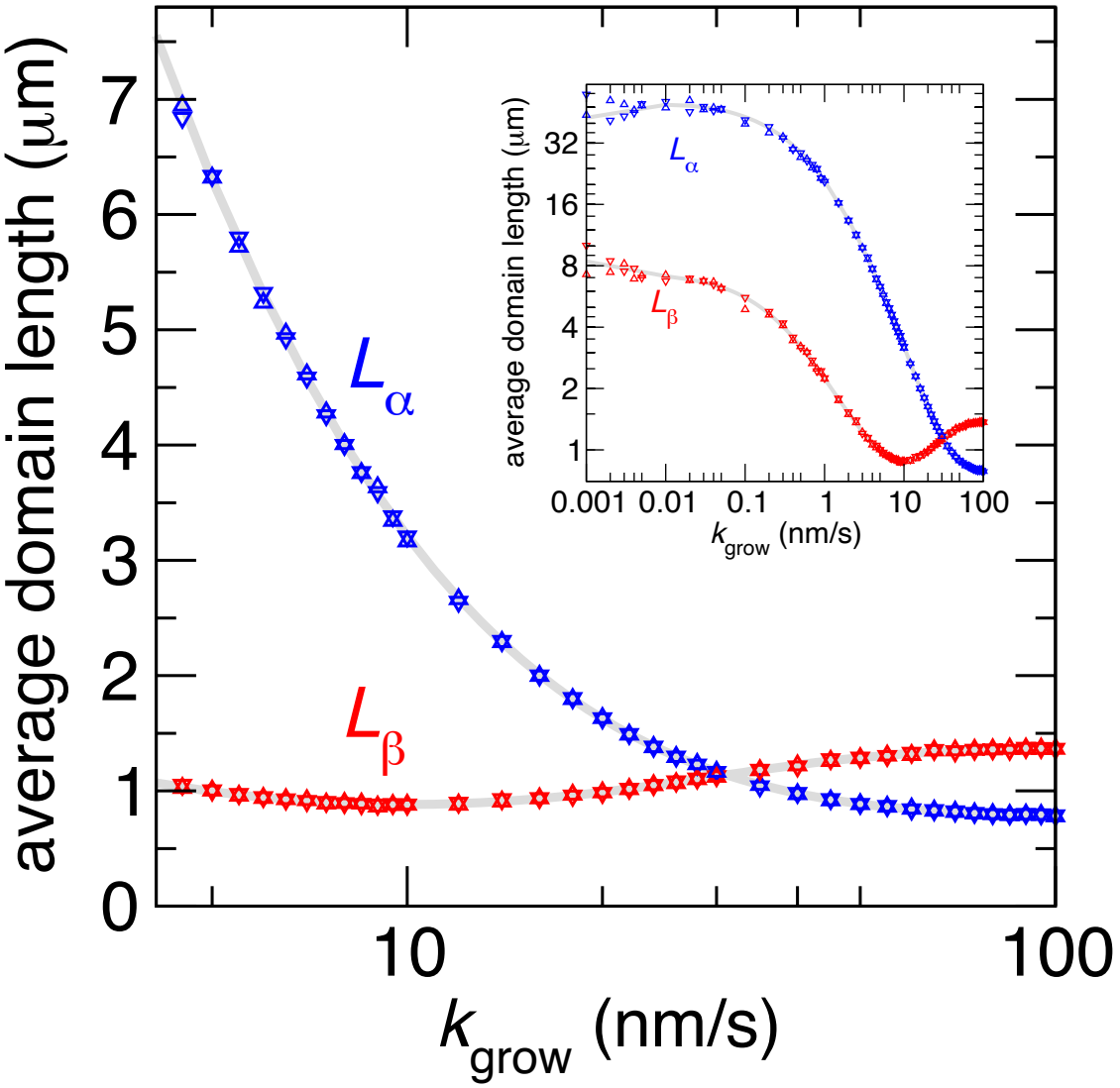

Figure 5.2: Average domain length of α and β ABPs as a function of polymerization rate k_{grow}. The distance between neighboring ABPs is assumed to be 0.037 μm in computing domain lengths [2]. Blue and red triangles are average domain lengths L_α and L_β measured from KMC simulations. Up and down triangles represent the average domain lengths measured in simulations with initial configurations composed of either all α or all β types of ABPs, respectively. Each data point is computed from a single KMC simulation of $S = 10^6$ steps. Gray lines (Eq. 5.7) are the domain lengths computed by self-consistently solving the master equation (Eq. 5.5). The parameters for both KMC simulations and the master equation are $k^{f,1}_{\alpha\alpha,eq} = 6$, $k^{f,1}_{\beta\beta,eq} = 2$, $f_{\text{density},\alpha} = f_{\text{density},\beta} = 100$, $f_{\text{molecular},\alpha} = 0.4$, $f_{\text{molecular},\beta} = 1$, $L_{\alpha,\text{eq}} = 900(33.3\mu\text{m})$, $L_{\beta,\text{eq}} = 300(11.1\mu\text{m})$ and $\tau = 1\text{s}$. The inset shows the domain lengths over a wider range of polymerization rates with the same symbols. The plateaus toward the left of the inset represent the domain lengths approaching their equilibrium values.

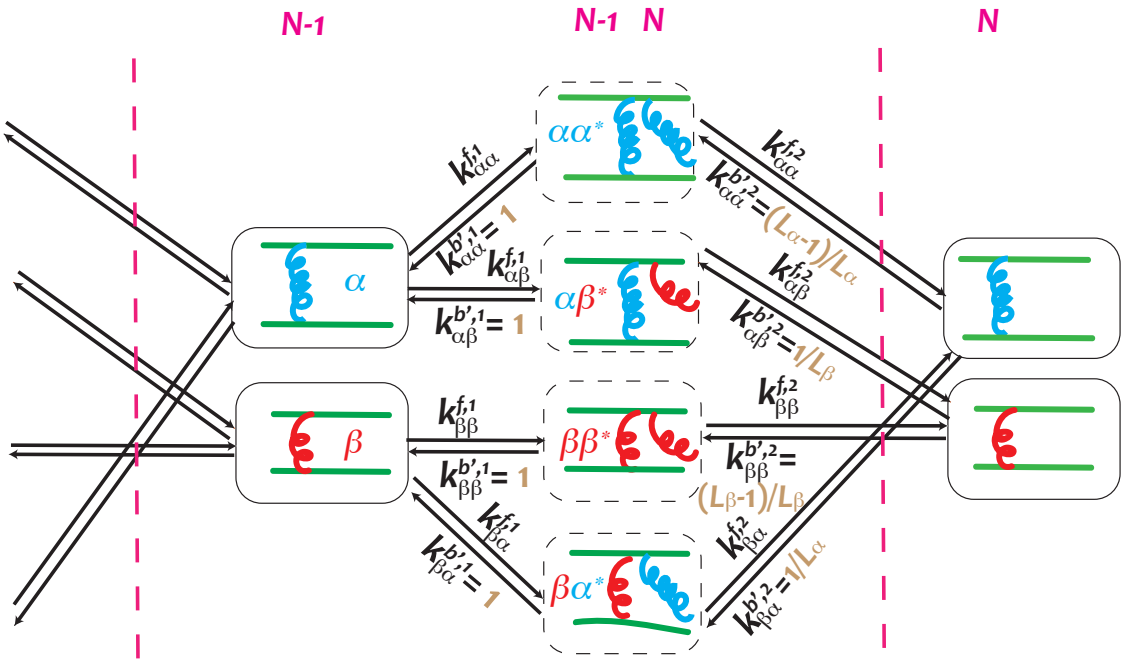

Figure 5.3: Schematic of the N^{th} cross-linker binds to the actin pairs. The states between two pink dashed lines describe the N^{th} ABP binding. Arrows link states between which the transitions are allowed. $k_{ij}^{f,m}$ and $k_{ij}^{b,m}$ are the forward and backward rates, where i and j are the types of the last two ABPs at the tip, and $*$ represents a half-bound state.

Fig. 5.3). We summarize the expressions of the rates in the KMC and the Mean Field Master Equations in the following table.

Table 5.1: Forward and Backward rates for ABP in Master Equation (ME) and KMC Simulations

	Forward Rates	ME and KMC	Backward Rates	ME	KMC
First head of ABP	$k^{f,1}_{\alpha\alpha}$	$k^{f,1}_{\alpha\alpha} = k^{f,1}_{\beta\alpha}$	$k^{b',1}_{\alpha\alpha}$ or $k^{b,1}_{\alpha\alpha}$	1	1
	$k^{f,1}_{\alpha\beta}$		$k^{b',1}_{\alpha\beta}$ or $k^{b,1}_{\alpha\beta}$	1	1
	$k^{f,1}_{\beta\beta}$	$k^{f,1}_{\beta\beta} = k^{f,1}_{\alpha\beta}$	$k^{b',1}_{\beta\beta}$ or $k^{b,1}_{\beta\beta}$	1	1
	$k^{f,1}_{\beta\alpha}$		$k^{b',1}_{\beta\alpha}$ or $k^{b,1}_{\beta\alpha}$	1	1
Second head of ABP	$k^{f,2}_{\alpha\alpha}$		$k^{b',2}_{\alpha\alpha}$ or $k^{b,2}_{\alpha\alpha}$	$(L_\alpha - 1)/L_\alpha$	1
	$k^{f,2}_{\beta\alpha}$		$k^{b',2}_{\beta\alpha}$ or $k^{b,2}_{\beta\alpha}$	$1/L_\alpha$	1
	$k^{f,2}_{\beta\beta}$		$k^{b',2}_{\beta\beta}$ or $k^{b,2}_{\beta\beta}$	$(L_\beta - 1)/L_\beta$	1
	$k^{f,2}_{\alpha\beta}$		$k^{b',2}_{\alpha\beta}$ or $k^{b,2}_{\alpha\beta}$	$1/L_\beta$	1

Given these expressions for the rates, we can write a master equation describing the evolution of probabilities of the various *tip* configurations, P_{ij}:

$$\begin{aligned} WP = \sum_{i,j=\alpha,\beta} (k^{f,1}_{ij} P_i - k^{b',1}_{ij} P_{ij*} \\ + k^{f,2}_{ij} P_{ij*} - k^{b',2}_{ij} P_j) = 0. \end{aligned} \tag{5.5}$$

Together with the mean field relations at steady state as demonstrated in the last chapters:

$$\begin{aligned} J_{N-1,\alpha,N,\alpha} &= \frac{L_\alpha - 1}{L_{\text{tot}}} J_{\text{tot}} \\ J_{N-1,\beta,N,\beta} &= \frac{L_\beta - 1}{L_{\text{tot}}} J_{\text{tot}} \\ J_{N-1,\alpha,N,\beta} = J_{N-1,\beta,N,\alpha} &= \frac{1}{L_{\text{tot}}} J_{\text{tot}} \end{aligned} \tag{5.6}$$

here $N-1, i, N, j$ denotes the tip configurations at position $N-1$ and N, J_{tot} is the sum of the four currents, and $L_{\text{tot}} \equiv L_\alpha + L_\beta$. The master equation (Eq. 5.5) can now be solved and expressions for the non-equilibrium domain lengths L_α and L_β can also be readily obtained:

$$L_\beta = \frac{(L_\alpha - 1)k^{f,2}_{\beta\alpha} - k^{f,2}_{\alpha\alpha}(L_\alpha(k^{f,2}_{\beta\alpha}+1)k^{f,1}_{\alpha\alpha} + L_\alpha - 1)}{k^{f,2}_{\beta\alpha}k^{f,1}_{\alpha\alpha}(L_\alpha k^{f,2}_{\alpha\alpha}((1+k^{f,2}_{\alpha\beta})k^{f,1}_{\alpha\alpha} - (L_\alpha - 1)k^{f,2}_{\alpha\beta}k^{f,1}_{\beta\beta}) - (L_\alpha - 1)(1 + k^{f,2}_{\alpha\beta} + L_\alpha k^{f,2}_{\alpha\beta}k^{f,1}_{\beta\beta}))}$$

$$L_\alpha = \frac{(L_\beta - 1)k^{f,2}_{\alpha\beta} - k^{f,2}_{\beta\beta}(L_\beta(k^{f,2}_{\alpha\beta}+1)k^{f,1}_{\beta\beta} + L_\beta - 1)}{k^{f,2}_{\alpha\beta}k^{f,1}_{\beta\beta}(L_\beta k^{f,2}_{\beta\beta}((1+k^{f,2}_{\beta\alpha})k^{f,1}_{\beta\beta} - (L_\beta - 1)k^{f,2}_{\beta\alpha}k^{f,1}_{\alpha\alpha}) - (L_\beta - 1)(1 + k^{f,2}_{\beta\alpha} + L_\beta k^{f,2}_{\beta\alpha}k^{f,1}_{\alpha\alpha}))} \tag{5.7}$$

We measure the currents and domain lengths from KMC simulations, and Fig. 5.2 demonstrates the validity of the relations between the fluxes and domain lengths in Fig. 5.6. The gray lines in Fig. 5.2 illustrate that these predictions are in excellent agreement with the domain lengths in KMC simulations for the full range of actin polymerization rates. This model also recovers the trend shown previously by simulations [27] that as the binding affinity of the short crosslinker (equivalent to β ABP in our model) is weakened, the crossover of domain lengths is deferred to a faster growth speed. Thus our mean-field treatment is able to capture the behavior of the model quantitatively.

5.4 Thermodynamic constraints between the non-equilibrium forcing, fluctuations, and morphology

The non-equilibrium thermodynamics of the growing actin bundle can now be probed. Using the master equation (Eq. 5.5) and the finite-state Markov model in Fig. 5.3, the entropy production rate $\dot{\sigma}$ for our effective Markov model can be written as

$$\dot{\sigma} = J_{\text{tot}}(\Delta\mu - \epsilon_{diss}) \geqslant 0. \tag{5.8}$$

The factor $\Delta\mu$ represents the non-equilibrium forces driving polymerization; it is defined as

$$\Delta\mu = \frac{2}{L_{\text{tot}}} \left(\sum_{i}^{\alpha,\beta} L_i \log dk_i \right). \tag{5.9}$$

The factor ϵ_{diss} is a measure of the difference between the non-equilibrium and equilibrium morphologies as characterized by the respective average domain lengths $L_{\beta,\text{eq}}$ and $L_{\alpha,\text{eq}}$.

$$\begin{aligned} \epsilon_{diss} = -\frac{1}{L_{\text{tot}}} \Bigg(& \sum_{i}^{\alpha,\beta} L_i \log \frac{L_i}{L_{i,\text{eq}}} \\ & - \sum_{i}^{\alpha,\beta} (L_i - 1) \log \frac{L_i - 1}{L_{i,\text{eq}} - 1} \Bigg). \end{aligned} \tag{5.10}$$

When we compare the expression of the ϵ_{diss} to the one in Eq. 3.21, we see that some of the terms are very similar. In fact, the expression for the ϵ_{diss} in Eq. 5.10 can be readily obtained if we were to use the energy expression of a 1D-Ising model with an effective magnetic constant and magnetic field. This suggests that the expression of ϵ_{diss}, in general, does not matter if the process goes through many intermediate states. We can also rewrite the expression of the entropy production in vector form:

$$\dot{\sigma} = J_{\text{tot}}(\Delta\mu - \epsilon_{diss}) = 2\mathbf{J}^T \left(\mathbf{dk} - \mathbf{D}[\mathbf{p}] \right) \tag{5.11}$$

with $\mathbf{J}^T = (J_\alpha, J_\beta)$, the rates in which the crosslinkers are being added into the system. The microscopic force vector $\mathbf{dk}$ and the relative entropy term $\mathbf{D}[\mathbf{p}]$ are defined as

$$\begin{aligned} \mathbf{dk} &= \begin{pmatrix} \log dk_\alpha \\ \log dk_\beta \end{pmatrix} \\ \mathbf{D}[\mathbf{p}] &= \begin{pmatrix} D(P(\alpha)||P^{eq}(\alpha)) \\ D(P(\beta)||P^{eq}(\beta)) \end{pmatrix} \end{aligned} \tag{5.12}$$

with

$$D(P(i)||P^{eq}(i)) = \frac{L_i - 1}{2L_i}(\log \frac{L_i - 1}{L_i} - \log \frac{L_{i,\text{eq}} - 1}{L_{i,\text{eq}}}) + \frac{1}{2L_i}(\log \frac{1}{L_i} - \log \frac{1}{L_{i,\text{eq}}}) \tag{5.13}$$

Eq. 5.8 is a statement of the second law of thermodynamics. However, we can improve on this bound substantially by adapting recent works in [85, 86]. Specifically, let's consider general currents J_g that can be written as a linear combination of edge currents j in the Markov networks according to:

$$J_g(n) = \sum_{\epsilon} j(\epsilon) d(\epsilon, n) \tag{5.14}$$

here $d(n, \epsilon)$ are elements in a matrix $\mathbf{d}$ that describes how each of the generalized currents depends on the edge currents.

We now proceed by first "inverting" Eq. 5.14 and defining a set of edge currents:

$$\tilde{j}(\epsilon) = \sum_{n} J_g(n) G(n, \epsilon) \tag{5.15}$$

where $\mathbf{G}$ is a pseudoinverse of the matrix $\mathbf{d}$. Note that since $\mathbf{G}$ and $\mathbf{d}$ are pseudoinverses of one another, we have

$$\sum_{\epsilon} \tilde{j}(\epsilon) d(\epsilon, k) = \sum_{n,\epsilon} J_g(n) G(n, \epsilon) d(\epsilon, k) = \sum_{n,\epsilon,\epsilon'} j(\epsilon') d(\epsilon', n) G(n, \epsilon) d(\epsilon, k) = \sum_{\epsilon'} j(\epsilon') d(\epsilon', k) = J_g(k) \tag{5.16}$$

Eq. 5.16 suggests that the sets of currents $\tilde{\mathbf{j}}$ do not have to be identical to $\mathbf{j}$. The matrix $\mathbf{G}$, however, has to be constructed to ensure that the resulting sets of currents $\tilde{\mathbf{j}}$ meet the following two requirements: first, the sets of $\tilde{\mathbf{j}}$ satisfy current conservation; second, the resulting sets of $\tilde{\mathbf{j}}$ at steady state match $\mathbf{j}$ at steady state.

Then, we use the findings of Ref. [21] which showed that the large deviation rate functions

associated with the fluctuations in the various edge currents satisfy the following inequality,

$$I(\mathbf{j}) \leq \sum_{\epsilon} \left(j(\epsilon) - j^{\pi}(\epsilon)\right)^2 \frac{\sigma^{\pi}(\epsilon)}{4[j^{\pi}(\epsilon)]^2}, \tag{5.17}$$

where $I(\mathbf{j})$ is the rate function of the edge currents, j^{π} is the average current of the edge and $\sigma^{\pi}(\epsilon)$ is the entropy production of edge ϵ. Note that the entropy production along the edge ϵ that links states i and j with forward rate k_{ij} and backward rates k_{ji} can be written as $\sigma^{\pi}(\epsilon) = j^{\pi}(\epsilon) \log \frac{k_{ij}P_i}{k_{ji}P_j}$. The sum of entropy production along all the edges should result in the total entropy as in Eq. 5.11.We can then use the arguments in Ref. [21, 85] to substitute Eq. 5.15 into Eq. 5.17 and obtain a bound on the large deviation rate function associated with the generalized currents, $I(\mathbf{J_g})$

$$I(\mathbf{J_g}) \leq \sum_{\epsilon} \left(\sum_{\mathbf{n}} \mathbf{J_g}(\mathbf{n})\mathbf{G}(\mathbf{n},\epsilon) - \mathbf{J_g^{\pi}}(\epsilon)\mathbf{G}(\mathbf{n},\epsilon) \right)^{\mathbf{2}} \frac{\sigma^{\pi}(\epsilon)}{\mathbf{4}[\mathbf{j}^{\pi}(\epsilon)]^{\mathbf{2}}}. \tag{5.18}$$

Now we consider the system at steady state, with $\mathbf{J_g}^{\pi}$ denoting the vector of average generalized currents and $\mathbf{J_g}$ denoting the covariance of generalized currents. The rate function $I(\mathbf{J_g})$ can be expanded around the average generalized currents, $\mathbf{J_g}^{\pi}$, as

$$I(\mathbf{J_g}) \approx I(\mathbf{J_g}^{\pi}) + D\left[I(\mathbf{J_g})|\mathbf{J_g}^{\pi}\right] \cdot \tilde{\mathbf{J}}_\mathbf{g} + \frac{1}{2}\tilde{\mathbf{J}}_\mathbf{g}^T \cdot H\left[I(\mathbf{J_g})|\mathbf{J_g}^{\pi}\right] \cdot \tilde{\mathbf{J}}_\mathbf{g} \tag{5.19}$$

Here $\tilde{\mathbf{J}}_\mathbf{g}$ is a vector with elements $(\mathbf{J_g}(\mathbf{n}) - \mathbf{J_g}^{\pi}(\mathbf{n}))$, and $D\left[I(\mathbf{J_g})|\mathbf{J_g}^{\pi}\right]$ is the vector containing the derivatives of the rate function $I(\mathbf{J_g})$ with respect to the current $\mathbf{J_g}$. Since the rate function is at its minimum at $\mathbf{J_g}^{\pi}$, $I(\mathbf{J_g}^{\pi})$ and $D\left[I(\mathbf{J_g})|\mathbf{J_g}^{\pi}\right]$ equal zero. $H\left[I(\mathbf{J_g})|\mathbf{J_g}^{\pi}\right]$ is the Hessian matrix of $I(\mathbf{J_g})$ evaluated at $\mathbf{J_g}^{\pi}$ which can be related to the covariance matrix $\mathbf{L}$ as shown in [87]:

$$H\left[I(\mathbf{J_g})|\mathbf{J_g}^{\pi}\right] = \mathbf{L}^{-\mathbf{1}}. \tag{5.20}$$

Eq. 5.19 and Eq. 5.20 then allow us to rewrite Eq. 5.18 as

$$\tilde{\mathbf{J}}_{\mathbf{g}}^{T} \cdot \mathbf{L}^{-1} \cdot \tilde{\mathbf{J}}_{\mathbf{g}} \leq \tilde{\mathbf{J}}_{\mathbf{g}}^{T} \cdot \mathbf{GSG^{T}} \cdot \tilde{\mathbf{J}}_{\mathbf{g}} \tag{5.21}$$

Here $\mathbf{G}$ is the matrix form of $G(n, \epsilon)$ with n indicating the row and ϵ indicating the column, $\mathbf{G^{T}}$ is its transpose and $\mathbf{S}$ is a diagonal matrix with elements $\sigma^{\pi}(\epsilon)/2|j^{\pi}(\epsilon)|^{2}$. Since Eq. 5.18 is valid for any arbitrary fluctuation about the mean, $\mathbf{GSG}^{T} - \mathbf{L}^{-1}$ has to be positive semi-definite, which is to say that all of its eigenvalues have to be non-negative. For a 2×2 matrix, this is equivalent to

$$\mathrm{Tr}(\mathbf{GSG}^{\mathrm{T}} - \mathbf{L}^{-1}) \geq 0, \quad \mathrm{Det}(\mathbf{GSG}^{\mathrm{T}} - \mathbf{L}^{-1}) \geq 0. \tag{5.22}$$

We then rewrite $\mathbf{GSG}^{T}$ into $\boldsymbol{\delta\mu} - \mathbf{D}$ where $\boldsymbol{\delta\mu}$ contains all the term with the driving forces: $dk_{\alpha/\beta}$ while $\mathbf{D}$ contains the rest.

We now define the matrices $\boldsymbol{\delta\mu}$, $\mathbf{D}$ and $\mathbf{L^{-1}}$ precisely. This is mainly determined by the choice of the general currents in interest. In this system, the two important currents are the J_{α} and J_{β}, the rate in which the crosslinkers are being added into the system. With this choice, we can write down a matrix $\boldsymbol{d}$ that relates the particle currents $\boldsymbol{J}$ to the edge currents $\boldsymbol{j}$ and its pseudo-invert matrix $\boldsymbol{G}$ with the conditions: the resulting currents $\tilde{\mathbf{j}} = \mathbf{G^{T}J}$ satisfy current conservation and the match $\mathbf{j}$ at steady state. With this and some algebra, the matrix $\boldsymbol{\delta\mu}$ becomes:

$$\boldsymbol{\delta\mu} = \begin{pmatrix} \delta\mu_{\alpha}\gamma_{1}^{\alpha} + \delta\mu_{\beta}\gamma_{2}^{\beta} & \delta\mu_{\alpha}\gamma_{3}^{\alpha} + \delta\mu_{\beta}\gamma_{3}^{\beta} \\ \delta\mu_{\alpha}\gamma_{3}^{\alpha} + \delta\mu_{\beta}\gamma_{3}^{\beta} & \delta\mu_{\alpha}\gamma_{2}^{\alpha} + \delta\mu_{\beta}\gamma_{1}^{\beta} \end{pmatrix} \tag{5.23}$$

where $\delta\mu_{\alpha/\beta} \equiv \log dk_{\alpha/\beta}$, $\gamma_{1}^{\alpha/\beta} \equiv [(L_{\mathrm{tot}} - 1)^{2}/(L_{\alpha/\beta} - 1) + 1]/L_{\mathrm{tot}}$, $\gamma_{2}^{\alpha/\beta} \equiv [1/(L_{\alpha/\beta} - 1) + 1]/L_{\mathrm{tot}}$, and $\gamma_{3}^{\alpha/\beta} \equiv -L_{\beta/\alpha}/[L_{\mathrm{tot}}(L_{\alpha/\beta} - 1)]$. The matrix $\mathbf{D}$ depends on the non-equilibrium

and equilibrium domain lengths of ABPs and is defined as

$$\mathbf{D} = \begin{pmatrix} dp_\alpha \gamma_1^\alpha + dp_\beta \gamma_2^\beta + \epsilon & dp_\alpha \gamma_3^\alpha + dp_\beta \gamma_3^\beta + \epsilon \\ dp_\alpha \gamma_3^\alpha + dp_\beta \gamma_3^\beta + \epsilon & dp_\alpha \gamma_2^\alpha + dp_\beta \gamma_1^\beta + \epsilon \end{pmatrix} \tag{5.24}$$

where $dp_{\alpha/\beta} \equiv (1/2)(\ln[(L_{\alpha/\beta}-1)/L_{\alpha/\beta}]-\ln[(L^{\rm eq}_{\alpha/\beta}-1)/L^{\rm eq}_{\alpha/\beta}])$ and $\epsilon \equiv (1/(2L_{\rm tot}))(\ln[(L^{\rm eq}_\alpha-1)/(L_\alpha-1)]+\ln[(L^{\rm eq}_\beta-1)/(L_\beta-1)])$. The $\mathbf{D}$ matrix only depends on the equilibrium and non-equilibrium morphologies of the bundle. $\mathbf{L^{-1}}$ is proportional to the inverse of the covariance matrix of fluxes and is computed as $\mathbf{L^{-1}} \equiv \lim_{t\to\infty} J_{\rm tot}\mathbf{M}^{-1}/t$, in which $\mathbf{M}$ has the elements $M_{ij} = \langle \delta J_i \delta J_j \rangle$ and t is the time of growth. In Fig. 5.4, we numerically verify Eq. 5.1 for various parameter combinations. The equality in Eq. 5.21 holds only when $\boldsymbol{\delta\mu} - \mathbf{D} = \mathbf{L^{-1}}$. In that case multiplying Eq. 5.21 by the column vector $\mathbf{J}$ we readily obtain

$$\mathbf{dk} - \mathbf{D}[\mathbf{p}] = \tilde{\mathbf{L}}^{-1} \cdot \mathbf{J} \tag{5.25}$$

where $\tilde{\mathbf{L}}^{-1} \equiv \mathbf{L}^{-1}/J_{\rm tot}$, $\mathbf{dk}$ and $\mathbf{D}[\mathbf{p}]$ are defined in Eq. 5.12. Eq. 5.25 can be viewed as an extension of the fluctuation dissipation relation to our non-equilibrium bundling and polymerization process. It relates the various driving forces $\mathbf{dk}$ and a relative entropic measure of the distance between the non-equilibrium and equilibrium structures, $\mathbf{D}[\mathbf{p}]$, to the various observed fluxes $\mathbf{J}$ through the flux covariance matrix $\tilde{\mathbf{L}}^{-1}$.

5.5 Connection to the Thermodynamics Uncertainty Relations

The so called thermodynamic uncertainty relations (TUR) [84, 21, 86, 88, 85] can also be readily derived from Eq. 5.1. The TURs have emerged as universal constraints on the fluctuations of currents in non-equilibrium processes, which present tighter bounds for microscopic driving compared than the second law (Eq. 5.8). Specifically, our central results in Eq. 5.1 implies that $\tilde{\mathbf{J}}^T \cdot [\boldsymbol{\delta\mu} - \mathbf{D} - \mathbf{L^{-1}}] \cdot \tilde{\mathbf{J}} \geq 0$ for any vector $\tilde{\mathbf{J}}$. Hence, this TUR bound takes

into account the correlation between individual molecular fluxes and we derive the following multidimensional thermodynamic relation (MTUR) [86] for biopolymer bundling:

$$J_{\text{tot}}(\Delta\mu - \epsilon_{diss}) = 2\mathbf{J}^{\intercal} \cdot (\mathbf{dk} - \mathbf{D}[\mathbf{p}]) \geqslant 2\mathbf{J}^{\intercal} \cdot \tilde{\mathbf{L}}^{-1}\mathbf{J}. \tag{5.26}$$

Our central result provides a connection between the microscopic driving forces represented by $\boldsymbol{\delta\mu}$ or $\mathbf{dk}$, the non-equilibrium structure of the bundle as encoded by matrix $\mathbf{D}$ or $\mathbf{D}[\mathbf{p}]$, and the fluctuations of the various fluxes denoted by $\mathbf{L^{-1}}$ (obtained in the non-equilibrium steady state). Experimentally, it is possible to measure the fluxes of various bundling proteins, and the structure of the bundles. Then, one can use Eq. 5.1 to bound the microscopic driving forces. These microscopic forces generally cannot be measured directly. Further, in non-equilibrium regimes where the $\mathbf{L^{-1}}$ matrix exhibits singular or close to singular behavior, our results suggest that the system might be insensitive to perturbations that tune the various microscopic driving forces, $\mathbf{dk}$. Our results suggest that the non-equilibrium bundling morphology can be effectively tuned away from such points.

Finally, Eq. 5.1 can also be used to assess the relative importance of accounting for the statistics of the individual fluxes. To do so, we use the TURs to derive a bound for the rate of entropy production in terms of the total flux, J_{tot}:

$$\Delta\mu \geqslant \epsilon_{diss} + \frac{2\langle J_{\text{tot}}\rangle}{t\left\langle \delta J_{\text{tot}}^2 \right\rangle}. \tag{5.27}$$

Here, t is the growth time of the bundle, $\langle J_{\text{tot}}\rangle$ is the average total flux of adding ABPs to the bundle, and $\left\langle \delta J_{\text{tot}}^2 \right\rangle$ is its variance. In Fig. 5.5, we compare the performance of Eq. 5.27 (brown) with that of Eq. 5.8 (blue). We see that the TUR bound is closer to the real driving $\Delta\mu$ compared with the second-law bound. Nevertheless, it still fails significantly at $k_{\text{grow}} \approx 1$ nm/s, where it only recovers about 6% of the actual driving. This implies that controlling the overall kinetics is not enough for facilitating the sorting of ABPs.

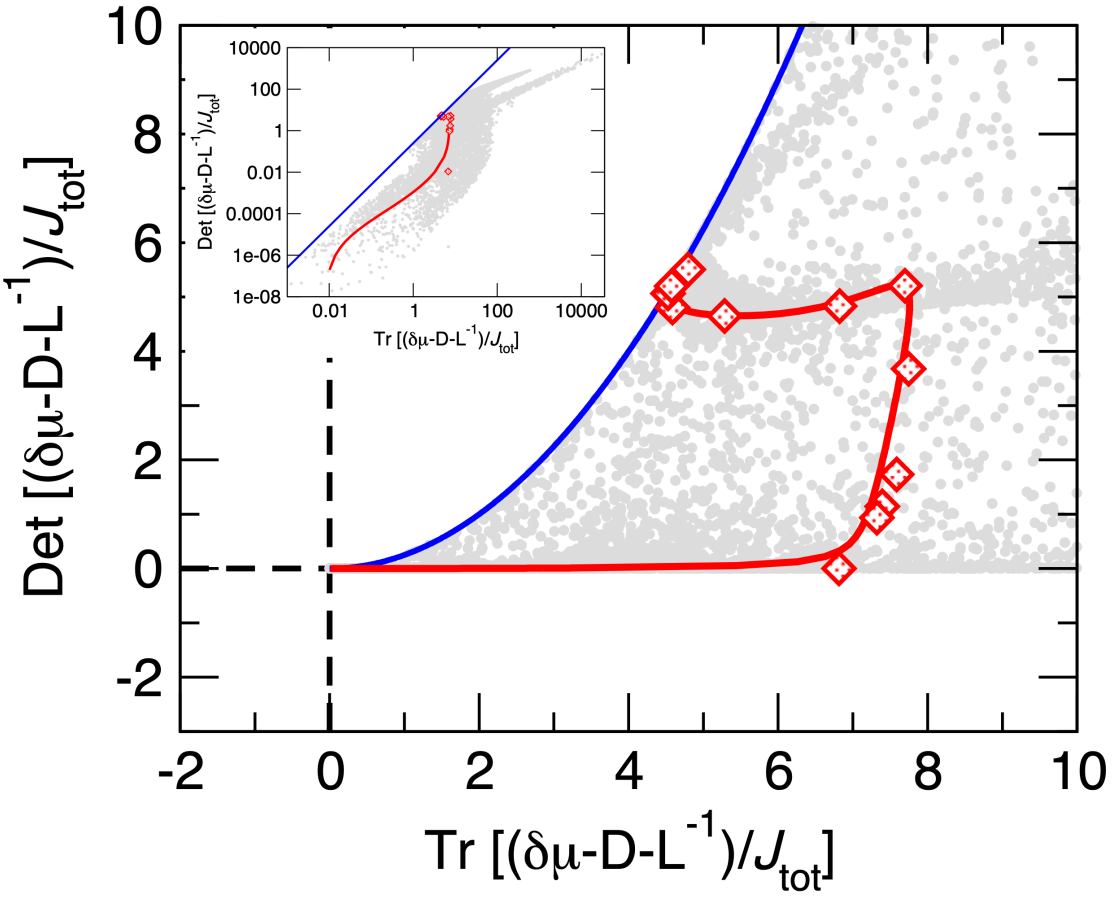

Figure 5.4: Numerical verification of Eq. 5.1. The blue boundary marks the location of the inequality $\mathrm{Tr}[\mathbf{M}] \geq 2\sqrt{\mathrm{Det}[\mathbf{M}]}$ for a two dimensional square matrix $\mathbf{M}$. The red diamonds are results from the non-equilibrium KMC simulations with the parameters used in Fig. 5.2 and the red line is the theoretical mean field prediction for those same parameters. Gray dots are computed by constructing the matrices $\boldsymbol{\delta\mu}$, $\mathbf{D}$, and $\mathbf{L^{-1}}$ using the the master equation results and computing the eigenvalues of $(\boldsymbol{\delta\mu} - \mathbf{D} - \mathbf{L^{-1}})/J_{\mathrm{tot}}$ using Mathematica [3] for randomly selected parameters from $L_{\beta,\mathrm{eq}} = [1, 90000]$, $f_{\mathrm{density},\beta} = [1, 100]$ and $k_{\mathrm{grow}} = [0.001, 100]$ nm/s, with all other parameters the same as the red line. The inset shows these two quantities for a wider range, with both axes in logarithmic scale. We do not consider $k_{\mathrm{grow}} < 0.001$ nm/s due to limitations of numerical precision. Eq. 5.1 provides strong constraints between the non-equilibrium forcing, morphology, and speed of growth.

In Fig. 5.5, we also plot the MTUR bound (Eq. 5.26) using cumulants of fluctuations in the individual fluxes from KMC simulations. Although not perfect, this bound recovers at least 46% of the actual driving $\Delta\mu$ for the full range of polymerization rates. The increasing gap between the MTUR bound and the actual driving is consistent with our central result in Fig. 5.4 that $\mathrm{Tr}[\boldsymbol{\delta\mu} - \mathbf{D} - \mathbf{L^{-1}}]$ becomes further away from zero as microscopic driving becomes stronger and makes growth faster.

5.6 Conclusions

In conclusion, we have derived a strong thermodynamic constraint relating the microscopic driving of a growing bundle (denoted by $\boldsymbol{\delta\mu}$ in Eq. 5.1), the morphology of the bundle in its non-equilibrium steady state as described by the matrix $\mathbf{D}$, and the statistics of the rates of incorporation of crosslinkers as described by the matrix $\mathbf{L^{-1}}$. Our central results, which can be viewed as extensions of the fluctuation dissipation relations, also have practical applications. As an example, they potentially provide a route to estimate microscopic driving forces (contained in the $\boldsymbol{\delta\mu}$ matrix) from experiments in which the various fluxes and morphologies are measured using microscopy and quantitative image analysis.

While this current work is focused exclusively on the growth dynamics of bundled actin networks, we anticipate that the formalism presented here can be used in other contexts, such as the interplay between structure, speed, and non-equilibrium forcing in the growth dynamics of branched actin networks [89, 90, 91], the self-organization of other ABPs to distinct actin network architectures (e.g., networks initiated by formin or the Arp2/3 complex) [78], and the sorting of ABPs to distinct networks under confinement [92].

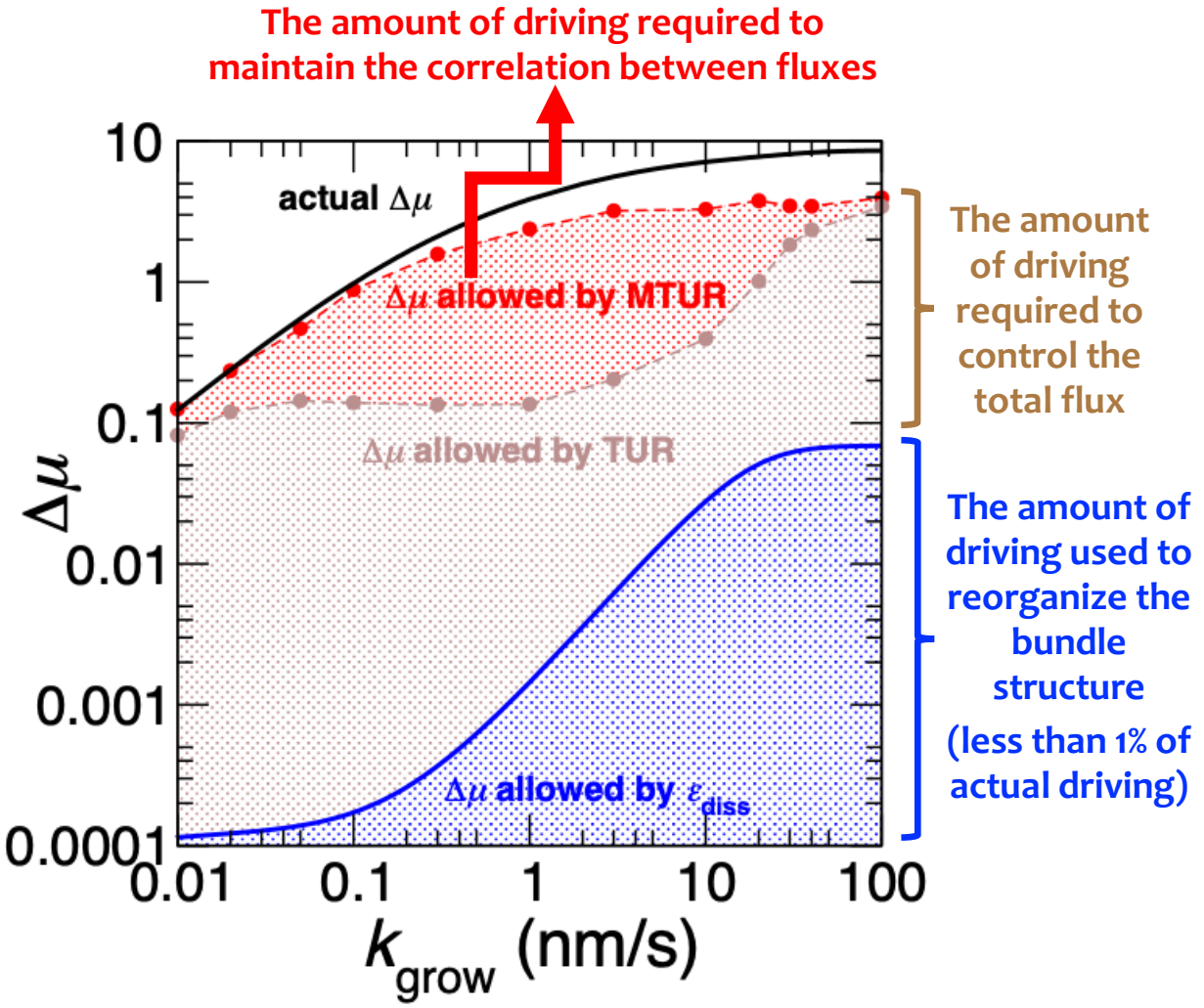

Figure 5.5: Comparison of bounds on the non-equilibrium driving force $\Delta\mu$. The black line(5.9)is the actual driving force predicted by the master equation. The blue curve(5.8) is the driving force required for morphology change. The brown (Eq. 5.27) and red (Eq. 5.26) lines are the thermodynamic bounds computed from KMC simulations using TUR and MTUR. Each of the brown and red data points is generated with 500 independent KMC simulations, each of 10^7 steps. All parameters of the KMC simulations are the same as in Fig. 5.2.

CHAPTER 6

EXTENSION TO TIME DEPENDENT DRIVE

6.1 Introduction

In the previous chapters, we have developed a framework to model non-equilibrium self-assembly at a steady-state and apply it to various growing systems such as actin and membrane. One important non-equilibrium self-assembly that we have not touched is assembly under periodic drive. Indeed, time-periodic forcing has been used to create non-equilibrium states with enhanced order in many contexts [93, 94, 95, 96, 97, 98, 99, 100]. It was showed that dynamic phase transition can occur by tuning the frequency of inputting the energy into the system [101, 102]. Unfortunately, there is no general framework to study how the pattern of the assembly changes under periodic drive or how entropy production plays a role in it. These issues will be the focus of this chapter.

Under the periodic drive, the self-assembly system is no longer steady-state, and many mean-field conditions in the previous chapters are no longer valid. In general, the mathematical treatment of deterministic periodic systems is not trivial, especially in calculating the entropy production [103]. However, we will show that many of our mean-field approaches can still be used to probe the periodic assembly effectively under certain conditions. Inspired by works in [104, 105, 106, 107, 108, 109, 110], we develop a more general treatment that works for wider conditions using bi-partite Markov Network. Finally, we will demonstrate the relationship between the entropy production and the regime in which a field is effectively driven into the assembly.

6.2 Model And Simulations

We consider a one-dimensional growth of an assembly made up of two kinds of particles as shown in Fig. 6.1. We will assign the red particle with a value of 1 and the blue particle

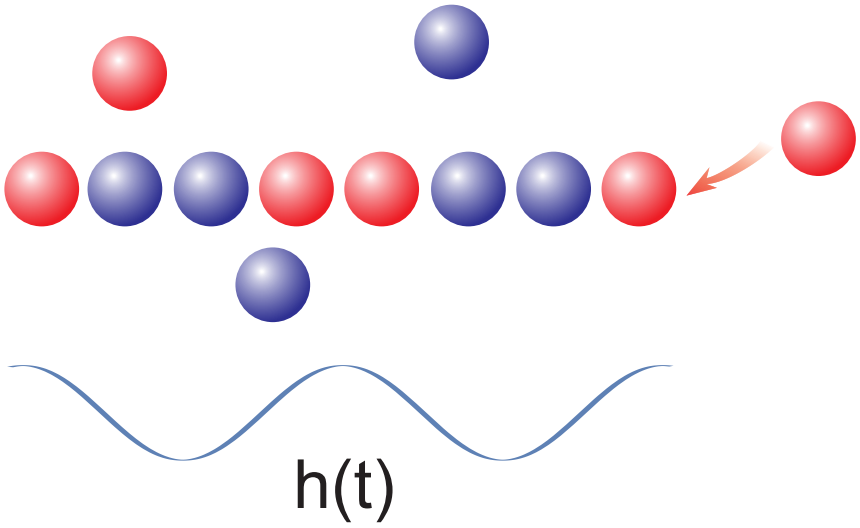

Figure 6.1: Schematic of the one dimension growth assembly with rates affected by a time-varying magnetic field h(t).

with -1. In this particular case, we will add particles into the assembly at a constant rate:

$$k_t^{add}(n_i, n_j \to n_j, n_k) = \exp(\mu) = \exp(\mu_{eq} + \delta\mu) \tag{6.1}$$

Here n represents the configurations/properties of the elements or particles that make up the assembly (like spins). μ is the chemical potential of the particles on the bath, which we have further separated into $\mu_{eq} + \delta\mu$. μ_{eq} is the chemical potential of the bath when the system is at equilibrium with no magnetic field, and $\delta\mu$ is the extra chemical potential driving the system. The particles, however, are removed with a time-dependent rate:

$$k_t^{rem}(n_k, n_i \leftarrow n_i, n_j) = \exp(-Jn_in_j - h\cos\left(\frac{2\pi t}{\omega}\right)n_j) \tag{6.2}$$

Here J is the magnetic constant, h is the amplitude of the magnetic field, t is time, and ω is the period. As the assembly grows, we only allow particles to attach or detach at the outermost block of the assembly. We then run simulations with the above rates using the First Reaction Method (FRM) [111]. In the limit of small ω, the magnetic field will oscillate

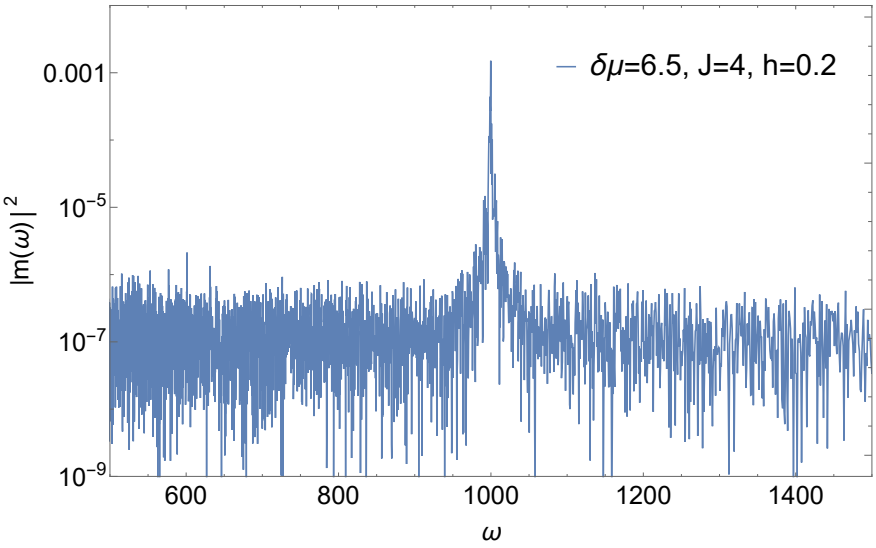

Figure 6.2: Fourier Transform of the assembly obtained using simulations at $\delta\mu = 6.5$, $J = 4$, $h = 0.2$ and $\omega = 1000$. The period of the peak is the same as the period of the magnetic field.

very fast, resulting in the assembly only see the average magnetic field. In the opposite limit, when the magnetic field is extremely slow, the assembly can be modeled using the steady-state equations at every instant in time. Both of these limits can be solved using the techniques we develop in previous chapters. Therefore, in this chapter, we will focus on the regime between these two extremes and investigate how an extra driving force $\delta\mu$ affects the pattern inside the assembly.

To analyze how well the magnetic field affects the pattern inside the assembly, we take the whole assembly generated by the simulation through a Fourier Transform. We then convert the frequency in the assembly to period in time using the growth rate: $\langle \dot{N} \rangle = \frac{N}{\omega}$. Fig. 6.2 shows the result of the Fourier Transform for an assembly consisted of 10^7 particles. The location of the peak of the Fourier Transform corresponded to the period, ω, of the magnetic field.

We repeat this analysis to assemblies obtained with $\delta\mu$ from the range: $\delta\mu : 4.0 - 9.0$ and plot the magnitude square of the peak varying with the number of particles in the assemblies which go through the Fourier Transform in Fig. 6.3. From Fig. 6.3, we see that

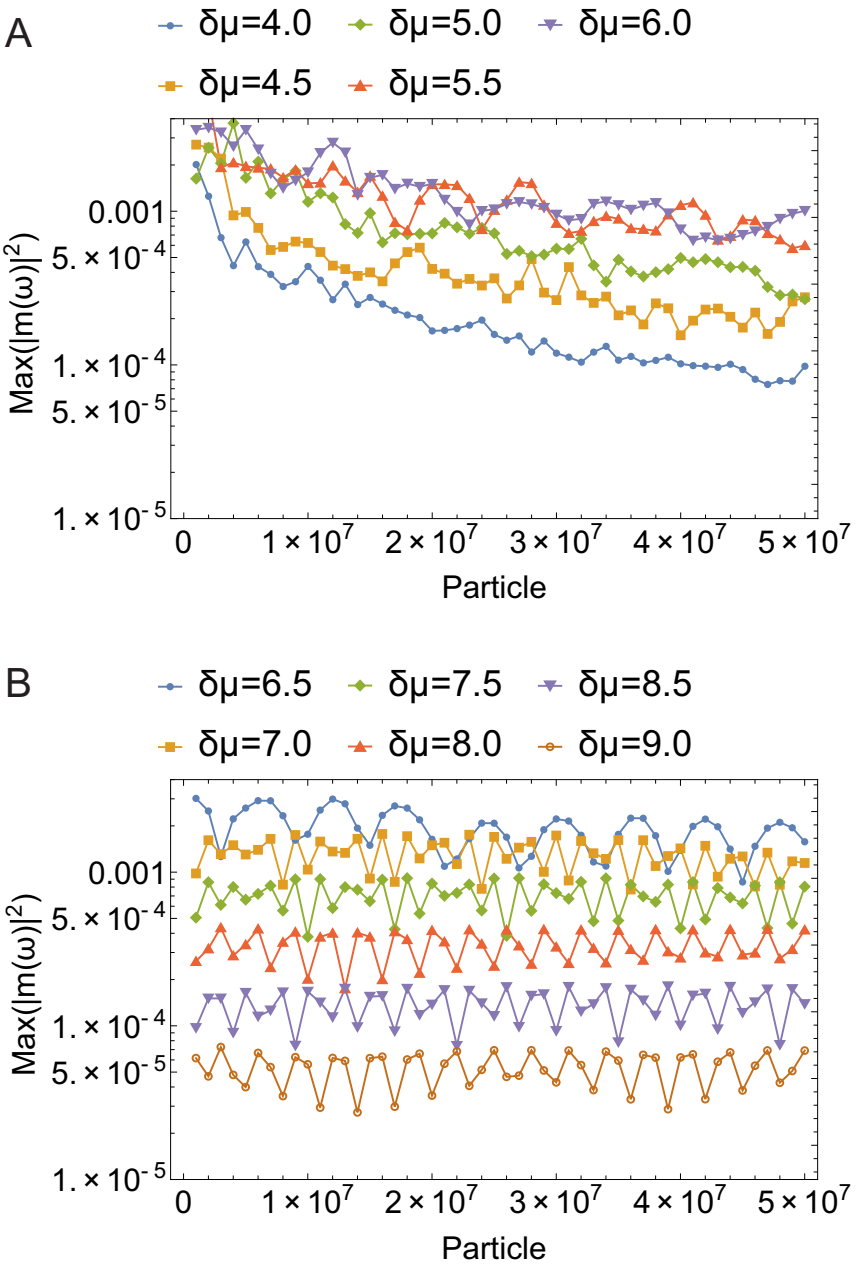

Figure 6.3: Peak of the Fourier Transform as a function of the number of particles in the assembly. Top: in this range, $\delta\mu = 4.0$ to 6.0 , the peak keeps decaying as the number of particles increases. Down: in this range, $\delta\mu = 6.5$ to 9.0, the peak stays constant with the number of particles.

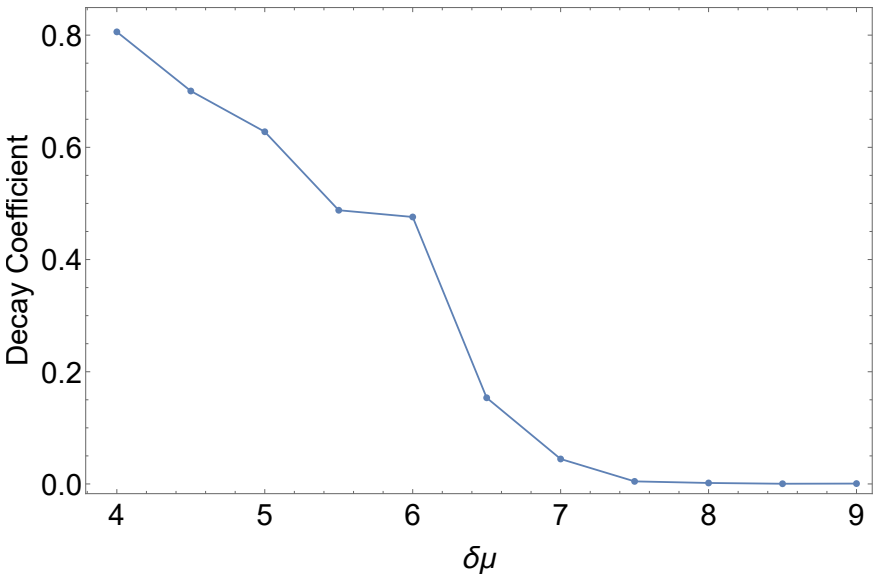

Figure 6.4: Decay coefficient as a function of $\delta\mu$. The decay coefficients, a, are extracted using $\ln \max(|m|^2) = a \ln N + b$.

the peak of the assembly first increases with increasing $\delta\mu$. It then caps out and decreases with increasing $\delta\mu$. Closer inspection reveals that the peaks in the profiles from $\delta\mu = 4$ to $\delta\mu = 6$ keep decaying with increasing particles while the profiles with higher $\delta\mu$ seem to stay constant. To quantify this, we fit the peak to the number of particles using the formula: $\ln \max(|m|^2) = a \ln N + b$. The parameter a is the decay coefficient of the assembly peak. Fig. 6.4 shows how this decay coefficient change with the $\delta\mu$. This suggests that to effectively drive a pattern from a varying field into the assembly, a minimum amount of driving force, $\delta\mu$, is required.

In addition to the assemblies' peaks obtained from Fourier Transform, the probability of obtaining a certain particle at a certain time can also be used to measure how the magnetic field drives its pattern into the assembly. This is done by recording the time in which a particle is added into the inner layer of the assembly. Fig 6.5A shows the probability profiles inside the assembly of some $\delta\mu s$. Similar to the peaks of the Fourier Transforms, the amplitude of the probability profiles also maximizes at certain $\delta\mu$ as shown in Fig 6.5B. However, the location of this peak is not the same as the one obtained from the Fourier

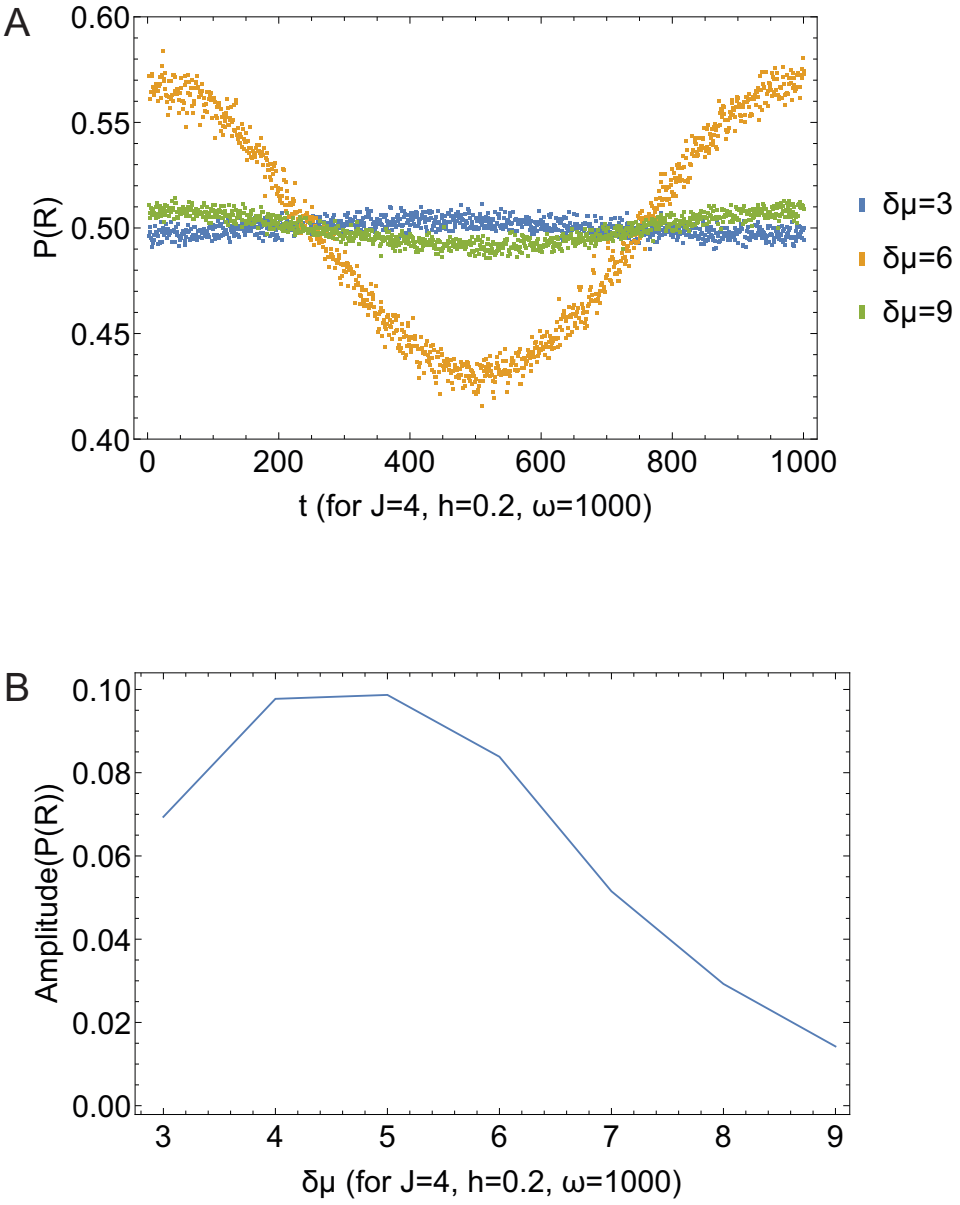

Figure 6.5: Up: Probability profiles of obtaining a red particle as a function of time. Down: Amplitudes of the probability profiles of obtaining a red particle.

Transform. From now on, we will use the probability profile as a metric to measure how well our approach model the simulations. We choose this mainly because the probability profile converges much faster in the simulation and can be readily obtained from the mean-field model.

6.3 Mean-Field Approach

Before developing a bi-partite Markov Network to describe our process fully, let's first try applying the mean-field approach developed for steady-state assembly. We consider the probability: $P^t(n_i, n_j)$ and master equations:

$$\begin{aligned}
\frac{dP^t(n_i,n_j)}{dt} = &-P^t(n_i,n_j)\Big[\sum_{n_k} P_{gen}(n_k|n_j)k_t^{add}(n_i,n_j \to n_j,n_k)+ \\
&\sum_{n_k} P_{sys}^t(n_k|n_i)k_t^{rem}(n_k,n_i \leftarrow n_i,n_j)\Big]+ \\
&\Big[P_{sys}^t(n_i|n_j)\sum_{n_k} P(n_j,n_k)k_t^{rem}(n_i,n_j \leftarrow n_j,n_k)\Big]+ \\
&\Big[P_{gen}(n_j|n_i)\sum_{n_k} P(n_k,n_i)k_t^{add}(n_k,n_i \to n_i,n_j)\Big]
\end{aligned} \tag{6.3}$$

The conditional probability $P_{sys}^t(n_i|n_j)$ can be expressed through the other probabilities:

$$P_{sys}^t(n_i|n_j) = \frac{P^t(n_i,n_j)}{\sum_{n_i} P^t(n_i,n_j)} \tag{6.4}$$

One approach in solving the above master equations assumes that the system is at a quasi-steady state. With this, we can set the left-hand side of Eq. 6.3 to 0 and solve the master equations consistently at every point in time. However, this naive approach only works in the limit where the oscillation is extremely slow (high ω). In general, we cannot assume the system is at a quasi-steady state, and the master equations have to be solved numerically. In Fig 6.6, we compare the probability profiles obtained from the FRM simulations (blue dots)

and those from solving the mean-field master equation, Eq. 6.3, numerically (red curve), which indicates that in the regime of high $\delta\mu$ and high ω, the mean-field master equations can be used to predict the structures inside a periodic assembly. This is because, in these regimes, the rates at which particles going into the assembly are relatively high compared to the rate that the field is changing. However, this does not mean the assembly is in a quasi-steady state. In Fig. 6.6B, we plot the probability profile by solving the master equations assuming steady-state (green dot) to contrast the one obtained from solving the time-dependent master equations numerically (red curve).

6.4 Bi-Partite Markov Network

When we develop our mean-field model, one assumption that we take is that the conditional probability operator is universal across the assembly. This, however, is no longer true when the different parts of the assembly experience different fields. To take in account this effect, we have to include a time-dependent term in our probabilities: $P^t(n_i t_x, n_j t_y)$. Here for the part $n_i t_x$, the t_x represents the time that the particle n_i is added into the assembly. In order words, a particle will remember the time it is deposited into the assembly. The t_y is on the interface particle and represents the current time of the system. With this setting, there will be two different kinds of transitions in this process. One is the additional and removal of particles. Another one is the moving of time at the tip of the particle. The possible transitions in addition and removal of particles are:

$$n_i t_y, n_j t_x \underset{k_{rem}}{\overset{k_{add}}{\rightleftarrows}} n_j t_x, n_k t_x \tag{6.5}$$

$$n_i t_y, n_j t_x \xleftarrow[k_{rem}]{} n_j t_z, n_k t_x \quad (\text{with} \quad t_z \neq t_x)$$

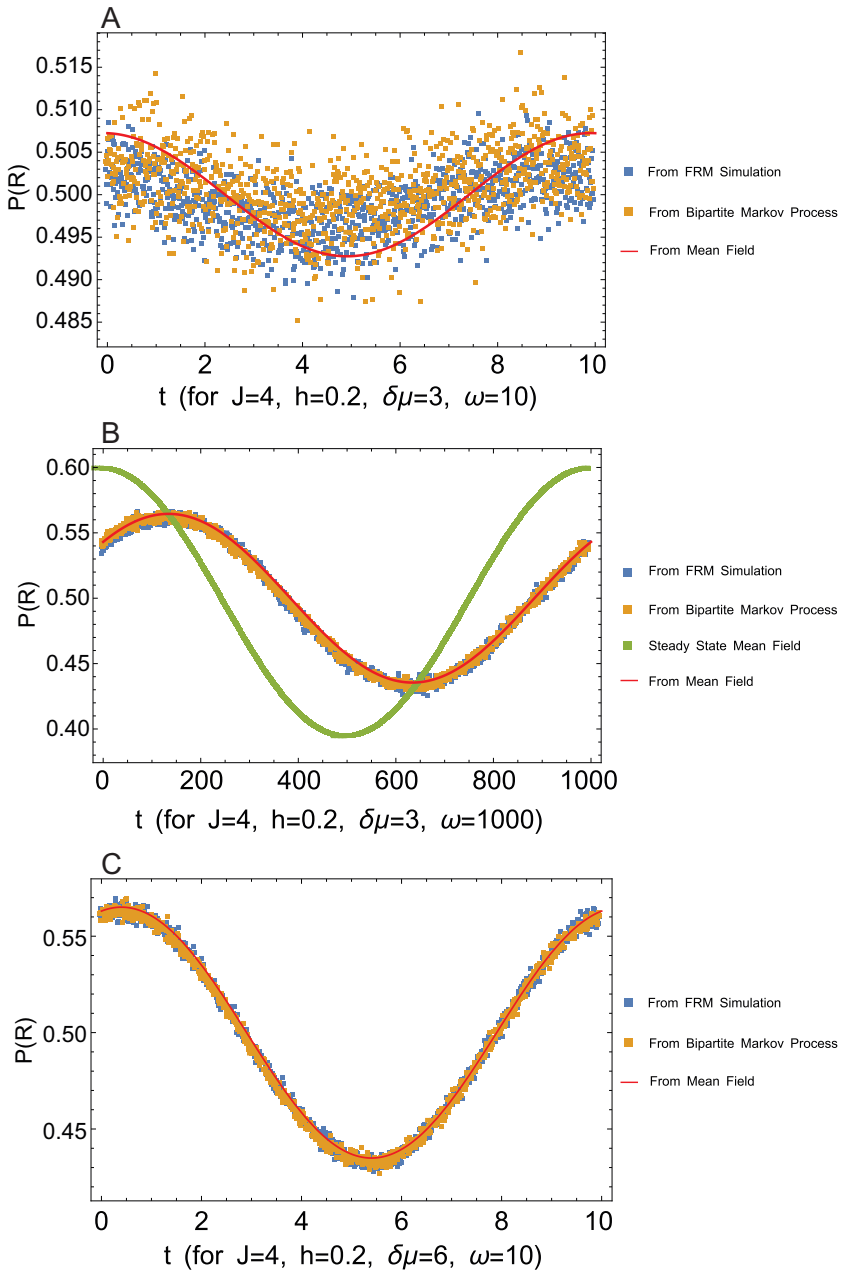

Figure 6.6: Probability profile for obtaining a red particle at a certain time in the assembly at A: This profile is at $\delta\mu = 3, J = 4, h = 0.2, \omega = 10$. B: This profile is at $\delta\mu = 3, J = 4, h = 0.2, \omega = 1000$. C: This profile is at $\delta\mu = 6, J = 4, h = 0.2, \omega = 10$. The blue dots are obtained from FRM simulations. The orange dots are obtained from simulations of the bi-partite Markov process with Eq. 6.9. The red curve is obtained by solving the mean-field master equations, Eq. 6.3, numerically with time-dependent rates. The green dots are obtained from solving the mean-field master equations, Eq. 6.3, by assuming the assembly is at quasi steady-state at every point in time.

The transition in time is simply: $n_i t_y, n_j t_x \xrightarrow{\lambda} n_i t_y, n_j t_{x+1}$ Here $\lambda = \frac{M}{\omega}$, M is the number of time states we have partitioned the field into.

With the above transitions, the master equations for this bi-partite Markov process are:

$$\begin{aligned}
&\frac{dP^t(n_i t_x, n_j t_x)}{dt} = -P^t(n_i t_x, n_j t_x)\Big[\sum_{n_k} P_{gen}(n_k t_x | n_j t_x) k_t^{add}(n_i t_x, n_j t_x \to n_j t_x, n_k t_x) \\
&+ \sum_{n_k, t_y} P^t_{sys}(n_k t_y | n_i t_x) k_t^{rem}(n_k t_y, n_i t_x \leftarrow n_i t_x, n_j t_x)\Big] \\
&+ \Big[\sum_{n_k, t_y} P^t_{sys}(n_i t_x | n_j t_y) P^t(n_j t_y, n_k t_x) k_t^{rem}(n_i t_x, n_j t_x \leftarrow n_j t_y, n_k t_x)\Big] \\
&+ \Big[\sum_{n_k, t_y} P_{gen}(n_j t_x | n_i t_x) P^t(n_k t_y, n_i t_x) k_t^{add}(n_k t_y, n_i t_x \to n_i t_x, n_j t_x))\Big] \\
&+ \lambda P^t(n_i t_x, n_j t_{x-1}) - \lambda P^t(n_i t_x, n_j t_x)
\end{aligned} \tag{6.6}$$

$$\begin{aligned}
&\frac{dP^t(n_i t_x, n_j t_z)}{dt} = -P^t(n_i t_x, n_j t_z)\Big[\sum_{n_k} P_{gen}(n_k t_z | n_j t_z) k_t^{add}(n_i t_x, n_j t_z \to n_j t_z, n_k t_z) + \\
&\sum_{n_k, t_y} P^t_{sys}(n_k t_y | n_i t_x) k_t^{rem}(n_k t_y, n_i t_z \leftarrow n_i t_x, n_j t_z)\Big] \\
&+ \Big[\sum_{n_k, t_y} P^t_{sys}(n_i t_x | n_j t_y) P^t(n_j t_y, n_k t_z) k_t^{rem}(n_i t_x, n_j t_z \leftarrow n_j t_y, n_k t_z)\Big] \\
&+ \lambda P^t(n_i t_x, n_j t_{z-1}) - \lambda P^t(n_i t_x, n_j t_z)
\end{aligned} \tag{6.7}$$

In the Eq. 6.7, $x \neq z$. With this setup, we can construct self-consistent formulas that connect

the probabilities at the interface and the probabilities inside the assembly like we did before:

$$P^t_{inside}(n_i t_x, n_j t_{\text{ave}}) \propto \sum_{n_k,t_y,t_z} \Big[P_{gen}(n_j t_x | n_i t_x) k^{add}_t(n_k t_y, n_i t_x \rightarrow n_i t_x, n_j t_x) P^t(n_k t_y, n_i t_x) \\ - P^t(n_i t_x, n_j t_z) P^t_{sys}(n_k t_y | n_i t_z) k^{rem}_t(n_k t_y, n_i t_z \leftarrow n_i t_x, n_j t_z) \Big] \tag{6.8}$$

Usually for the removal move, the term $k^{rem}_t(n_k t_y, n_i t_z \leftarrow n_i t_x, n_j t_z)$ doesn't depend on the inner configuration $n_k t_y$. This allows us to simplify the last term to:

$$P^t_{inside}(n_i t_x, n_j t_{\text{ave}}) \propto \sum_{n_k,t_y,t_z} \Big[P_{gen}(n_j t_x | n_i t_x) k^{add}_t(n_k t_y, n_i t_x \rightarrow n_i t_x, n_j t_x) P^t(n_k t_y, n_i t_x) \\ - P^t(n_i t_x, n_j t_z) k^{rem}_t(n_k t_y, n_i t_z \leftarrow n_i t_x, n_j t_z) \Big] \tag{6.9}$$

Figs. 6.6 show that the probability profiles obtained using Eq. 6.9 (orange dots) match very well with ones from FRM simulations (blue dots). We have also tested Eq. 6.9 using different kinetics and harmonics, Eq. 6.9 (orange dots) still captures the probability profiles very well when the mean field method (red curve) does not (Fig .6.7).

6.5 Entropy Production

Now we can proceed to calculate the entropy production for the system. Because of the system's setup, some of the transitions are unidirectional, so the normal definition of entropy production does not apply to them. The total entropy production, however, only depends

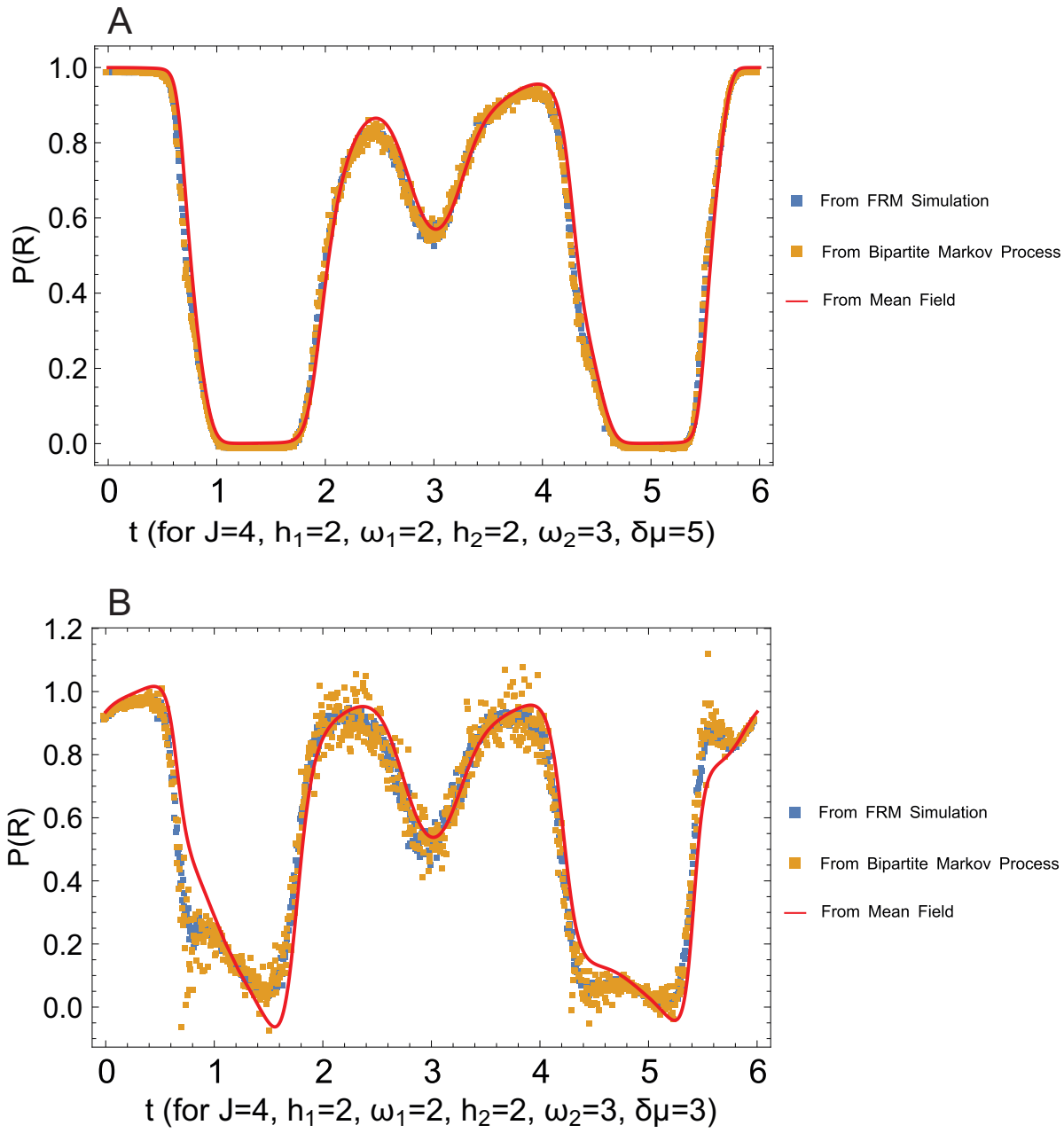

Figure 6.7: Probability profile for obtaining a red particle at a certain time in the assembly with two magnetic fields at different periods $\omega_1 = 2$ and $\omega_2 = 3$ with $J = 4, h = 2$. A: This profile is for $\delta\mu = 5$. B: This profile is for $\delta\mu = 3$. The results from bi-partite Markov processes agree very well with ones from FRM simulations. The mean-field method, however, only works well at high $\delta\mu$.

on the bidirectional transitions [112]. The total entropy production, thus, is:

$$\begin{aligned}\dot{S} = \sum_{t_x,t_y,n_k,n_i,n_j} \big[&P_{gen}(n_j t_x | n_i t_x) k^{add}(n_k t_y, n_i t_x \to n_i t_x, n_j t_x) P^t(n_k t_y, n_i t_x) \\ &- P^t_{sys}(n_k t_y | n_i t_x) k^{rem}(n_k t_y, n_i t_x \leftarrow n_i t_x, n_j t_x) P^t(n_i t_x, n_j t_x)\big] \\ &\ln \frac{P_{gen}(n_j t_x | n_i t_x) k^{add}(n_k t_y, n_i t_x \to n_i t_x, n_j t_x) P^t(n_k t_y, n_i t_x)}{P^t_{sys}(n_k t_y | n_i t_x) k^{rem}(n_k t_y, n_i t_x \leftarrow n_i t_x, n_j t_x) P^t(n_i t_x, n_j t_x)}\end{aligned} \tag{6.10}$$

However, this entropy production increases without limit with the number of time partitions in the bi-partite Markov Network. This is because we have artificially labeled timestamps into the particles, which cost information making the entropy production increase. We then have to look at a coarse grain probability to get an entropy production that converges with increasing time partition.

$$P^t(n_i t_{\text{ave}}, n_j t_y) = \sum_{t_x} P^t(n_i t_x, n_j t_y) \tag{6.11}$$

The master equation for this coarse grain probability is:

$$
\begin{aligned}
&\frac{dP^t(n_i t_{\text{ave}}, n_j t_y)}{dt} = \\
&- \sum_{t_x,,t_z,n_k} P^t(n_i t_x, n_j t_y)\Big[P_{gen}(n_k t_y|n_j t_y)k^{add}(n_i t_x, n_j t_y \to n_j t_y, n_k t_y)+ \\
&P^t_{sys}(n_k t_z|n_i t_x)k^{rem}(n_k t_z, n_i t_y \leftarrow n_i t_x, n_j t_y)\Big]+ \\
&\Big[\sum_{n_k,t_x,t_z} P^t_{sys}(n_i t_x|n_j t_z)P^t(n_j t_z, n_k t_y)k^{rem}(n_i t_x, n_j t_y \leftarrow n_j t_z, n_k t_y)\Big]+ \\
&\Big[\sum_{n_k,t_x} P_{gen}(n_j t_y|n_i t_y)P^t(n_k t_x, n_i t_y)k^{add}(n_k t_x, n_i t_y \to n_i t_y, n_j t_y))\Big] \\
&+ \lambda P^t(n_i t_{\text{ave}}, n_j t_{y-1}) - \lambda P^t(n_i t_{\text{ave}}, n_j t_y) \\
&= -P^t(n_i t_{\text{ave}}, n_j t_y)\Bigg(\sum_{t_x,,t_z,n_k} P^t_{sys}(t_x|n_i, n_j t_y) \\
&\Big[P_{gen}(n_k t_y|n_j t_y)k^{add}(n_i t_x, n_j t_y \to n_j t_y, n_k t_y)+ \\
&P^t_{sys}(n_k t_z|n_i t_x)k^{rem}(n_k t_z, n_i t_y \leftarrow n_i t_x, n_j t_y)\Big]\Bigg)+ \\
&\sum_{n_k}\Bigg(P^t(n_j t_{\text{ave}}, n_k t_y)\Big[\sum_{t_x,t_z} P^t_{sys}(n_i t_x|n_j t_z)P^t_{sys}(t_z|n_j, n_k t_y)k^{rem}(n_i t_x, n_j t_y \leftarrow n_j t_z, n_k t_y)\Big] \\
&+ P^t(n_k t_{\text{ave}}, n_i t_y)\Big[\sum_{t_x} P_{gen}(n_j t_y|n_i t_y)P^t_{sys}(t_x|n_k, n_i t_y)k^{add}(n_k t_x, n_i t_y \to n_i t_y, n_j t_y)\Big]\Bigg) \\
&+ \lambda P^t(n_i t_{\text{ave}}, n_j t_{y-1}) - \lambda P^t(n_i t_{\text{ave}}, n_j t_y)
\end{aligned}
\tag{6.12}
$$

Unlike the master equations for the full probabilities, the master equations for the coarse grain probabilities cannot be self-consistently solved at a steady state. So to get the coarse grain probabilities, we have to solve the master equations of the full probabilities first. However, in the limit of high $\delta\mu$, high ω, and for the case, the rates are independent of the inner block, Eq. 6.12 reduces to the mean-field master equations we have earlier. Fig. 6.8

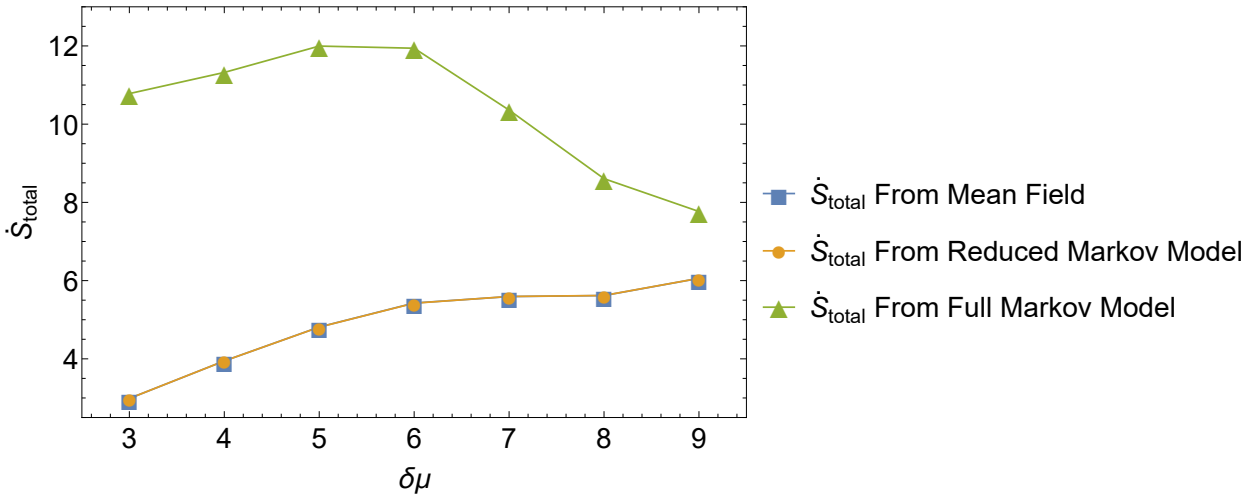

Figure 6.8: Entropy production of the one dimension growth assembly with rates affected by a time-varying magnetic field h(t) with $J = 4, h = 0.2, \omega = 1000$

shows that entropy production from the coarse grain master equation and one from the mean-field equation are indistinguishable from each other.

$$\dot{S}_{reduced} = \sum_{t_y, n_k, n_i, n_j}$$
$$\Big(P^t(n_k t_{\text{ave}}, n_i t_y) \big[\sum_{t_x} P_{gen}(n_j t_y | n_i t_y) P^t_{sys}(t_x | n_k, n_i t_y) k^{add}(n_k t_x, n_i t_y \to n_i t_y, n_j t_y) \big]$$
$$- P^t(n_i t_{\text{ave}}, n_j t_y) \big[\sum_{t_x, t_z} P^t_{sys}(n_k t_x | n_i t_z) P^t_{sys}(t_z | n_i, n_j t_y) k^{rem}(n_k t_x, n_i t_y \leftarrow n_i t_z, n_j t_y) \big] \Big)$$
$$\ln \frac{P^t(n_k t_{\text{ave}}, n_i t_y) \big[\sum_{t_x} P_{gen}(n_j t_y | n_i t_y) P^t_{sys}(t_x | n_k, n_i t_y) k^{add}(n_k t_x, n_i t_y \to n_i t_y, n_j t_y) \big]}{P^t(n_i t_{\text{ave}}, n_j t_y) \big[\sum_{t_x, t_z} P^t_{sys}(n_k t_x | n_i t_z) P^t_{sys}(t_z | n_i, n_j t_y) k^{rem}(n_k t_x, n_i t_y \leftarrow n_i t_z, n_j t_y) \big]} \tag{6.13}$$

As the system approaches the transition in which pattern is added into the assembly (around $\delta\mu \approx 7$), the entropy production of the coarse grain system approaches an inflection point. And the entropy production of the bi-partite Markov network model starts to decrease. These indicate that in the regime where patterns are deposited effectively into the assembly, there's little correlation in an assembly pattern deposited from one time to those at another

time. The results in Fig. 6.8 also suggest we can use the entropy production to predict the required $\delta\mu$ to deposit particles into the assembly effectively.

6.6 Conclusion

In this chapter, we have developed a framework to study the growing of an assembly under periodic drive. In the regime of high $\delta\mu$ and ω, the mean-field equations for steady-state can be used to predict the probability profile inside the assembly. A bi-partite Markov network has also been constructed that works in a wider regime than the mean-field equations. We demonstrate that a minimal driving force is required to grow an assembly under a certain pattern effectively. As the system goes through these two regimes, the entropy production also goes through an inflection point. We plan to test this observation with more complicated systems with thermal phase transition such as 2D-Ising in future studies.

CHAPTER 7

CONCLUSION AND OUTLOOK

7.1 Conclusions

In this dissertation, we have developed a general framework to study steady-state and periodic non-equilibrium self-assembly. Using ideas from stochastic thermodynamics, we have argued that the energy dissipation of a process can potentially be used to constrain self-assembly properties, correlations, material properties, and phase transition behavior in many non-equilibrium systems. Biology uses non-equilibrium activity to support a variety of novel functional states. We anticipate that the frameworks reviewed here can provide a starting point to address some of the unique phenomenology seen in biophysical systems and potentially replicate them in synthetic materials.

7.2 Outlooks

7.2.1 Hydrodynamic generalizations

Eq. 2.37 and its various proposed generalizations, we have assumed that the dominant non-equilibrium forces are tied to growth. Our approach does not consider other dissipative effects such as those due to hydrodynamic modes [113] and particle transport, which can be important factors. If the contributions from such considerations are to be considered, Eq. 2.37 needs to be generalized so that the entropy production rate includes these effects. Following the theoretical framework laid out above, the thermodynamic uncertainty relations can be potentially be used to obtain a set of inequalities constraining the fluctuations in various fluxes. Such sets of inequalities can be viewed as generalizations of the classical linear irreversible thermodynamics approach that is commonly used to obtain phenomenological equations of motion in near equilibrium settings [114, 115].

7.2.2 Modulating structure and phase transformation behavior of self-assembled colloidal crystals using non-equilibrium forcing

Building on the results in Ref [116, 117] we anticipate that this thermodynamic framework can be used to study the properties of colloidal or nanoscale crystals assembled under non-equilibrium growth conditions. Indeed, experiments and simulations have shown that non-equilibrium forcing can potentially modify crystal structures and phase behavior in such setups [118, 119, 120]. For example, Ref [120] used computer simulations to study the non-equilibrium phase diagram of a binary $A-B$ mixture. Their work showed that the location of the line separating the BCC and CP phases shifted if the crystals were grown out of equilibrium. The non-equilibrium theoretical framework in Eq. 2.37 can potentially reveal how energy landscapes are different from the equilibrium landscapes or, alternately, how crystals characteristic of interaction energies other than the ones encoded physically can be generated by non-equilibrium forcing (for example, using $\delta\mu$). Such studies can clarify how the equilibrium phase diagram and boundaries can be modified by non-equilibrium forcing [120].

Adapting Eq. 2.37 so that it applies to finite time processes, for example by using generalizations of the thermodynamic uncertainty relations to finite time processes [22, 23], it might be possible to develop predictive thermodynamic frameworks that explain the self-assembly of large complex *terminal* structures (i.e. finite structures as opposed to the non-terminal assemblies considered above) [121] from patchy nanoparticles [122, 123] and DNA mediated interactions [37].

7.2.3 Thermodynamic bounds on membrane morphologies due to non-equilibrium activity.

Building on the above-described applications of Eq. 2.37 to understand non-equilibrium morphologies of model membranes (embedded in two dimensions), future work should explore whether similar relations can be written down for more realistic membrane models that are embedded in three dimensions (Fig. 4.13) and to include cases where detailed balance is broken due to other membrane remodeling events. One important example of this is binding and unbinding of curvature-preferring proteins, which are often involved in active membrane remodeling processes such as endocytosis and cell fission [58, 124]. Non-equilibrium thermodynamic bounds, if derivable in a manner that accounts for the various hydrodynamic flows, can provide intuition for the microscopic energy requirements to drive such an organization. It can provide a general far from equilibrium framework for controlling membrane material properties, such as the local surface tension, at the cost of energy consumption.

7.2.4 Biological polymerization reactions

Proofreading mechanisms used during various DNA replication processes provide a very illustrative example of the tradeoffs between dissipation, speed, and error or functionality in biology. We anticipate that connections like those in Eq. 2.37 will further elucidate these tradeoffs. Indeed, expressions for entropy production for various model replication processes have already been obtained. Such expressions can be used to extend Eq. 2.37 to study the energy-speed-accuracy tradeoffs in replication and translation processes in biology [125, 39, 17]

REFERENCES

[1] S. Whitelam and R. L. Jack, Annual review of physical chemistry (2014), 10.1146/annurev-physchem-040214-121215.

[2] J. Winkelman, C. Suarez, G. Hocky, A. Harker, A. Morganthaler, J. Christensen, G. Voth, J. Bartles, and D. Kovar, Curr. Biol **26**, 2697 (2016).

[3] W. R. Inc., "Mathematica, Version 12.2," (2020), champaign, IL, 2020.

[4] Y. Ke, L. L. Ong, W. M. Shih, and P. Yin, Science (New York, N.Y.) **338**, 1177 (2012).

[5] M. R. Jones, N. C. Seeman, and C. A. Mirkin, Science **347**, 1260901 (2015).

[6] A. Reinhardt and D. Frenkel, Physical Review Letters **112**, 238103 (2014).

[7] L. O. Hedges, R. V. Mannige, and S. Whitelam, Soft matter **10**, 6404 (2014).

[8] S. Hormoz and M. P. Brenner, Proceedings of the National Academy of Sciences of the United States of America **108**, 5193 (2011).

[9] S. C. Weber and C. P. Brangwynne, Cell **149**, 1188 (2012).

[10] S. Mann, Nature materials **8**, 781 (2009).

[11] E. Sanz, C. Valeriani, D. Frenkel, and M. Dijkstra, Phys. Rev. Lett. **99**, 055501 (2007).

[12] E. Rabani, D. R. Reichman, P. L. Geissler, and L. E. Brus, Nature **426**, 271 (2003).

[13] T. S. Ursell, J. Nguyen, R. D. Monds, A. Colavin, G. Billings, N. Ouzounov, Z. Gitai, J. W. Shaevitz, and K. C. Huang, Proceedings of the National Academy of Sciences **111**, E1025 (2014).

[14] A. Levandovsky and R. Zandi, Phys. Rev. Lett. **102**, 198102 (2009).

[15] M. F. Hagan and D. Chandler, Biophysical journal **91**, 42 (2006).

[16] H. Jiang, F. Si, W. Margolin, and S. X. Sun, Biophysical journal **101**, 327 (2011).

[17] D. Andrieux and P. Gaspard, Proceedings of the National Academy of Sciences of the United States of America **105**, 9516 (2008).

[18] A. J. Kim, R. Scarlett, P. L. Biancaniello, T. Sinno, and J. C. Crocker, Nature materials **8**, 52 (2009).

[19] S. Auer and D. Frenkel, Nature **413**, 711 (2001).

[20] A. C. Barato and U. Seifert, Phys. Rev. Lett. **114**, 158101 (2015).

[21] T. R. Gingrich, J. M. Horowitz, N. Perunov, and J. L. England, Physical Review Letters **116**, 120601 (2016).

[22] P. Pietzonka, F. Ritort, and U. Seifert, Phys. Rev. E **96**, 012101 (2017).

[23] J. M. Horowitz and T. R. Gingrich, Physical Review E **96**, 020103 (2017).

[24] T. Koyuk and U. Seifert, Phys. Rev. Lett. **122**, 230601 (2019).

[25] A. C. Barato, R. Chetrite, A. Faggionato, and D. Gabrielli, New Journal of Physics **20**, 103023 (2018).

[26] T. R. Gingrich and J. M. Horowitz, Phys. Rev. Lett. **119**, 170601 (2017).

[27] S. L. Freedman, C. Suarez, J. D. Winkelman, D. R. Kovar, G. A. Voth, A. R. Dinner, and G. M. Hocky, Proceedings of the National Academy of Sciences **116**, 16192 (2019).

[28] P. Gaspard and D. Andrieux, The Journal of chemical physics **141**, 044908 (2014).

[29] D. Andrieux and P. Gaspard, Journal of Statistical Physics **127**, 107 (2007).

[30] U. Seifert, Reports on Progress in Physics **75**, 126001 (2012).

[31] A. Pal, S. Reuveni, and S. Rahav, Phys. Rev. Research **3**, 013273 (2021).

[32] S. Whitelam, R. Schulman, and L. Hedges, Physical Review Letters **109**, 265506 (2012).

[33] S. Whitelam, L. O. Hedges, and J. D. Schmit, Phys. Rev. Lett. **112**, 155504 (2014).

[34] J. L. England, Nature Nanotechnology **10**, 919 (2015).

[35] A. C.-H. Sue, R. V. Mannige, H. Deng, D. Cao, C. Wang, F. Gándara, J. F. Stoddart, S. Whitelam, and O. M. Yaghi, Proceedings of the National Academy of Sciences **112**, 5591 (2015).

[36] A. Murugan, Z. Zeravcic, M. P. Brenner, and S. Leibler, Proc. Natl. Acad. Sci. USA **112**, 54 (2015).

[37] W. M. Jacobs, A. Reinhardt, and D. Frenkel, Proceedings of the National Academy of Sciences of the United States of America **112**, 6313 (2015).

[38] A. Murugan, Z. Zeravcic, M. P. Brenner, and S. Leibler, Proceedings of the National Academy of Sciences **112**, 54 (2015).

[39] P. Sartori and S. Pigolotti, Phys. Rev. X **5**, 041039 (2015).

[40] C. Battle, C. P. Broedersz, N. Fakhri, V. F. Geyer, J. Howard, C. F. Schmidt, and F. C. MacKintosh, Science **352**, 604 (2016).

[41] G. Lan, P. Sartori, S. Neumann, V. Sourjik, and Y. Tu, Nature physics **8**, 422 (2012).

[42] P. Mehta and D. J. Schwab, Proceedings of the National Academy of Sciences of the United States of America **109**, 17978 (2012).

[43] J. J. Hopfield, Proceedings of the National Academy of Sciences **71**, 4135 (1974).

[44] A. Murugan, D. A. Huse, and S. Leibler, Proceedings of the National Academy of Sciences **109**, 12034 (2012).

[45] A. Murugan and S. Vaikuntanathan, Journal of Statistical Physics **162**, 1183 (2016).

[46] A. Murugan and S. Vaikuntanathan, Nature Communications **8**, 13881 (2017).

[47] A. C. Barato and U. Seifert, Physical Review E **95**, 062409 (2017).

[48] H. T. McMahon and J. L. Gallop, Nature **438**, 590 (2005).

[49] H. Turlier, D. A. Fedosov, B. Audoly, T. Auth, N. S. Gov, C. Sykes, J. F. Joanny, G. Gompper, and T. Betz, Nature Physics **12**, 513 (2016).

[50] J. C. Stachowiak, E. M. Schmid, C. J. Ryan, H. S. Ann, D. Y. Sasaki, M. B. Sherman, P. L. Geissler, D. A. Fletcher, and C. C. Hayden, Nature Cell Biology **14**, 944 (2012).

[51] Z. Chen, E. Atefi, and T. Baumgart, Biophysical Journal **111**, 1823 (2016).

[52] P. Rangamani, K. K. Mandadap, and G. Oster, Biophysical journal **107**, 751 (2014).

[53] S. Leibler, Journal de Physique **47**, 507 (1986).

[54] K. Gowrishankar, S. Ghosh, S. Saha, C. Rumamol, S. Mayor, and M. Rao, Cell **149**, 1353 (2012).

[55] J. Weichsel and P. L. Geissler, PLoS computational biology **12**, e1004982 (2016).

[56] D. Drasdo, Physical Review Letters **84**, 4244 (2000).

[57] S. Ramaswamy, J. Toner, and J. Prost, Physical Review Letters **84**, 3494 (2000).

[58] M. Rao and R. C. Sarasij, Physical Review Letters **87**, 128101 (2001).

[59] J. Solon, J. Pécréaux, P. Girard, M. C. Fauré, J. Prost, and P. Bassereau, Physical Review Letters **97**, 3 (2006).

[60] E. Hannezo, J. Prost, and J. F. Joanny, Physical Review Letters **107**, 1 (2011).

[61] S. Leibler, R. R. P. Singh, and M. E. Fisher, Physical Review Letter **59**, 1989 (1987).

[62] M. E. Fisher, Physica D: Nonlinear Phenomena **38**, 112 (1989).

[63] J. Rudnick and G. Gaspari, Science **252**, 422 (1991).

[64] M. K. Mitra, G. I. Menon, and R. Rajesh, Physical Review E **77**, 041802 (2008).

[65] E. Katifori, S. Alben, and D. R. Nelson, Physical Review E **79**, 056604 (2009).

[66] T. Ruiz-Herrero, T. G. Fai, and L. Mahadevan, Physical Review Letter **123**, 038102 (2019).

[67] Y. Li and P. R. ten Wolde, Physical Review Letter **123**, 148003 (2019).

[68] W. Helfrich, Zeitschrift fur Naturforschung Teil C Biochemie Biophysik Biologie Virologie **28**, 693 (1973).

[69] B. Loubet, U. Seifert, and M. A. Lomholt, Physical Review E - Statistical, Nonlinear, and Soft Matter Physics **85**, 1 (2012).

[70] J. Paulose, G. A. Vliegenthart, G. Gompper, and D. R. Nelson, Proceedings of the National Academy of Sciences **109**, 19551 (2012).

[71] S. T. Milner and S. A. Safran, Phys. Rev. A **36**, 4371 (1987).

[72] A. Mogilner and G. Oster, Biophys. J **71**, 3030 (1996).

[73] R. B. Dickinson, Journal Math. Biol. **58**, 81 (2009).

[74] A. Jégou and G. Romet-Lemonne, Curr. Opin. Cell Biol. **68**, 72 (2020).

[75] M. Murrell, P. W. Oakes, M. Lenz, and M. L. Gardel, Nature reviews Molecular cell biology **16**, 486 (2015).

[76] M. L. Gardel, I. C. Schneider, Y. Aratyn-Schaus, and C. M. Waterman, Annu. Rev. Cell Dev. Bio. **26**, 315 (2010).

[77] S. Watanabe, Y. Ando, S. Yasuda, H. Hosoya, N. Watanabe, T. Ishizaki, and S. Narumiya, Mol. Biol. Cell. **19**, 2328 (2008).

[78] R. S. Kadzik, K. E. Homa, and D. R. Kovar, Annu. Rev. Cell. Dev. Biol. **36**, 35 (2020).

[79] D. Vavylonis, J.-Q. Wu, S. Hao, B. O'Shaughnessy, and T. D. Pollard, Science **319**, 97 (2008).

[80] D. Zimmermann, K. E. Homa, G. M. Hocky, L. W. Pollard, M. Enrique, G. A. Voth, K. M. Trybus, and D. R. Kovar, Nature Comm. **8**, 1 (2017).

[81] Y. Tu, Proceedings of the National Academy of Sciences of the United States of America **105**, 11737 (2008).

[82] L. Tociu, E. Fodor, T. Nemoto, and S. Vaikuntanathan, Phys. Rev. X **9**, 041026 (2019).

[83] A. Murugan, D. A. Huse, and S. Leibler, Proc. Natl. Acad. Sci. **109**, 12034 (2012).

[84] A. C. Barato and U. Seifert, Phys. Rev. Lett. **114**, 158101 (2015).

[85] J. Yan, arXiv:1905.00929 (2019).

[86] A. Dechant, J. Phys. A Math. **52**, 035001 (2018).

[87] R. S. Ellis, *Entropy, large deviations, and statistical mechanics* (Springer-Verlag, 1985).

[88] J. M. Horowitz and T. R. Gingrich, Nature Physics **16**, 15 (2020).

[89] J. Liman, C. Bueno, Y. Eliaz, N. P. Schafer, M. N. Waxham, P. G. Wolynes, H. Levine, and M. S. Cheung, Proc. Natl. Acad. Sci. **117**, 10825 (2020).

[90] P. Bieling, J. Weichsel, R. McGorty, P. Jreij, B. Huang, D. A. Fletcher, R. D. Mullins, *et al.*, Cell **164**, 115 (2016).

[91] J. Weichsel and U. S. Schwarz, Proc. Natl. Acad. Sci. **107**, 6304 (2010).

[92] Y. Bashirzadeh, S. A. Redford, C. Lorpaiboon, A. Groaz, T. Litschel, P. Schwille, G. M. Hocky, A. R. Dinner, and A. P. Liu, bioRxiv:2020.10.03.322354 (2020).

[93] S. O. Lumsdon, E. W. Kaler, and O. D. Velev, Langmuir **20**, 2108 (2004).

[94] J. P. Singh, P. P. Lele, F. Nettesheim, N. J. Wagner, and E. M. Furst, Physical Review E **79**, 050401 (2009).

[95] M. Tagliazucchi, E. A. Weiss, and I. Szleifer, Proceedings of the National Academy of Sciences **111**, 9751 (2014).

[96] L. Corté, P. M. Chaikin, J. P. Gollub, and D. J. Pine, Nature Physics **4**, 420 (2008).

[97] D. Helbing, I. J. Farkas, and T. Vicsek, Physical Review Letters **84**, 1240 (2000).

[98] H. E. Stanley, Nature **404**, 718 (2000).

[99] F. Evers, R. D. L. Hanes, C. Zunke, R. F. Capellmann, J. Bewerunge, C. Dalle-Ferrier, M. C. Jenkins, I. Ladadwa, A. Heuer, R. Castañeda-Priego, and S. U. Egelhaaf, The European Physical Journal Special Topics **222**, 2995 (2013).

[100] A. S. Nunes, N. A. M. Araújo, and M. M. Telo da Gama, The Journal of Chemical Physics **144**, 034902 (2016).

[101] R. Klajn, M. A. Olson, P. J. Wesson, L. Fang, A. Coskun, A. Trabolsi, S. Soh, J. F. Stoddart, and B. A. Grzybowski, Nature Chemistry **1**, 733 (2009).

[102] G. Cheng and J. Perez-Mercader, Chem **6**, 1160 (2020).

[103] Y. Zheng and F. L. H. Brown, The Journal of Chemical Physics **139**, 164120 (2013).

[104] A. C. Barato, D. Hartich, and U. Seifert, Phys. Rev. E **87**, 042104 (2013).

[105] A. C. Barato, D. Hartich, and U. Seifert, Journal of Statistical Physics **153**, 460 (2013).

[106] G. Verley, C. V. den Broeck, and M. Esposito, New Journal of Physics **16**, 095001 (2014).

[107] D. Hartich, A. C. Barato, and U. Seifert, Journal of Statistical Mechanics: Theory and Experiment **2014**, P02016 (2014).

[108] J. M. Horowitz, Journal of Statistical Mechanics: Theory and Experiment **2015**, P03006 (2015).

[109] A. C. Barato and U. Seifert, Phys. Rev. X **6**, 041053 (2016).

[110] J. M. Horowitz and M. Esposito, Phys. Rev. X **4**, 031015 (2014).

[111] A. Jansen, Computer Physics Communications **86**, 1 (1995).

[112] D. M. Busiello, D. Gupta, and A. Maritan, Phys. Rev. Research **2**, 023011 (2020).

[113] M. Driscoll, B. Delmotte, M. Youssef, S. Sacanna, A. Donev, and P. Chaikin, Nature Physics **13**, 375 (2017).

[114] M. Doi, Journal of Physics: Condensed Matter **23**, 284118 (2011).

[115] S. R. d. S. R. Groot and P. P. Mazur, *Non-equilibrium thermodynamics* (Dover Publications, 1984) p. 510.

[116] M. Nguyen and S. Vaikuntanathan, Proceedings of the National Academy of Sciences **113**, 14231 (2016).

[117] M. Nguyen and S. Vaikuntanathan, arXiv preprint arXiv:1803.04368 (2018).

[118] W. B. Rogers, W. M. Shih, and V. N. Manoharan, Nature Reviews Materials **1**, 16008 (2016).

[119] Z. Zeravcic, V. N. Manoharan, and M. P. Brenner, Reviews of Modern Physics **89**, 031001 (2017).

[120] R. T. Scarlett, M. T. Ung, J. C. Crocker, and T. Sinno, Soft Matter **7**, 1912 (2011).

[121] A. V. Tkachenko, Physical Review Letters **106**, 255501 (2011).

[122] Z. Zhang and S. C. Glotzer, Nano Letters **4**, 1407 (2004).

[123] S. C. Glotzer and M. J. Solomon, Nature Materials **6**, 557 (2007).

[124] N. Ramakrishnan, J. H. Ipsen, M. Rao, and P. B. S. Kumar, Soft Matter **11**, 2387 (2015).

[125] J. M. Poulton, P. R. ten Wolde, and T. E. Ouldridge, Proceedings of the National Academy of Sciences **116**, 1946 (2019).